SYNTHETIC GAUGE FIELDS IN DEGENERATE QUANTUM GASES

A Dissertation

Presented to the Faculty of the Graduate School

of Cornell University

in Partial Fulfillment of the Requirements for the Degree of

Doctor of Philosophy

by

Ran Wei

August 2016

SYNTHETIC GAUGE FIELDS IN DEGENERATE QUANTUM GASES

Ran Wei, Ph.D.

Cornell University 2016

Cold atom experimentalists have developed “synthetic gauge fields”, which interact with neutral atoms in the same way that electromagnetic fields interact with electrons. These developments open up new classes of experiments in which one hopes to observe analogs of phenomena from solid state physics.

Here I present several theoretical studies on this fast growing area, which I divide into three parts: superfluid phases from synthetic magnetic fields, Majorana fermions from synthetic spin-orbit coupling, and adiabatic charge pumping in periodic potentials. In the first part, I study superfluid ground states and vortex structures for both Bose and Fermi gases in elongated geometries, including anisotropic harmonic traps and anisotropic optical lattices. In the second part, I study Majorana fermions in one dimensional trapped Fermi gases in the presence of superconducting pairing and spin-orbit coupling. In a related work, I study magnetic field dependence of Raman coupling for different alkali atoms. In the third part, I study a one dimensional topological quantum pump in a superlattice.

BIOGRAPHICAL SKETCH

Ran Wei was born on December 23, 1985, in Chengdu, P. R. China. He is the only child of his father Xingyuan Wei and his mother Xin Zhou. He grew up with a curious mind, being fascinated with how things work in nature. After graduating from Chengdu No.12 High School in 2004, he decided to pursue a physics career in the University of Science and Technology of China (USTC), where he earned his B.S. in 2008. He continued to study physics in USTC for three years, where he worked on quantum optics and quantum information. In the summer of 2010, he met Prof. Erich J. Mueller in an international workshop in Beijing, which later becomes his life's turning point. With the support of Prof. Mueller, he got a fellowship to study at Cornell University from 2011-2013, where he spent two truly enjoyable years doing research in cold atoms. He enrolled in the physics Ph.D program at Cornell in 2013, and continued to do research under the guidance of Prof. Mueller. He obtained his M.Sc. in January 2015 and will complete his Ph.D in August 2016.

To my Mom and Dad

To Erich J. Mueller

ACKNOWLEDGEMENTS

I owe a great debt of gratitude to my parents, for their enormous devotion, and for their immense love.

I am greatly indebted to Erich J. Mueller, my mentor, who offers tremendous helps in my career. I was blessed to meet him in Beijing in the summer of 2010, when my first journey to Cornell came true. I am extremely grateful for his continued supports in making me a Cornell Ph.D. Erich is certainly the most important person in my career.

I've learned a great deal of physics from Erich, whose desire and ability to translate intricate physics into simple terms has been very inspiring. My meetings with him have always been encouraging. He has infinite patience and is extremely generous – often, much of the work was done while he was "just" introducing problems. These meetings have been keeping me in good shape, for which I am very grateful.

I also like to thank other faculty members in physics department at Cornell. I thank Paul McEuen and James Sethna for giving me interesting A-exam questions, and for their encouragements on my career. I thank Jeevak Parpia and Lawrence Gibbons for helping me overcome big hurdles when I was transferred to Cornell. I thank Tomas Arias for useful discussions on computing the localized Wannier states. I thank Katja Nowack, Ryd Anders, Paul Ginsparg and Carl Frank for asking interesting questions in my physics lunch talk. I thank Sol Gruner and Katherine Selby for being my wonderful TA instructors.

Beyond Cornell, there are many other physicists I would like to thank. I thank Randall Hulet and Levent Subasi for writing me recommendation letters, Hui Zhai and Han Pu for their encouragements on my career, Deborah Jin and Ian Spielman for delightful discussions at Princeton, and Xiaopeng Li for being

a good friend in every cold atom conference I attended.

I like to thank my wonderful colleagues in Mueller's group, Stefan Baur, Elliot Kapit, Stefan Natu, Yariv Yanay, Bhuvanesh Sundar, Matthew Reichl, Sayan Choudhury, Shovan Dutta, Levent Subasi, Junjun Xu, Mehmet Oktel, and Nur Unal, for many enlightening discussions on physics problems. I also like to thank Bhuvanesh for teaching me climbing, Matt for telling me U.S. politics, Shovan for being a nice person who always smile, and Sayan for being a laid back physicist.

I would like to thank Kyuming Lee for many inspiring conversations on physics, as well as many other physics friends in the department, Yi-ting Hsu, Jian-huang She, Abolhassan Vaezi, Weehao Ng, Zhen Wah Tan, Gabriel Bonilla, Jihoon Kim, William Lou, Yi Xue Chong, Ryan Tapping, Huiyao Chen, Amir Hossein Tajdini, Salvator Lombardo, Yudai Tsai, Zheng-cheng Tao, Junhao Li, Margaret Zientek, Airlia Shaffer, Lauren Aycock, Srivatsan Chakram and Yogesh Patil, Deniz Gunceler, Jiang Yi, Daniel Citron, Xin Huang, Lijie Tu, Jason Stevens, Rahul Sharma, William Bergan, Gowri Kurup, Phil Burnham, Hao Shi, Merlin Enault-Dautheribes, Haofei Wei, Jordan Venderley, Katherine Quinn, Eddie Lee, Nathan Sitaraman, Eamonn O' Shea, Dan Gonnella, Christine Umbright, Kayla Jade Crosbie, Jocienne Nelson, Andre Sterenberg Frankenthal, Laurent Boulet, Ajay Bhat, Brian Schaefer, Ben Nicholson, Michael Reynolds, Kyle Dorsey Xiaopeng Li, Lin Frank Dong, Min-feng Tu, Biao Huang, Xiongjun Liu, Catherine Wang, and Andrea Lo.

I also like to acknowledge my funding agencies during my work at Cornell. From 2011 to 2013, I was supported by the China Scholarship Council (CSC), the National Science Foundation under Grant No. PHY-1068165, and a grant from the Army Research Office with funds from the DARPA optical lattice emulator

program. From 2013 to 2016, I was funded by the National Science Foundation Grant no. PHY-1068165, and a grant from ARO-MURI Nonequilibrium Many-body Dynamics (W911NF-14-1-0003).

I am grateful to my cousin in the school of Civil and Environmental Engineering at Cornell, for taking care of me for the past five years. I am very indebted to my uncle in Houston for having visited me three times at Cornell, and for always having strong beliefs in me.

Finally, I thank my girlfriend Yinghan Pan, who showed up three years ago and left me with many enjoyable memories.

TABLE OF CONTENTS

LIST OF TABLES

LIST OF FIGURES

CHAPTER 1

INTRODUCTION

Condensed matter, such as solid and liquid, exhibits rich and complicated phenomena. Physicists create simple theoretical models to understand them, and test their models with well-designed experiments. Ultracold atoms provide an excellent playground – they are particularly simple, clean and controllable, and that quantitative comparisons between theory and experiment are especially informative.

In the past decade, there has been tremendous success in engineering "simple" theoretical models in ultracold atom experiments, most of which aim to understand the many-body phenomena in condensed matter. One of the most exciting areas is the light-induced synthetic gauge fields, where artificial fields couple to neutral atoms the same way real fields couple to charge particles and spins. In this thesis, I will present several theoretical studies on this fast growing area.

Chapter 2 introduces the basic theory of light-induced gauge fields in ultracold atoms. I will be focusing on Abelian gauge fields with U(1) gauge symmetry. I will introduce the Raman process, and from that derive synthetic spin-orbit coupling, synthetic magnetic fields, and synthetic magnetic fluxes.

Chapter 3 includes a brief introduction on the basic mean-field theories in degenerate quantum gases under the framework of Gross - Pitaevski and Bogoliubov - de Gennes. I will be focusing on the variational wavefunction methods for bosons and Bogoliubov-de Gennes equations for fermions. These are the tools I use for my studies in **chapters 5 – 8**.

Chapter 4 introduces the theory of topology on energy bands. I will give mathematical descriptions on the topological invariant in periodic potentials. This includes the Zak's phase in one dimension and the Chern number in two dimensions. I will give two simple examples to shed light on the Zak's phase. I further study an anisotropic Harper model to elucidate relation between the Chern number and the edges states. Applications on these invariants on other models are included in **chapter 8** and **chapter 10**.

Chapter 5 and **Chapter 6** study applications of synthetic magnetic fields on interacting Bose and Fermi gases trapped in elongated geometries, where ground states display various phases and superfluid order parameters exhibit rich vortex structures. These two chapters were adapted from:

"Vortex structures of a two-component Bose-Einstein condensate for large anisotropies" by Ran Wei and Erich J. Mueller, published in Physical Review A 84, 063611 (2011);

"Pair density waves and vortices in an elongated spin-1/2 Fermi gas" by Ran Wei and Erich J. Mueller, published in Physical Review Letter 108, 245301 (2012).

Chapter 7 studies Bose gases trapped on a two-leg ladder in large magnetic fields, where a new phase was predicted. This chapter was adapted from:

"Theory of bosons in two-leg ladders with large magnetic fields" by Ran Wei and Erich J. Mueller, published in Physical Review A 89, 063617 (2014).

Chapter 8 studies application of synthetic spin-orbit coupling on one dimensional trapped Fermi gases with superconducting pairing. These gases are topological, which can lead to Majorana fermions. This chapter was adapted from:

"Majorana fermions in one dimensional spin-orbit-coupled Fermi gases" by Ran

Wei and Erich J. Mueller, published in Physical Review A 86, 063604 (2012).

Chapter 9 studies the Raman processes in the presence of real magnetic Zeeman fields. These Zeeman fields are crucial for generating superconducting pairing in ultracold Fermi gases, which are the key experimental considerations for producing Majorana fermions based on the proposal in **chapter 8**. This chapter was adapted from:

"Magnetic-field dependence of Raman coupling in alkali-metal atoms" by Ran Wei and Erich J. Mueller, published in Physical Review A 87, 042514 (2013).

Chapter 10 studies adiabatic charge pumping on a one dimensional superlattice, where the integrated adiabatic current is an unbounded Chern number. This model is also related to the anisotropic Harper model introduced in **chapter 4**, where the Chern number is the transverse Hall conductance. This chapter was adapted from:

"Anomalous charge pumping in a one dimensional optical superlattice" by Ran Wei and Erich J. Mueller, published in Physical Review A 92, 013609 (2015).

1.1 Chronological publication list

1. "Light pulse in Λ-type cold atomic gases" by **Ran Wei**, Bo Zhao, Youjin Deng, Shuai Chen, Zeng-Bing Chen, and Jian-Wei Pan, published in ***Physical Review A 81,043403 (2010)***.

2. “Deterministic spin-wave interferometer based on Rydberg blockade” by **Ran Wei**, Bo Zhao, Youjin Deng, Yu-Ao Chen, and Jian-Wei Pan, published in ***Physical Review A 83, 063623 (2011)***.

3. “Vortex structures of a two-component Bose-Einstein condensate for large anisotropies” by **Ran Wei** and Erich J. Mueller, published in ***Physical Review A 84, 063611 (2011)***.

4. “Pair density waves and vortices in an elongated spin-1/2 Fermi gas” by **Ran Wei** and Erich J. Mueller, published in ***Physical Review Letter 108, 245301 (2012)***.

5. “Majorana fermions in one dimensional spin-orbit-coupled Fermi gases” by **Ran Wei** and Erich J. Mueller, published in ***Physical Review A 86, 063604 (2012)***.

6. “Magnetic-field dependence of Raman coupling in alkali-metal atoms” by **Ran Wei** and Erich J. Mueller, published in ***Physical Review A 87, 042514 (2013)***.

7. “Theory of bosons in two-leg ladders with large magnetic fields” by **Ran Wei** and Erich J. Mueller, published in ***Physical Review A 89, 063617 (2014)***.

8. “Anomalous charge pumping in a one dimensional optical superlattice” by **Ran Wei** and Erich J. Mueller, published in ***Physical Review A 92, 013609 (2015)***.

CHAPTER 2

LIGHT-INDUCED GAUGE FIELDS

In 2009, Ian Spielman *et al.* from National Standard Institute of Technology (NIST) experimentally realized the first light-induced gauge fields in ultracold atoms [1], drawing great interest from the cold atom community [2, 3]. These fields, known as "synthetic magnetic fields" and "synthetic spin-orbit coupling", are analogous to real fields arising from the gauge symmetry of Lagrangian. They are generated by two "Raman" laser light, which effectively couple to neutral atoms in the same way real fields couple to charged particles and spins. In this chapter, I will discuss the origin of these fields in both homogeneous gases and optical lattices.

2.1 Raman processes in alkali atoms

The key ingredient of light-induced gauge fields is the Raman process [4], a two-photon process induced by atom-light interactions. This process can be understood in the context of a single three-level atom interacting with two sets of laser light, which couple two ground states to the same excited state. In the following I will describe the Raman process through this example of a three level atom, and then extend it to a more realistic example of a 2+N level atom, where N ($N > 1$ for alkali atoms) is the number of excited states.

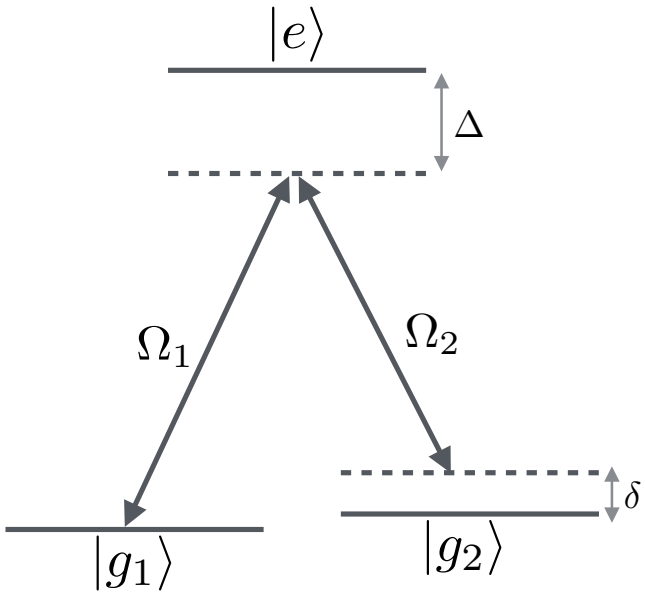

Figure 2.1: Schematic graph of energy levels of a Λ-type atom coupled by two laser light with Rabi frequencies Ω_1 and Ω_2.

2.1.1 Three level system

We start with a single Λ-type atom, coupled by two laser light with frequencies ω_1 and ω_2, where two ground states $|g_1\rangle$ and $|g_2\rangle$ (of energies E_{g_1} and E_{g_2}) are coupled to an excited state $|e\rangle$ (of energy E_e) respectively, as shown in Fig. 2.1. We assume the spontaneous decay rate for the excited state is γ. The Hamiltonian in rotating frame is written as

$$H = \delta\, g_2^\dagger g_2 + (\Delta - i\gamma)\, e^\dagger e + \frac{1}{2}\left(\Omega_1\, e^\dagger g_1 + \Omega_2\, e^\dagger g_2 + H.c.\right) \tag{2.1}$$

where $g_i^\dagger$ $(i = 1, 2)$ creates the ground state $|g_i\rangle = g_i^\dagger |\text{vac}\rangle$, and $e^\dagger$ creates the excited state $|e\rangle = e^\dagger |\text{vac}\rangle$, where $|\text{vac}\rangle$ is the vacuum state. The single-photon detuning is defined by $\Delta = \left(E_e - E_{g_1}\right) - \omega_1$, corresponding to the energy of atomic excited state (in the rotating frame), and the two-photon detuning is defined by $\delta = \left(E_{g_1} - E_{g_2}\right) - (\omega_1 - \omega_2)$, corresponding to the energy of the second atomic ground state (in the rotating frame). The optical Rabi frequency $\Omega_i = \boldsymbol{E}_i \cdot \langle g_i |\, \boldsymbol{d}\, | e \rangle$

characterizes the individual transition element between the ground state $|g_i\rangle$ and the excited state $|e\rangle$, where electronic dipole is $\boldsymbol{d} = e\boldsymbol{r}$, and $\boldsymbol{E}_i$ is electric field of the laser light. Throughout **chapters 2–4**, we set the Plank's constant $\hbar = 1$.

In the limit of $\Delta \gg \{\gamma, \delta, \Omega_1, \Omega_2\}$, the eigenstate of the Hamiltonian is superpositions of $|g_1\rangle$ and $|g_2\rangle$, and a Raman process is characterized by the effective Hamiltonian projected on these two ground states. Using the degenerate perturbation theory shown in the **Appendix 2.4.1**, one obtains

$$H_{\text{eff}} = -\delta\,\hat{\sigma}_{g_2g_2} + \frac{1}{2}\left(\delta_{g_1}\hat{\sigma}_{g_1g_1} + \delta_{g_2}\hat{\sigma}_{g_2g_2} + \Omega\,\hat{\sigma}_{g_1g_2} + \Omega^*\hat{\sigma}_{g_2g_1}\right), \tag{2.2}$$

where:

(1) Real diagonal elements

$$\delta_{g_1} \equiv \text{Re}\left(\frac{|\Omega_1|^2}{4\,(\Delta - i\gamma)}\right) \approx \frac{|\Omega_1|^2}{4\Delta}, \quad \delta_{g_2} \equiv \text{Re}\left(\frac{|\Omega_2|^2}{4\,(\Delta - i\gamma)}\right) \approx \frac{|\Omega_2|^2}{4\Delta} \tag{2.3}$$

are the "AC" Stark shifts of the two ground states.

(2) Imaginary diagonal elements

$$\Gamma_{g_1} \equiv \text{Im}\left(\frac{|\Omega_1|^2}{4\,(\Delta - i\gamma)}\right) \approx \frac{\gamma\,|\Omega_1|^2}{4\Delta^2}, \quad \Gamma_{g_2} \equiv \text{Im}\left(\frac{|\Omega_2|^2}{4\,(\Delta - i\gamma)}\right) \approx \frac{\gamma\,|\Omega_2|^2}{4\Delta^2} \tag{2.4}$$

are the inelastic scattering rates (decay rates) of the two ground states.

(3) The real off-diagonal element

$$\Omega \equiv \frac{\Omega_1^*\Omega_2}{2\,(\Delta - i\gamma)} \approx \frac{\Omega_1^*\Omega_2}{2\Delta} \tag{2.5}$$

is the Raman coupling rate between the two ground states. The fact that Ω is proportional to both Ω_1 and Ω_2 means the Raman process is a two-photon process.

In practice, we wish to have a large Ω and a small Γ_g. Since both Ω and Γ_g are proportional to the second order of Ω_1 or Ω_2, the key figure of merit is the

ratio of them, i.e., $\beta \equiv \Omega/\Gamma_g \sim \Delta/\gamma$ [5]. We see that β does not have an upper bound, as one can arbitrarily increases Δ by tuning the laser frequency. In a realistic system however, β is bounded by the fine structure splitting of alkali atoms. Section 2.1.2 explores this bound.

2.1.2 2+N level system

We extend Eq. (2.3)-(2.5) to the case of a 2+N level system, where N ($N > 1$) is the number of excited states. Assuming all the excited states are decoupled from each another, the effective Hamiltonian can be identified as the sum of N three level systems, where each subsystem consists of states $\{|g_1\rangle, |g_2\rangle, |e_i\rangle\}$, with excited state labeled by $|e_i\rangle$ ($i = 1, 2, ..., N$). This yields:

(1) AC Stark shifts

$$\delta_{g_1} = \sum_{j=1}^{N} \frac{\left|\Omega_{1j}\right|^2}{4\Delta_j}, \quad \delta_{g_2} = \sum_{j=1}^{N} \frac{\left|\Omega_{2j}\right|^2}{4\Delta_j}. \tag{2.6}$$

(2) Inelastic scattering rates

$$\Gamma_{g_1} = \sum_{j=1}^{N} \frac{\gamma_j \left|\Omega_{1j}\right|^2}{4\Delta_j^2}, \quad \Gamma_{g_2} = \sum_{j=1}^{N} \frac{\gamma_j \left|\Omega_{2j}\right|^2}{4\Delta_j^2}. \tag{2.7}$$

(3) Raman coupling

$$\Omega = \sum_{j=1}^{N} \frac{\Omega_{1j}^* \Omega_{2j}}{2\Delta_j}, \tag{2.8}$$

where the single-photon detuning to the excited state is $\Delta_i = \left(E_{e_i} - E_{g_1}\right) - \omega_1$, the spontaneous decay rate is γ_i, and Ω_{1i} and Ω_{2i} are the Rabi couplings between $|g_1\rangle$ and $|e_i\rangle$, and $|g_2\rangle$ and $|e_i\rangle$.

For a typical Raman experiment in cold atoms, the excited states are in the $J = 1/2$ and $J = 3/2$ manifolds, where J is the angular momentum of an alkali atom, labeling the fine structure states. The transition lines between the ground states and the excited states from these two manifolds are called D1 and D2 lines. Since the fine structure splitting is much greater than the hyperfine structure splitting (the energy splitting within J manifolds), one can group Eq. (2.8) into two terms, with one from D1 lines and the other from D2 lines,

$$\Omega = \sum_{j=1}^{N_1} \frac{\Omega_{1j}^* \Omega_{2j}}{2\Delta} + \sum_{j=N_1+1}^{N} \frac{\Omega_{1j}^* \Omega_{2j}}{2\left(\Delta + A_f\right)} \tag{2.9}$$

where A_f is the fine structure splitting between the $J = 1/2$ and $J = 3/2$ manifolds, and N_1 is the number of states in the $J = 1/2$ manifold. This expression can be simplified by noting that the ground state quadrupole matrix element satisfies $\langle g_1 | d_a d_b | g_2 \rangle = 0$ unless $a = b$ $(a, b = x, y, z)$. This reflects the spherical symmetry of the electron wavefunction, and the fact that the electronic dipole does not couple to spin. Inserting a complete set of exited states, the dipole transitions shall satisfy the identity $\sum_{j=1}^{N_1} \Omega_{1j}^* \Omega_{2j} + \sum_{j=N_1+1}^{N} \Omega_{1j}^* \Omega_{2j} = 0$. This allows us to write Eq. (2.9) solely in terms of D1 transitions,

$$\Omega = \frac{A_f}{2\Delta\left(\Delta + A_f\right)} \sum_{j=1}^{N_1} \Omega_{1j}^* \Omega_{2j}. \tag{2.10}$$

For $\Delta \gg A_f$, the Raman coupling scales as $\Omega \sim A_f/\Delta^2$. In this case, $\beta \equiv \Omega/\Gamma_g \sim A_f/\gamma$ is bounded by the fine structure splitting. Typically, heavier alkali atoms have larger fine structure splittings, and thus β is larger. Detailed calculations on different alkali atoms can be found in **chapter 9**.

2.1.3 Momentum transferred by Raman laser

We have shown that light from two Raman laser, can effectively couple two atomic internal states through a virtual two-photon process. To derive an effective gauge field we have to consider the momentum carried by photons, which is implicit in the spatial dependence of the laser fields.

To include this spatial dependence, one takes the Rabi frequencies, $\Omega_1 \rightarrow \Omega_1 e^{i\boldsymbol{k}_1\cdot\boldsymbol{r}}$, $\Omega_2 \rightarrow \Omega_2 e^{i\boldsymbol{k}_2\cdot\boldsymbol{r}}$, and $\Omega \rightarrow \Omega e^{i(\boldsymbol{k}_2-\boldsymbol{k}_1)\cdot\boldsymbol{r}}$, where $\boldsymbol{k}_1$ and $\boldsymbol{k}_2$ are the wave vectors (momenta) of two laser light. The momentum difference $\delta\boldsymbol{k} = \boldsymbol{k}_2 - \boldsymbol{k}_1$ represents the momentum transferred to an atom in a two-photon Raman process – an atom absorbs one photon with momentum $\boldsymbol{k}_2$ and emits one photon with momentum $\boldsymbol{k}_1$. The recoil momentum is largest when two laser light are counter-propagating. In the following I will derive the gauge fields from the Raman coupling $\Omega e^{i(\boldsymbol{k}_2-\boldsymbol{k}_1)\cdot\boldsymbol{r}}$.

2.2 Light-induced spin-orbit coupling

I first discuss one type of gauge field – spin-orbit coupling (SOC). I emphasize that SOC is NOT the coupling between the electronic spin and angular momentum which naturally exists in an atom, but instead the coupling between atomic motion and atomic hyperfine states. It is analogous to the spin-orbit coupling ubiquitous in condense matter systems (known as Rashba or Dresselhaus spin-orbit coupling [7, 8]). I will focus on the SOC generated in Spielman's experiments [6], known as the one dimensional SOC with an equal combination of Rashba and Dresselhaus types.

Starting from Eq. (2.2), we include the kinetic energy of an atom and subtract the unimportant constant, and the Hamiltonian is expressed as

$$\bar{H} = -\frac{1}{2m}\partial_x^2 + \frac{\delta}{2}\left(\hat{\sigma}_{\uparrow\uparrow} - \hat{\sigma}_{\downarrow\downarrow}\right) + \frac{\Omega}{2}e^{2ik_R x}\hat{\sigma}_{\uparrow\downarrow} + \frac{\Omega}{2}e^{-2ik_R x}\hat{\sigma}_{\downarrow\uparrow}, \tag{2.11}$$

where $|\uparrow\rangle$ and $|\downarrow\rangle$ represent the two atomic ground states. Here we have assumed two laser light are counter-propagating in the x-direction ($-k_1 = k_2 = k_R$) and neglect the decay rate ($\gamma = 0$). In the Pauli matrices representation, the Hamiltonian is written as

$$\bar{H} = -\frac{1}{2m}\partial_x^2 + \frac{\delta}{2}\sigma_z + \frac{\Omega}{2}\cos 2k_R x\,\hat{\sigma}_x - \frac{\Omega}{2}\sin 2k_R x\,\hat{\sigma}_y. \tag{2.12}$$

To eliminate the spatial dependence of the off-diagonal terms, we apply a unitary transformation $U = e^{i k_R x \hat{\sigma}_z} = \cos(k_R x) + i \sin(k_R x)\,\hat{\sigma}_z$, which yields

$$H = U^{-1}\bar{H}U = \frac{1}{2m}\left(-\partial_x^2 - ik_R\partial_x\sigma_z + k_R^2\right) + \frac{\delta}{2}\sigma_z + \frac{\Omega}{2}\sigma_x. \tag{2.13}$$

Replacing $-i\partial_x$ with $\hat{k}$, we obtain

$$H = \frac{\hat{k}^2}{2m} + \frac{k_R}{m}\hat{\sigma}_z\hat{k} + \frac{\Omega}{2}\hat{\sigma}_x + \frac{\delta}{2}\hat{\sigma}_z + \frac{k_R^2}{2m}. \tag{2.14}$$

To notationally comply with the Hamiltonian in condense matter system, we perform a spin rotation $\hat{\sigma}_z \to \hat{\sigma}_y, \hat{\sigma}_y \to \hat{\sigma}_x, \hat{\sigma}_x \to \hat{\sigma}_z$, yielding

$$H = \frac{\hat{k}^2}{2m} + \frac{k_R}{m}\hat{\sigma}_y\hat{k} + \frac{\Omega}{2}\hat{\sigma}_z + \frac{\delta}{2}\hat{\sigma}_y + \frac{k_R^2}{2m}. \tag{2.15}$$

This Hamiltonian was experimentally realized in NIST [6], where the second term is the spin-orbit coupled (SOC) interaction, with σ_y representing the spin (in the y-direction), $\hat{k}$ representing the orbit (in the x-direction), and k_R/m characterizing the coupling strength. The third term is the Zeeman term, with σ_z representing the spin (in the z-direction), and Ω characterizing the Zeeman coupling strength. The SOC interaction is one dimensional, consisting of equal contributions of Rashba coupling ($\sigma_x\hat{k}_y - \sigma_y\hat{k}_x$) and Dresselhaus coupling ($-\sigma_x\hat{k}_y - \sigma_y\hat{k}_x$)

[7, 8]. Since the interaction preserves the spin rotational symmetry in the y-direction (U(1) symmetry), it corresponds to an Abelian gauge field [9]. I will show in **chapter 8** that this gauge field can give rise to interesting physics. Note two groups from China have recently realized a two dimensional non-Abelian SOC [10, 11].

2.3 Light-induced magnetic field

Here I introduce another type of gauge fields – light-induced magnetic fields. I will discuss how these fields are produced in both homogenous gases [1] and optical lattices [12, 13, 14, 15].

2.3.1 Homogenous case

The magnetic field in homogenous gases can be understood from Eq. (2.14). Replacing $\hat{k} \to k$, the Hamiltonian is simply represented by a 2 by 2 matrix and can be readily diagonalized: Moving the two identity matrices to the left and squaring both sides of Eq. (2.14), we arrive

$$\left(H - \frac{k^2 + k_R^2}{2m}\right)^2 = \left(\left(\frac{k_R k}{m} + \frac{\delta}{2}\right)\hat{\sigma}_z + \frac{\Omega}{2}\hat{\sigma}_x\right)^2 = \left(\frac{k_R k}{m} + \frac{\delta}{2}\right)^2 + \frac{\Omega^2}{4}. \tag{2.16}$$

Extracting the characteristic polynomial, we obtain the dispersions of two dressed states

$$E_\pm(k) = \frac{k^2 + k_R^2}{2m} \pm \sqrt{\left(\frac{k_R k}{m} + \frac{\delta}{2}\right)^2 + \frac{\Omega^2}{4}}, \tag{2.17}$$

as shown in Fig. 2.2. We see the quasi-momentum of the lowest energy state

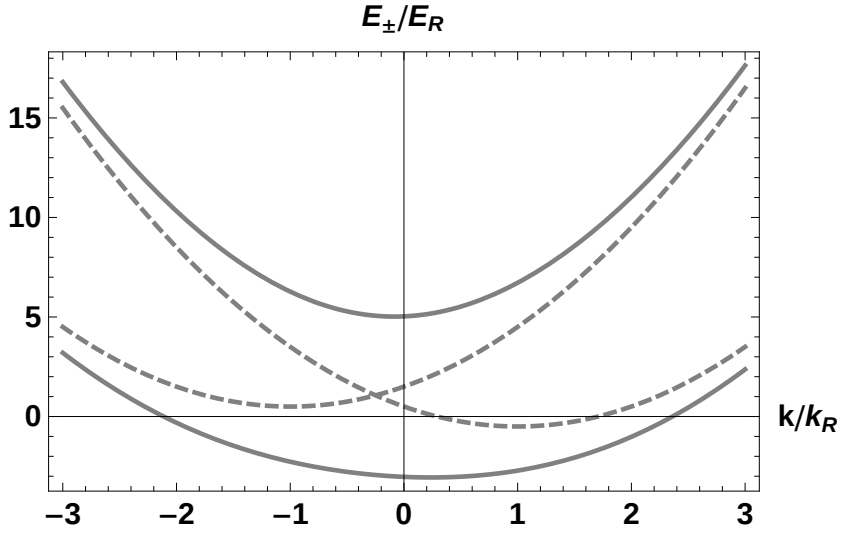

Figure 2.2: Dispersions (solid lines) of two dressed states plotted from Eq. (2.17), where the minima of the two bands are shifted away from zero, creating the effective vector potentials. Here the parameters are $\Omega = 8E_R, \delta = -E_R$, with $E_R = k_R^2/2m$ the recoil energy. The dashed lines represent two bare states ($\Omega = 0$).

is shifted away from zero, creating an effective vector potential for each energy band [4]. Since the momentum shift can not be greater than the recoil momentum k_R, the vector potential is bounded by $-k_R \leq A \leq k_R$. Note the real momentum is still zero.

To analytically calculate these potentials, we expand the dispersions to first order in $(2k_R k/m + \delta)/\Omega$, yielding

$$E_\pm(k) = \frac{1 \pm 2k_R^2/m\Omega}{2m}\left(k^2 \pm \frac{2k_R\delta}{\Omega \pm 2k_R^2/m}k\right) \pm \frac{\Omega}{2} \pm \frac{\delta^2}{4\Omega} + \frac{k_R^2}{2m}. \tag{2.18}$$

In the limit of $\Omega \gg 2k_R^2/m$, Eq. (2.18) can be written as

$$E_\pm(k) = \frac{1}{2m}(k \pm A)^2 \pm C. \tag{2.19}$$

where $A = k_R\delta/\Omega$ is the effective vector potential in the x-direction, and C is a k-independent constant. This dispersion is formally the same as the Hamiltonian of charged particles of mass m in electromagnetic vector potentials A. Here the

two vector potentials have opposite signs but equal magnitude, corresponding to opposite "charges" for the two energy bands.

To produce a magnetic field, we include the y-component in the Hamiltonian. Rewriting the dispersions in real space, one obtains

$$H_{\pm} = \frac{1}{2m}\left(-i\partial_x \pm A\right)^2 - \frac{1}{2m}\partial_y^2 \pm C. \tag{2.20}$$

When δ is y-dependent, the curl of the vector potential A yields a non-vanishing magnetic field in the z-direction (Landau gauge), i.e., $B_z = -\partial_y A = -\left(k_R/\Omega\right)\delta_y$, where the detuning gradient δ_y can be generated from an inhomogeneous Zeeman field [1].

While the vector potential is bounded, the magnetic field can be arbitrarily large (as δ_y is not bounded). In such case, the field only exists in a narrow region – the larger the field, the narrower the region [16]. Studies of interacting gases in large magnetic fields on narrow geometries can be found in **chapter 5–6**.

2.3.2 Optical lattice

In this section, I will discuss how Raman processes are used to generate magnetic fluxes on optical lattices. In contrast to the homogenous case, the fields created on lattices are not bounded and can be extremely strong over the entire lattice [17]. This is particularly exciting not only because large fields can lead to rich phenomena such as fractional quantum Hall effect, but more interestingly they open up the possibility of exploring the fractal energy spectrum predicted by D. R. Hofstadter [19]. This might lead to uncharted territory that is not accessible in electron systems [20].

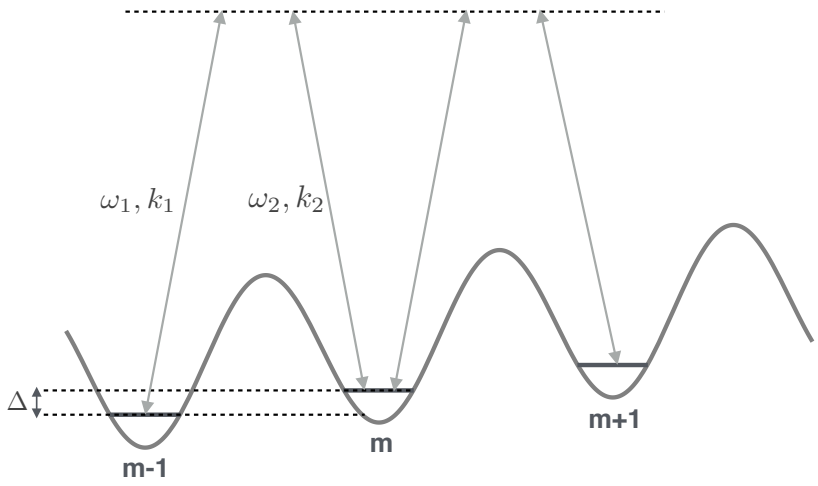

Figure 2.3: Raman-assist tunneling in the lowest band of a tilt lattice. The energy offset between neighboring sites is $\Delta = \omega_1 - \omega_2$, where ω_1 and ω_2 are the frequencies of the two laser light. The bandwidth of the lattice is much smaller than Δ, so the tunneling is prohibited without the Raman light. When the Raman light is on, tunneling is restored.

Uniform fields

We first consider the following time-dependent tight-binding Hamiltonian,

$$\begin{aligned} H &= -J_x \sum_{m,n} \left(b^\dagger_{m+1,n} b_{m,n} + H.c. \right) - J_y \sum_{m,n} \left(b^\dagger_{m,n+1} b_{m,n} + H.c. \right) \\ &+ \sum_{m,n} m\Delta \, b^\dagger_{m,n} b_{m,n} + \sum_{m,n} \Omega \sin\left(\omega t - \phi_{m,n}\right) b^\dagger_{m,n} b_{m,n}. \end{aligned} \tag{2.21}$$

The first two terms describe a regular two dimensional optical lattice, where the operator $b^\dagger_{m,n}$ ($b_{m,n}$) creates (annihilates) a particle at lattice site $\{m, n\}$, and J_x and J_y represent the tunnelings between neighboring sites along the x-direction and y-direction. The third term describes a tilted potential, where the energy offset on neighboring sites is Δ. This potential is produced by the gravity in Refs. [13, 14]. Note the tunneling in the y-direction is not effected by Δ. The fourth term is a Raman light-induced running potential, where Ω is the Raman Rabi frequency, $\omega = \omega_1 - \omega_2$ and $\boldsymbol{k} = \boldsymbol{k}_1 - \boldsymbol{k}_2$ are the frequency and momentum differences of the two light, and $\phi_{m,n} = \boldsymbol{k} \cdot \boldsymbol{R}_{m,n} = mk_x a + nk_y a$ is a periodic phase

factor, with a the lattice constant. We consider the limit where the bandwidth in the x-direction is much smaller than the potential tilt ($J_x \ll \Delta$), so the tunneling (in the x-direction) is forbidden without the Raman light.

While the Hamiltonian does not explicitly include a magnetic field, I will show that the low energy effective model is a Harper Hamiltonian, which describes a two dimensional lattice in a static magnetic field [18].

Given that the Hamiltonian in Eq. (2.21) is periodic in time, one could calculate the evolution operator $\mathcal{U}(T) = \mathcal{T} e^{-i\int_0^T d\tau\, H(\tau)}$ in one period ($T = 2\pi/\omega$), and extract the effective Hamiltonian from $\mathcal{U}(T) = e^{-iH_{\text{eff}}T}$.

We first perform a unitary transformation to eliminate the large terms in Eq. (2.21),

$$U(t) = \exp\left(-\sum_{m,n} i\,\chi_{m,n}(t)\, b^\dagger_{m,n} b_{m,n}\right), \tag{2.22}$$

where

$$\chi_{m,n}(t) = m\Delta\, t - \frac{\Omega}{\omega}\cos\left(\omega t - \phi_{m,n}\right) + \frac{m k_x a}{2}. \tag{2.23}$$

Under the new basis, the Hamiltonian becomes

$$\begin{aligned} \bar{H} &= UHU^{-1} - iU\partial_t U^{-1} \qquad (2.24)\\ &= -J_x \sum_{m,n}\left(e^{-i\Phi_{m+1,n}(t)} b^\dagger_{m+1,n} b_{m,n} + H.c.\right) - J_y \sum_{m,n}\left(e^{-i\Phi_{m,n+1}(t)} b^\dagger_{m,n+1} b_{m,n} + H.c.\right), \end{aligned}$$

where we have defined

$$\Phi_{m+1,n}(t) = \chi_{m+1,n}(t) - \chi_{m,n}(t) = \Delta\, t - \frac{\Omega}{\omega}\xi_{m+1,n}(t) + \frac{k_x a}{2} \tag{2.25}$$

$$\Phi_{m,n+1}(t) = \chi_{m,n+1}(t) - \chi_{m,n}(t) = -\frac{\Omega}{\omega}\xi_{m,n+1}(t) \tag{2.26}$$

$$\xi_{m+1,n}(t) = 2\sin\left(\omega t + \frac{\phi_{m+1,n} + \phi_{m,n}}{2}\right)\sin\left(\frac{k_x a}{2}\right) \tag{2.27}$$

$$\xi_{m,n+1}(t) = 2\sin\left(\omega t + \frac{\phi_{m,n+1} + \phi_{m,n}}{2}\right)\sin\left(\frac{k_y a}{2}\right). \tag{2.28}$$

We now expand the evolution operator to first order in J/ω, which corresponds to writing $\mathcal{U}(T) = e^{-i\int_0^T d\tau\, \bar{H}(\tau)} = e^{-iH_{\text{eff}}T}$. This leads to

$$H_{\text{eff}} = \frac{1}{T}\int_0^T d\tau\, \bar{H}(\tau). \tag{2.29}$$

The only time-dependent terms are $e^{-i\Phi_{m+1,n}(t)}$ and $e^{-i\Phi_{m,n+1}(t)}$. At $\omega = \Delta$, the average of these two terms have the following closed forms,

$$\begin{aligned}
\frac{1}{T}\int_0^T d\tau\, e^{-i\Phi_{m+1,n}(\tau)} &= \frac{e^{i\phi_{m,n}}}{2\pi}\int_0^{2\pi} d\tau \exp\left(-i\left(\tau - \left(\frac{2\Omega}{\Delta}\sin\frac{k_x a}{2}\right)\sin\tau\right)\right) && (2.30)\\
&= e^{i\phi_{m,n}}\mathcal{J}_1\left(\frac{2\Omega}{\Delta}\sin\left(\frac{k_x a}{2}\right)\right) && (2.31)\\
\frac{1}{T}\int_0^T d\tau\, e^{-i\Phi_{m,n+1}(\tau)} &= \frac{1}{2\pi}\int_0^{2\pi} d\tau \exp\left(\left(\frac{2\Omega}{\Delta}\sin\frac{k_y a}{2}\right)\sin\tau\right) && (2.32)\\
&= \mathcal{J}_0\left(\frac{2\Omega}{\Delta}\sin\left(\frac{k_y a}{2}\right)\right), && (2.33)
\end{aligned}$$

where $\mathcal{J}_0(x)$ and $\mathcal{J}_1(x)$ are the Bessel functions of the first kind. The effective Hamiltonian is then expressed as

$$H_{\text{eff}} = -K\sum_{m,n}\left(e^{i\phi_{m,n}}b^\dagger_{m+1,n}b_{m,n} + H.c.\right) - J\sum_{m,n}\left(b^\dagger_{m,n+1}b_{m,n} + H.c.\right) \tag{2.34}$$

where

$$\begin{aligned}
K &= J_x\mathcal{J}_1\left(\frac{2\Omega}{\Delta}\sin\left(\frac{k_x a}{2}\right)\right) && (2.35)\\
J &= J_y\mathcal{J}_0\left(\frac{2\Omega}{\Delta}\sin\left(\frac{k_y a}{2}\right)\right). && (2.36)
\end{aligned}$$

Note in the limit of $\Omega \ll \Delta$, one has

$$\begin{aligned}
K &= J_x\left(\frac{\Omega}{\Delta}\sin\frac{k_x a}{2} + O\left[\frac{\Omega}{\Delta}\right]^3\right) \approx \frac{J_x\Omega}{\Delta}\sin\frac{k_x a}{2} && (2.37)\\
J &= J_y\left(1 + O\left[\frac{\Omega}{\Delta}\right]^2\right) \approx J_y. && (2.38)
\end{aligned}$$

The scaling of K ($\sim J_x\Omega/\Delta$) is reminiscent of a second-order perturbation process, where neighboring sites are effectively coupled by Ω and J_x through a virtual site with an energy offset Δ.

Eq. (2.34) describes a two dimensional lattice in a magnetic field, where the site-dependent phase (Peierls phase) $\phi_{m,n} = mk_x a + nk_y a$ gives rise to a magnetic flux $\phi_f = k_y a$ per plaquette. Since ϕ_f is only defined modulo 2π, the largest magnetic field is at $\phi_f = k_y a = \pi$. Note the tunneling in the x-direction vanishes when $k_x a = 0$, so one shall keep both $k_x a$ and $k_y a$ finite. In experiments, one can easily vary ϕ_f from zero to π either by changing ω and Δ simultaneously, or by tuning the angle between the pair of Raman light. These magnetic fluxes ϕ_f correspond to the effective magnetic fields ranging from zero to thousands of Tesla in electrons [17].

Fields with patterns

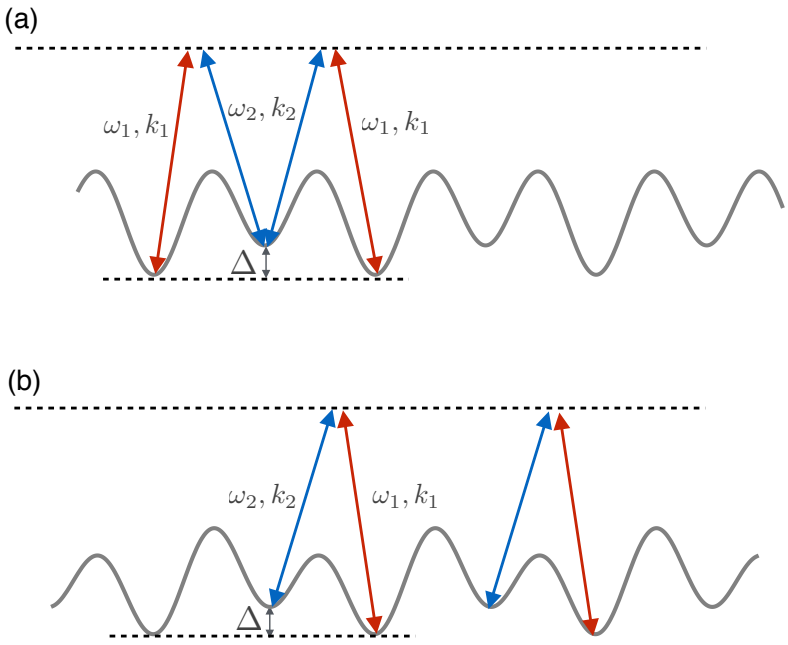

Figure 2.4: Raman-assist tunneling on superlattices. In (a), sublattice has a reflection symmetry, but the sign of recoil momenta alternates, yielding a staggered magnetic field. In (b), sublattice does not have a reflection symmetry, and lattice is broken into a bundle of decoupled "two-leg ladders".

By changing the lattice structure, experimentalists can even design patterns for these large magnetic fields. For example, they have produced a field that reverses direction from odd-number sites to even-number sites [12]. This "staggered" field exists in models of spin liquids and strongly correlated electron systems, and can thus be of great interest in condense matter community [17]. The same group also produced a bundle of decoupled "two-leg ladders" [15], which can be served as a toy model to understand two dimensional systems.

Concretely, these patterns are realized in the optical superlattice $V_{\text{latt}}(x) = V_1\cos(2\pi x/a) + V_2\cos(\pi x/a + \varphi)$. This potential has a period of $2a$, with two distinct configurations, as shown in Fig. 2.4. When $\varphi = \pi/2$, a unit cell has reflection symmetry (see Fig. 2.4(a)). In this case, the tunneling amplitude is the same between neighboring sites, but the sign of recoil momenta alternates, yielding a "staggered" magnetic field. When $\varphi \neq \pi/2$, a unit cell has broken reflection symmetry (see Fig. 2.4(b)). In this case, there is a large potential barrier between two neighboring cells, breaking a two dimensional lattice into a bundle of decoupled "two-leg ladders". In **chapter 7**, we will study the ground states of interacting Bose gases on a two-leg ladder.

2.4 Appendix

2.4.1 Effective Hamiltonian for a Raman process

Here we derive a low energy effective Hamiltonian for Eq. (2.1) in the limit $\Delta \gg \{\gamma, \delta, \Omega_1, \Omega_2\}$. We aim to eliminate the excited state and find an effective Hamiltonian in the ground state basis. To make the derivations mathematically

compact, we introduce the projection operators

$$P = |g_1\rangle\langle g_1| + |g_2\rangle\langle g_2|, \tag{2.39}$$

$$Q = 1 - P = |e\rangle\langle e|. \tag{2.40}$$

These two operators break a state $|\psi\rangle$ into two parts,

$$|\psi\rangle = P|\psi\rangle + Q|\psi\rangle \equiv |\psi_0\rangle + |\psi_{\text{ex}}\rangle, \tag{2.41}$$

where $|\psi_0\rangle$ represents the low-energy sector, and $|\psi_{\text{ex}}\rangle$ represents the high-energy sector. The eigen-equation $H|\psi\rangle = E|\psi\rangle$ is then divided into two equations

$$PH|\psi\rangle = PE|\psi\rangle = E|\psi_0\rangle, \tag{2.42}$$

$$QH|\psi\rangle = QE|\psi\rangle = E|\psi_{\text{ex}}\rangle. \tag{2.43}$$

Inserting the identity $P^2 + Q^2 = P + Q = 1$ on the left hand side of Eq. (2.42)-(2.43) and substituting $|\psi_{\text{ex}}\rangle$ in terms of $|\psi_0\rangle$, we obtain a closed equation for $|\psi_0\rangle$,

$$H_{\text{eff}}|\psi_0\rangle = E|\psi_0\rangle, \tag{2.44}$$

where the effective Hamiltonian in the low-energy sector is

$$H_{\text{eff}} \equiv PHP + PHQ\frac{1}{E - QHQ}QHP. \tag{2.45}$$

Writing out each term explicity

$$PHQ = \frac{1}{2}\left(\Omega_1^*\hat{\sigma}_{g_1e} + \Omega_2^*\hat{\sigma}_{g_2e}\right), \quad QHP = \frac{1}{2}\left(\Omega_1\hat{\sigma}_{eg_1} + \Omega_2\hat{\sigma}_{eg_2}\right), \tag{2.46}$$

$$PHP = \delta\hat{\sigma}_{g_2g_2}, \quad QHQ = (\Delta - i\gamma)\,\hat{\sigma}_{ee}, \tag{2.47}$$

we obtain the effective Hamiltonian

$$H_{\text{eff}} = \delta\hat{\sigma}_{g_2g_2} + \left(\Omega_1^*\hat{\sigma}_{g_1e} + \Omega_2^*\hat{\sigma}_{g_2e}\right)\frac{1}{4\left(E - (\Delta - i\gamma)\,\hat{\sigma}_{ee}\right)}\left(\Omega_1\hat{\sigma}_{eg_1} + \Omega_2\hat{\sigma}_{eg_2}\right), \tag{2.48}$$

where $\hat{\sigma}_{ab} \equiv |a\rangle\langle b|$. We are interested in the low-energy limit, where $|E| \ll |\Delta - i\gamma|$, yielding the Hamiltonian (multiplied by a negative sign)

$$H_{\text{eff}} = -\delta\,\hat{\sigma}_{g_2g_2} + \frac{1}{2}\left(\delta_{g_1}\hat{\sigma}_{g_1g_1} + \delta_{g_2}\hat{\sigma}_{g_2g_2} + \Omega\,\hat{\sigma}_{g_1g_2} + \Omega^*\hat{\sigma}_{g_2g_1}\right). \tag{2.49}$$

CHAPTER 3

MEAN-FIELD THEORY FOR DEGENERATE GASES

This chapter is a short introduction to the basic mean-field theories used to describe superfluid gases: Gross-Pitaevski and Bogoliubov-de Gennes equations. While these theories have many different representations, I will be focusing on variational wavefunction and BdG equation approaches. Applications of these approaches are discussed in **chapters 5–8**. For more comprehensive introductions to mean-field theories on degenerate quantum gases, one can refer to Refs. [21, 22].

3.1 Interaction

One of the most distinct features in cold atoms is that interactions between two particles are short-ranged compared to inter-particle spacing. This allows us to model the effective interaction by a delta function $V(\boldsymbol{r} - \boldsymbol{r}') = g\,\delta(\boldsymbol{r} - \boldsymbol{r}')$, where $g = 4\pi a/m$ characterizes the interaction strength, and a is the s-wave scattering length and m is the mass of an atom. Since the delta function can only capture the low energy physics, a high energy cut-off needs to be imposed. In particular one writes $1/g = m/(4\pi a) - \sum_{\boldsymbol{k}} \epsilon_{\boldsymbol{k}}/(2V)$, where V is the system volume, $\epsilon_{\boldsymbol{k}}$ is the excitation spectrum, and the sum is over modes below the cutoff [21]. Note this renormalization is unnecessary in 1D, where high energy modes are less important. In 1D, one writes $g = 4\pi a_{1\mathrm{D}}/m$, with $a_{1\mathrm{D}}$ the one dimensional scattering length [23].

In cold atoms, a particle has an internal (pseudo) "spin" degree of freedom, so collisions can also happen between different spins. In this thesis, we will

focus on spin-1/2 gases, where the many-body interaction is written as

$$\begin{aligned} H_{\text{int}} &= \frac{1}{2}\int d\mathbf{r}\Big(g_{\uparrow\uparrow}\,\psi_\uparrow^\dagger(\boldsymbol{r})\,\psi_\uparrow^\dagger(\boldsymbol{r})\,\psi_\uparrow(\boldsymbol{r})\,\psi_\uparrow(\boldsymbol{r}) + g_{\downarrow\downarrow}\,\psi_\downarrow^\dagger(\boldsymbol{r})\,\psi_\downarrow^\dagger(\boldsymbol{r})\,\psi_\downarrow(\boldsymbol{r})\,\psi_\downarrow(\boldsymbol{r}) \\ &+ 2g_{\uparrow\downarrow}\,\psi_\uparrow^\dagger(\boldsymbol{r})\,\psi_\downarrow^\dagger(\boldsymbol{r})\,\psi_\downarrow(\boldsymbol{r})\,\psi_\uparrow(\boldsymbol{r})\Big), \end{aligned} \tag{3.1}$$

where $\psi_\sigma^\dagger(\boldsymbol{r})$ ($\psi_\sigma(\boldsymbol{r})$) creates (annihilates) a σ state at position $\boldsymbol{r}$. In most Bose-Einstein condensate (BEC) experiments, one has $g_{\uparrow\uparrow} = g_{\downarrow\downarrow} = g_{\uparrow\downarrow}$. For degenerate Fermi gases, the Pauli exclusion principle leads to $g_{\uparrow\uparrow} = g_{\downarrow\downarrow} = 0$.

It's also useful to express the Hamiltonian in momentum space,

$$\begin{aligned} H_{\text{int}} &= \frac{1}{2V}\sum_{\boldsymbol{k},\boldsymbol{q},\boldsymbol{q}'}\Big(g_{\uparrow\uparrow}a^\dagger_{\boldsymbol{k}/2+\boldsymbol{q}\uparrow}a^\dagger_{\boldsymbol{k}/2-\boldsymbol{q}\uparrow}a_{\boldsymbol{k}/2-\boldsymbol{q}'\uparrow}a_{\boldsymbol{k}/2+\boldsymbol{q}'\uparrow} \\ &+ g_{\downarrow\downarrow}a^\dagger_{\boldsymbol{k}/2+\boldsymbol{q}\downarrow}a^\dagger_{\boldsymbol{k}/2-\boldsymbol{q}\downarrow}a_{\boldsymbol{k}/2-\boldsymbol{q}'\downarrow}a_{\boldsymbol{k}/2+\boldsymbol{q}'\downarrow} + 2g_{\uparrow\downarrow}a^\dagger_{\boldsymbol{k}/2+\boldsymbol{q}\uparrow}a^\dagger_{\boldsymbol{k}/2-\boldsymbol{q}\downarrow}a_{\boldsymbol{k}/2-\boldsymbol{q}'\downarrow}a_{\boldsymbol{k}/2+\boldsymbol{q}'\uparrow}\Big), \end{aligned} \tag{3.2}$$

where $a_{\boldsymbol{k}} = \left(1/\sqrt{V}\right)\int d\boldsymbol{r}\,\psi_\sigma(\boldsymbol{r})e^{-i\boldsymbol{k}\cdot\boldsymbol{r}}$ and $\psi_\sigma(\boldsymbol{r}) = \left(1/\sqrt{V}\right)\sum_{\boldsymbol{k}\sigma}a_{\boldsymbol{k}\sigma}e^{i\boldsymbol{k}\cdot\boldsymbol{r}}$. Here the index $\boldsymbol{k}$ denotes the center of mass momentum of the many-body system, and $\boldsymbol{q}$ and $\boldsymbol{q}'$ denote the relative momentum.

3.2 Variational wavefunction for Bose-Einstein Condensations

We here discuss one representation of the Gross-Pitaevski mean-field theory – the variational wavefunction approach. The essence of this approach is to find an educated guess of the ground state, and minimize the corresponding energy of respect to variational parameters. A natural guess of a BEC is a coherent state or a Fock state, which can be written as (in momentum space):

$$|\Psi_{\text{coh}}\rangle = \exp\left(-\frac{N}{2} + \sum_{\boldsymbol{k}\sigma}c_{\boldsymbol{k}\sigma}a^\dagger_{\boldsymbol{k}\sigma}\right)|\text{vac}\rangle\,, \tag{3.3}$$

or

$$|\Psi_{\text{Fock}}\rangle = \frac{1}{N_\uparrow!N_\downarrow!}\left(\sum_{\boldsymbol{k}}c_{\boldsymbol{k}\uparrow}a^\dagger_{\boldsymbol{k}\uparrow}\right)^{N_\uparrow}\left(\sum_{\boldsymbol{k}}c_{\boldsymbol{k}\downarrow}a^\dagger_{\boldsymbol{k}\downarrow}\right)^{N_\downarrow}|\text{vac}\rangle\,, \tag{3.4}$$

where N_σ is the number of σ particles, and $N = N_\uparrow + N_\downarrow$ is the total number of particles. The variational parameter $|c_{\boldsymbol{k}\sigma}|^2$ describes the number of σ particles at momentum $\boldsymbol{k}$, which is subjected to the normalization $\sum_{\boldsymbol{k}} |c_{\boldsymbol{k}\sigma}|^2 = N_\sigma$. Both states map an annihilation operator to a c-number: $a_{\boldsymbol{k}\sigma} \left|\Psi_{\text{coh/Fock}}\right\rangle = c_{\boldsymbol{k}\sigma} \left|\Psi_{\text{coh/Fock}}\right\rangle$, which transforms a quantum field into a classical field. Under this "mean-field" approximation, the quantum fluctuation disappears, and the many-body interaction becomes an energy functional,

$$\begin{aligned} E_{\text{int}} &= \left\langle \Psi_{\text{coh/Fock}} \right| H_{\text{int}} \left| \Psi_{\text{coh/Fock}} \right\rangle \\ &= \frac{1}{2V} \sum_{\boldsymbol{k},\boldsymbol{q},\boldsymbol{q}'} \Big(g_{\uparrow\uparrow} c^*_{\boldsymbol{k}/2+\boldsymbol{q}\uparrow} c^*_{\boldsymbol{k}/2-\boldsymbol{q}\uparrow} c_{\boldsymbol{k}/2-\boldsymbol{q}'\uparrow} c_{\boldsymbol{k}/2+\boldsymbol{q}'\uparrow} \\ &+ g_{\downarrow\downarrow} c^*_{\boldsymbol{k}/2+\boldsymbol{q}\downarrow} c^*_{\boldsymbol{k}/2-\boldsymbol{q}\downarrow} c_{\boldsymbol{k}/2-\boldsymbol{q}'\downarrow} c_{\boldsymbol{k}/2+\boldsymbol{q}'\downarrow} + 2 g_{\uparrow\downarrow} c^*_{\boldsymbol{k}/2+\boldsymbol{q}\uparrow} c^*_{\boldsymbol{k}/2-\boldsymbol{q}\downarrow} c_{\boldsymbol{k}/2-\boldsymbol{q}'\downarrow} c_{\boldsymbol{k}/2+\boldsymbol{q}'\uparrow} \Big). \end{aligned} \tag{3.5}$$

The total energy is then given by $E_{\text{tot}} = E_{\text{int}} + E_{\text{quad}}$, where E_{quad} includes all other quadratic energies such as kinetic energy (dispersion) and potential energy. Minimizing E_{tot} respect to $c_{\boldsymbol{k}\sigma}$ leads to the ground state. One shall impose extra symmetries to reduce the number of variational parameters and simplify the calculations. For example, if the system has lattice translational invariance, one can drop the $\boldsymbol{k}$-sum by setting $\boldsymbol{k}$ the minimum of the dispersion. Some of other symmetries will be discussed in **chapter 5**.

3.3 Elementary excitations – Bogoliubov spectrum

Here we study elementary excitations of a single-component BEC, described by the variational wavefunction

$$|\Psi\rangle = \exp\left(-\frac{N}{2} + \sum_{\boldsymbol{k}} c_{\boldsymbol{k}} a^\dagger_{\boldsymbol{k}} \right) |\text{vac}\rangle \,, \tag{3.6}$$

which gives the mean-field energy

$$E_{\text{tot}} = \sum_{\boldsymbol{k}} \frac{k^2}{2m} c^*_{\boldsymbol{k}} c_{\boldsymbol{k}} + \frac{g}{2V} \sum_{\boldsymbol{k},\boldsymbol{q},\boldsymbol{q}'} c^*_{\boldsymbol{k}/2+\boldsymbol{q}} c^*_{\boldsymbol{k}/2-\boldsymbol{q}} c_{\boldsymbol{k}/2-\boldsymbol{q}'} c_{\boldsymbol{k}/2+\boldsymbol{q}'}. \tag{3.7}$$

Since the minimum of the dispersion is at $k = 0$, the lowest energy is obtained when $c_{\boldsymbol{k}} = \sqrt{N}\delta_{k0}$, where δ is the Kronecker delta function. This leads to the ground state energy $E = gN^2/2V$ and the chemical potential $\mu = \partial E/\partial N = gN/V$.

To calculate the elementary excitation, we include the quantum fluctuation by writing $c_{\boldsymbol{k}} = \sqrt{N}\delta_{k0} + (1 - \delta_{k0})\chi_{\boldsymbol{k}}$ and subtract the chemical potential term $\mu \sum_{\boldsymbol{k}} c^*_{\boldsymbol{k}} c_{\boldsymbol{k}}$. The excitation Hamiltonian shall be expressed to the quadratic order in $\chi_{\boldsymbol{k}}$,

$$H_{\text{ex}} = \sum_{k\neq 0} \left(\frac{k^2}{2m} + \frac{gN}{V} \right) \chi^\dagger_{\boldsymbol{k}} \chi_{\boldsymbol{k}} + \frac{gN}{2V} \sum_{k\neq 0} \left(\chi^\dagger_{\boldsymbol{k}} \chi^\dagger_{-\boldsymbol{k}} + \chi_{-\boldsymbol{k}} \chi_{\boldsymbol{k}} \right) + \text{const.} \tag{3.8}$$

$$= \frac{1}{2} \left(\sum_{k\neq 0}{}' \left(\frac{k^2}{2m} + \frac{gN}{V} \right) \left(\chi^\dagger_{\boldsymbol{k}} \chi_{\boldsymbol{k}} + \chi_{-\boldsymbol{k}} \chi^\dagger_{-\boldsymbol{k}} \right) + \frac{gN}{V} \sum_{k\neq 0}{}' \left(\chi^\dagger_{\boldsymbol{k}} \chi^\dagger_{-\boldsymbol{k}} + \chi_{-\boldsymbol{k}} \chi_{\boldsymbol{k}} \right) \right) + \text{const.} \tag{3.9}$$

where $\sum'_{k\neq 0}$ indicates that the sum is only taken over one half of the momentum space. By performing the Bogoliubov transformation $\chi_{\boldsymbol{k}} = u\rho_{-\boldsymbol{k}} - v\rho^\dagger_{\boldsymbol{k}}$ and $\chi^\dagger_{-\boldsymbol{k}} = -v\rho_{-\boldsymbol{k}} + u\rho^\dagger_{\boldsymbol{k}}$, the excitation Hamiltonian is readily diagonalized as

$$H_{\text{ex}} = \sum_{\boldsymbol{k}} \varepsilon_{\boldsymbol{k}} \rho^\dagger_{\boldsymbol{k}} \rho_{\boldsymbol{k}} + \text{const.}, \tag{3.10}$$

where the dispersion of the Bogoliubov quasi-particle is

$$\varepsilon_k = \sqrt{\left(\frac{k^2}{2m} + \frac{gN}{V} \right)^2 - \frac{g^2N^2}{V^2}} = \frac{k}{\sqrt{2m}} \sqrt{\frac{k^2}{2m} + \frac{2gN}{V}}, \tag{3.11}$$

and $\rho_{\boldsymbol{k}}$ is the annihilation operator of a Bogoliubov quasi-particle, and the bosonic relation requires $u^2 - v^2 = 1$.

At low energies ($k \to 0$), the dispersion is linear: $\varepsilon_k = k\sqrt{gN/mV}$, where the finite slope defines a critical sound speed $v_c = \partial\varepsilon_k/\partial k|_{k=0} = \sqrt{gN/mV}$. Depending

on the forms of dispersion and interaction, the Bogoliubov spectrum could be non-monotonic. For instance, the spectrum might exhibit "maxon-roton" like structure as in a ^{4}He superfluid [24, 25]. I will show one such example in **chapter 7**.

3.4 Bogoliubov-de Gennes equation for degenerate Fermi gases

In this section, we study Eq. (3.1)-(3.2) for degenerate Fermi gases, where the Pauli principle only allows the $g_{\uparrow\downarrow}$ term. For spinless fermions, the $g_{\uparrow\downarrow}$ term is absent, and effective interactions only come from higher energies, such as p-wave and d-wave. For our spin-1/2 gases, where s-wave interactions dominate, the Hamiltonian is

$$H = \int d\mathbf{r} \left(\sum_{\sigma=\uparrow,\downarrow} \psi_\sigma^\dagger(\boldsymbol{r}) \left(-\frac{\boldsymbol{\nabla}^2}{2m} + V(\boldsymbol{r}) - \mu_\sigma \right) \psi_\sigma(\boldsymbol{r}) + g\, \psi_\uparrow^\dagger(\boldsymbol{r})\, \psi_\downarrow^\dagger(\boldsymbol{r})\, \psi_\downarrow(\boldsymbol{r})\, \psi_\uparrow(\boldsymbol{r}) \right), \quad (3.12)$$

where we have included an external potential $V(x)$ and a chemical potential μ. We assume the interaction is attractive: $g < 0$. Note μ_σ could be different for different spin, but here we only consider $\mu_\uparrow = \mu_\downarrow = \mu$.

Since the interaction term is quartic, Eq. (3.12) can not be solved in a closed form in generic dimensions. We here use the mean-field approximation to decouple the quartic term.

There are various ways to write Eq. (3.12) into a bilinear form, and each of these may describe a different phenomena. We here discuss the Bardeen-Cooper-Schrieffer (BCS) mean-field theory, which describes the superconductivity [26]. The mathematical formulation of BCS theory was developed by Bo-

goliubov [27], where the Hamiltonian is written as

$$H = \int d\mathbf{r} \left(\sum_{\sigma=\uparrow,\downarrow} \psi_\sigma^\dagger(\boldsymbol{r}) \left(-\frac{\boldsymbol{\nabla}^2}{2m} + V(\boldsymbol{r}) - \mu \right) \psi_\sigma(\boldsymbol{r}) + H_{\text{BCS}} \right), \tag{3.13}$$

and

$$H_{\text{BCS}} = \int d\boldsymbol{r} \left(\Delta^*(\boldsymbol{r}) \psi_\downarrow(\boldsymbol{r}) \psi_\uparrow(\boldsymbol{r}) + \Delta(\boldsymbol{r}) \psi_\uparrow^\dagger(\boldsymbol{r}) \psi_\downarrow^\dagger(\boldsymbol{r}) - \frac{|\Delta(\boldsymbol{r})|^2}{g} \right). \tag{3.14}$$

Here $\Delta(\boldsymbol{r}) = g \langle \psi_\downarrow(\boldsymbol{r}) \psi_\uparrow(\boldsymbol{r}) \rangle$ is the superconducting order parameter, where the expectation operator is defined by $\langle ... \rangle = \frac{\text{Tr}\left(e^{-\beta H} ...\right)}{\text{Tr}\left(e^{-\beta H}\right)}$, with $\beta = 1/T$ denoting the inverse temperature. The order parameter acts like an external field (mean-field) that binds together an electron and a hole into a Cooper pair.

One can represent Eq. (3.13) by a 2 by 2 matrix,

$$H = \int d\mathbf{r} \begin{pmatrix} \psi_\uparrow(\boldsymbol{r}) \\ \psi_\downarrow^\dagger(\boldsymbol{r}) \end{pmatrix}^\dagger \begin{pmatrix} -\frac{\boldsymbol{\nabla}^2}{2m} - \mu + V(\boldsymbol{r}) & \Delta(\boldsymbol{r}) \\ \Delta^*(\boldsymbol{r}) & \frac{\boldsymbol{\nabla}^2}{2m} + \mu - V(\boldsymbol{r}) \end{pmatrix} \begin{pmatrix} \psi_\uparrow(\boldsymbol{r}) \\ \psi_\downarrow^\dagger(\boldsymbol{r}) \end{pmatrix} + \text{const.}. \tag{3.15}$$

This Hamiltonian is readily diagonalized by performing the Bogoliubov-de Gennes (BdG) transformation

$$\begin{pmatrix} \psi_\uparrow(\boldsymbol{r}) \\ \psi_\downarrow^\dagger(\boldsymbol{r}) \end{pmatrix} = \sum_n \begin{pmatrix} u_n(\boldsymbol{r}) & -v_n^*(\boldsymbol{r}) \\ v_n(\boldsymbol{r}) & u_n^*(\boldsymbol{r}) \end{pmatrix} \begin{pmatrix} \xi_{\uparrow n} \\ \xi_{\downarrow n}^\dagger \end{pmatrix}, \tag{3.16}$$

where $\xi_{\sigma n}$ ($\xi_{\sigma n}^\dagger$) denotes the annihilation (creation) operator of Bogoliubov quasi-particle. The fermionic anticommutation relation requires the transformation is unitary: $\sum_n \left(u_n^*(\boldsymbol{r}) u_n(\boldsymbol{r}') + v_n^*(\boldsymbol{r}) v_n(\boldsymbol{r}') \right) = \delta(\boldsymbol{r} - \boldsymbol{r}')$. The diagonalized Hamiltonian is then expressed as

$$H = \sum_{\sigma n} \epsilon_n \left(\xi_{\uparrow n}^\dagger \xi_{\uparrow n} - \xi_{\downarrow n} \xi_{\downarrow n}^\dagger \right) + \text{const.}, \tag{3.17}$$

where ϵ_n is the energy of the Bogoliubov excitation. Note $\{\epsilon_n, -\epsilon_n\}$ always come in pairs due to the particle-hole symmetry in Eq. (3.15). I will show in **chapter**

8 that this symmetry is responsible for creating "Majorana fermions", exotic particles who are their own anti-particle. A more generalized BdG equations which include spin-orbit coupling will be discussed in **chapter 8**.

In terms of $u_n(\boldsymbol{r})$ and $v_n(\boldsymbol{r})$, the order parameter $\Delta(\boldsymbol{r})$ is written as

$$\Delta(\boldsymbol{r}) = g\left\langle\psi_\downarrow(\boldsymbol{r})\psi_\uparrow(\boldsymbol{r})\right\rangle = g\sum_n u_n^*(\boldsymbol{r})v_n(\boldsymbol{r})\left(1-2f(\epsilon_n)\right), \tag{3.18}$$

where $f(x) = \frac{1}{1+e^{\beta x}}$ is the Fermi function. This equation is called gap equation, which implicitly determines the solutions for $\Delta(\boldsymbol{r})$. It can be computed iteratively following the procedures: [**1**] make an initial guess on $\Delta(\boldsymbol{r})$; [**2**] diagonalize the BdG Hamiltonian (3.15); [**3**] use computed eigenvectors (u_n, v_n) to calculate $\Delta(\boldsymbol{r})$; [**4**] repeat [**2**] until convergence is reached. In many cases, a different initial guess might lead to a different order parameter. This often means the system has more than one steady states, and the energy of each state is a local minimum. An alternative way to calculate $\Delta(\boldsymbol{r})$ is minimizing the free energy, as has been discussed by Stefan Bauer in his PhD thesis [28].

Another important physical quantity is the number density

$$n(\boldsymbol{r}) = \left\langle\psi^\dagger(\boldsymbol{r})\psi(\boldsymbol{r})\right\rangle = \sum_n |u_n(\boldsymbol{r})|^2 f(\epsilon_n) + |v_n(\boldsymbol{r})|^2\left(1-f(\epsilon_n)\right), \tag{3.19}$$

which can be readily calculated once $\Delta(\boldsymbol{r})$ is obtained.

Imposing symmetries can simplify the calculations. For example, if the system is translational invariant, the BdG Hamiltonian becomes a set of decoupled 2 by 2 matrix in momentum space, and one can solve the gap equation analytically [28]. Some of other symmetries are discussed in **chapter 6**.

CHAPTER 4

TOPOLOGY OF ENERGY BANDS

For the past ten years, "topological" material has been showing its explosive existence in condensed matter, drawing extraordinary attentions from the physics community [29, 30]. All of these excitements largely stem from one experiment in early 80s – the quantum Hall effect [31], where the transverse conductance of a two dimensional material is quantized and exhibits sharp jumps in a strong magnetic field. While these jumps indicate phase transitions, the various insulating states have the same local symmetry, and thus can not be distinguished by Landau's symmetry breaking theory [32]. The concept of topological phases, was introduced to classify these states [33, 34], where certain fundamental physical properties are robust against the smooth changes of material parameters unless the system passes through a topological phase transition. In this context, the topology is only useful where the physical system has an energy band gap that separates the ground states from the excited states, and the topological phase transition occurs when the band gap closes. In this chapter, I will introduce the mathematical description of topological invariants in a periodic potential, and discuss examples of topological phases. For more details about this field, one can refer to the review articles by Hasan and Kane [35], and Qi and Zhang [36].

4.1 Topological invariant

The topology of a physical system can be characterized by the Berry's phase – a geometric phase accumulated during the adiabatic evolution of a quantum state along a closed path in a parameter space. The generic form of the Berry's phase

can be expressed as [37],

$$\gamma = \oint_C d\boldsymbol{R} \cdot \boldsymbol{A}(\boldsymbol{R}), \tag{4.1}$$

where the Berry's connection is defined as

$$\boldsymbol{A}(\boldsymbol{R}) = i \langle n(\boldsymbol{R}) | \nabla_{\boldsymbol{R}} | n(\boldsymbol{R}) \rangle . \tag{4.2}$$

Here $|n(\boldsymbol{R})\rangle$ is the instantaneous eigenstate of a Hamiltonian parameterized by a vector $\boldsymbol{R}$, and C denotes a closed path from $\boldsymbol{R}(t_i)$ to $\boldsymbol{R}(t_f)$ where $\boldsymbol{R}(t_i) = \boldsymbol{R}(t_f)$. The Berry's connection is gauge depend, as it shifts from $\boldsymbol{A}(\boldsymbol{R}) \rightarrow \boldsymbol{A}(\boldsymbol{R}) - \nabla_{\boldsymbol{R}}\Theta(\boldsymbol{R})$ under a gauge transformation $|n(\boldsymbol{R})\rangle \rightarrow e^{i\Theta(\boldsymbol{R})} |n(\boldsymbol{R})\rangle$, where $\Theta(\boldsymbol{R})$ is an arbitrary scaler function.

It's also useful to rewrite Eq. (4.1) in terms of a surface integral using Stokes' theorem,

$$\gamma = \int_S d\boldsymbol{S} \cdot \boldsymbol{\Omega}, \tag{4.3}$$

where the Berry's curvature is defined as

$$\boldsymbol{\Omega} = \nabla_{\boldsymbol{R}} \times \boldsymbol{A}(\boldsymbol{R}) = i\nabla_{\boldsymbol{R}} \times (\langle n(\boldsymbol{R}) | \nabla_{\boldsymbol{R}} | n(\boldsymbol{R}) \rangle) . \tag{4.4}$$

Here $\mathcal{S}$ is an arbitrary surface enclosed by path C. Since $\nabla_{\boldsymbol{R}} \times (\nabla_{\boldsymbol{R}}\Theta(\boldsymbol{R})) = 0$, the Berry curvature is gauge independent.

4.1.1 Berry's phase in Bloch bands

In a crystalline system, the parameter space of the Berry's phase can be characterized by the quasi-momentum on an energy band, where the Brillouin zone

is a natural closed path. Concretely, we consider the following single particle Hamiltonian,

$$H = -\frac{\boldsymbol{\nabla}^2}{2m} + V(\boldsymbol{r}), \tag{4.5}$$

where $V(\boldsymbol{r}) = V(\boldsymbol{r} + \boldsymbol{a})$ is a periodic potential, with $\boldsymbol{a}$ the Bravais lattice vector. The eigenstate of this Hamiltonian is a Bloch wavefunction,

$$\psi_{n\boldsymbol{q}}(\boldsymbol{r}) = e^{i\boldsymbol{q}\cdot\boldsymbol{r}} u_{n\boldsymbol{q}}(\boldsymbol{r}) \tag{4.6}$$

where $u_{n\boldsymbol{q}}(\boldsymbol{r}) = u_{n\boldsymbol{q}}(\boldsymbol{r} + \boldsymbol{a})$ is a periodic wavefunction in real space, n is the band index, and $\boldsymbol{q}$ is the quasi-momentum in the first Brillouin zone. Applying a unitary transformation, the Hamiltonian is written as

$$H(\boldsymbol{q}) = e^{-i\boldsymbol{q}\cdot\boldsymbol{r}} H e^{i\boldsymbol{q}\cdot\boldsymbol{r}} = \frac{(-i\boldsymbol{\nabla} + \boldsymbol{q})^2}{2m} + V(\boldsymbol{r}), \tag{4.7}$$

where the eigenstate becomes the periodic function $u_{n\boldsymbol{q}}(\boldsymbol{r})$. The boundary condition $u_{n\boldsymbol{q}}(\boldsymbol{r}) = u_{n\boldsymbol{q}}(\boldsymbol{r} + \boldsymbol{a})$ guarantees that all the eigenstates live in the same Hilbert space [37]. A closed path is realized when $\boldsymbol{q}$ sweeps the entire Brillouin zone, and the Berry's phase is written as

$$\gamma_n = \int_{\mathrm{BZ}} d\boldsymbol{q} \cdot \langle u_n(\boldsymbol{q}) |\, i\nabla_{\boldsymbol{q}}\, | u_n(\boldsymbol{q}) \rangle \,. \tag{4.8}$$

In the following sections, I will discuss two representations of Berry's phase in periodic potentials: the Zak phase and the Chern number, which are responsible for one dimensional and two dimensional systems. I will introduce concrete models to elucidate their physical meanings, some of which are also discussed in **chapter 8** and **chapter 10**.

4.2 Zak's phase

For one dimensional periodic system, one defines the Zak's phase,

$$\gamma_n^{\text{zak}} = \int_{-\pi/a}^{\pi/a} dq \, \langle u_n(q)| \, i\partial_q \, |u_n(q)\rangle \,, \tag{4.9}$$

where a is the lattice constant, and q is the one dimensional quasi-momentum. The Zak's phase is related to the charge polarization of a one dimensional crystal [38]. In practice, a closed form of Eq. (4.9) is not always accessible, and one shall calculate the Zak's phase numerically. However, it could be tricky to make $|u_n(q)\rangle$ a smooth function of q in numerical calculations. A useful alternative is to exponentiate the phase and rewrite the integral as a product,

$$\exp\left(i\gamma_n^{\text{zak}}\right) = \lim_{\delta q \to 0} \exp\left(- \sum_{-\pi/a}^{\pi/a} \langle u_n(q)| \, \partial_q \, |u_n(q)\rangle \, \delta q \right) \tag{4.10}$$

$$= \prod_{q=-\pi/a}^{\pi/a} \left(\lim_{\delta q \to 0} \langle u_n(q) | u_n(q - \delta q)\rangle \right). \tag{4.11}$$

This formula takes care of the sudden jump of $|u_n(q)\rangle$ where the derivative is not well defined. A similar formula which includes spins will be discussed in **chapter 8**. Note it's useless to define the Berry's curvature in one dimension.

In general γ_n^{zak} can choose any value from zero to 2π, but when certain symmetry (constrain) is imposed, it can be quantized or become "topological". Any perturbation that breaks the symmetry will also break the quantization constraint. In the following, I will discuss two simple lattice models to illustrate this phenomena.

4.2.1 Rice-Mele model

We first consider a one dimensional tight-binding Hamiltonian,

$$H = \sum_j \left(-\left(J a_j^\dagger b_j + J' a_j^\dagger b_{j+1} + h.c. \right) + \Delta \left(a_j^\dagger a_j - b_j^\dagger b_j \right) \right), \tag{4.12}$$

where each unit cell contains two sites A and B, characterized by creation (annihilation) operators $a_j^\dagger$ (a_j) and $b_j^\dagger$ (b_j). The intra-tunneling amplitude within a unit cell is J, and the inter-tunneling amplitude is J'. The energy offset between A and B sites is 2Δ. This model was originally introduced by Rice-Mele to describe diatomic polymers [39]. Recently, it was realized in a one dimensional optical lattice [40]. Note when $\Delta = 0$, the model reduces to the well known Su-Schrieffer-Heeger (SSH) model [41].

In momentum space, Eq. (4.12) is expressed as

$$\begin{aligned} H &= \sum_k \begin{pmatrix} a_k \\ b_k \end{pmatrix}^\dagger \begin{pmatrix} \Delta & -J - J' e^{-ikd} \\ -J - J' e^{ikd} & -\Delta \end{pmatrix} \begin{pmatrix} a_k \\ b_k \end{pmatrix} \qquad (4.13) \\ &= \sum_k \begin{pmatrix} a_k^\dagger & b_k^\dagger \end{pmatrix} \boldsymbol{h}(k) \cdot \boldsymbol{\sigma} \begin{pmatrix} a_k \\ b_k \end{pmatrix}, \qquad (4.14) \end{aligned}$$

where $a_k = \frac{1}{\sqrt{N}} \sum_j e^{ikdj} a_j$ and $b_k = \frac{1}{\sqrt{N}} \sum_j e^{ikdj} b_j$, with N the number of superlattice sites and d the periodicity, and $\boldsymbol{\sigma}$ represents three Pauli matrices, and $\boldsymbol{h}(k)$ represents the Bloch vector, with $h_x = -J - J' \cos kd$, $h_y = -J' \sin kd$, and $h_z = \Delta$,

This Hamiltonian is readily diagonalized, with two eigenstates

$$\left| u_k^- \right\rangle = e^{-i\alpha/2} \begin{pmatrix} -\sin\frac{\beta}{2} e^{-i\alpha/2} \\ \cos\frac{\beta}{2} e^{i\alpha/2} \end{pmatrix}, \quad \left| u_k^+ \right\rangle = e^{-i\alpha/2} \begin{pmatrix} \cos\frac{\beta}{2} e^{-i\alpha/2} \\ \sin\frac{\beta}{2} e^{i\alpha/2} \end{pmatrix}, \tag{4.15}$$

where $\tan\alpha = h_y/h_x$ and $\tan\beta = \sqrt{h_x^2 + h_y^2}/h_z$, and the phase factor $e^{-i\alpha/2}$ is imposed to make $\left| u_k^\pm \right\rangle$ change smoothly along the closed path $-\pi/d < k \leq \pi/d$. One

can then write the Zak's phase

$$\gamma_{\pm}^{\text{zak}} = \int_{-\pi/d}^{\pi/d} dk \left\langle u_k^{\pm} \right| i\partial_k \left| u_k^{\pm} \right\rangle \tag{4.16}$$

$$= \int_{-\pi/d}^{\pi/d} dk \, \frac{1 \pm \cos\beta}{2} \partial_k \alpha \tag{4.17}$$

$$= \frac{1}{2} \int_{-\pi/d}^{\pi/d} dk \, \partial_k \alpha \pm \frac{1}{2} \int_{-\pi/d}^{\pi/d} dk \cos\beta \, \partial_k \alpha. \tag{4.18}$$

Depending on β, the Zak's phase $\gamma_{\pm}^{\text{zak}}$ can choose any value from zero to 2π, so the Hamiltonian is not topological. However, if we impose a sublattice symmetry between A and B sites by setting $\Delta = 0$, the second term in Eq. (4.18) vanishes, yielding

$$\gamma_{\pm}^{\text{zak}} = \frac{1}{2} \int_{-\pi/d}^{\pi/d} dk \, \partial_k \alpha = \begin{cases} \pi & J < J' \\ 0 & J > J'. \end{cases} \tag{4.19}$$

We see $\gamma_{\pm}^{\text{zak}}$ is now quantized – the value of $\gamma_{\pm}^{\text{zak}}$ only depends on the sign of $J - J'$ rather than the magnitude, and the topological transition happens at $J = J'$. Since the model only has two topologically distinct phases, it is a Z_2 topological material, protected by inversion (sublattice) symmetry.

4.2.2 Kitaev's chain

We now move to another example that also has a Z_2 topological index. We consider a one dimensional spinless Fermi gas on a lattice with p-wave superconducting pairing,

$$H = \sum_j \left(-t \left(c_j^\dagger c_{j+1} + h.c. \right) - \mu \, c_j^\dagger c_j + \Delta \left(c_j c_{j+1} + h.c. \right) \right), \tag{4.20}$$

where $c_j^\dagger$ (c_j) is the creation (annihilation) operator at lattice site j, and t is the tunneling amplitude between neighboring sites, μ is the chemical potential, and

Δ is the superconducting order parameter. This model was introduced by Kitaev to describe Majorana fermions in condensed matter system [42].

Similar to the previous analysis, we write Eq. (4.20) in momentum space,

$$H = \sum_{k>0} \begin{pmatrix} c_k \\ c_{-k}^\dagger \end{pmatrix}^\dagger \begin{pmatrix} -2t\cos kd - \mu & -2i\Delta \sin kd \\ 2i\Delta \sin kd & 2t\cos kd + \mu \end{pmatrix} \begin{pmatrix} c_k \\ c_{-k}^\dagger \end{pmatrix} + \text{const.} \quad (4.21)$$

$$= \sum_{k>0} \left(c_k^\dagger, c_{-k}\right) \boldsymbol{h}(k) \cdot \boldsymbol{\sigma} \begin{pmatrix} c_k \\ c_{-k}^\dagger \end{pmatrix} + \text{const.}, \quad (4.22)$$

where $c_k = \frac{1}{\sqrt{N}} \sum_j e^{ikdj} c_j$, and $h_x(k) = 0$, $h_y(k) = 2\Delta \sin kd$, and $h_z(k) = -2t\cos kd - \mu$, and d is the lattice constant. Here we see the Bloch vector $\boldsymbol{h}(k)$ only lives on the $y-z$ plane, and thus the Zak's phase is always quantized. This is guaranteed by the particle-hole symmetry. The symmetry holds even when the superconducting pairing is s-wave, where the Zak's phase is always zero (topologically trivial).

4.3 Chern number

In two dimensions, the Bloch eigenstates $|u(\boldsymbol{k})\rangle$ are parameterized by a two dimensional quasi-momentum $\boldsymbol{k}$. Periodicity of the quasi-momentum implies that the Brillouin zone is a torus, allowing us to define a Chern number [37],

$$C = \frac{1}{2\pi} \int_{\text{BZ}} dk_x dk_y \, \Omega_{k_x k_y}. \quad (4.23)$$

where k_x and k_y denote two quasi-momentum in the x-direction and y-direction, and the Berry's curvature is

$$\Omega_{k_x k_y} = i\left(\partial_{k_y} \left\langle u(\boldsymbol{k}) \middle| \partial_{k_x} \middle| u(\boldsymbol{k}) \right\rangle - h.c.\right). \quad (4.24)$$

In most cases, it is difficult to calculate Eq. (4.23) analytically. A useful trick is to numerically calculate the Berry's phase on a small plaquette using Eq. (4.10), and sum up all the plaquettes. In particular,

$$C = \frac{1}{2\pi} \lim_{\delta k_x \to 0} \lim_{\delta k_y \to 0} \sum_{k_x, k_y} \gamma_{k_x k_y}, \tag{4.25}$$

where

$$\begin{aligned} \exp\left(i\gamma_{k_x k_y}\right) &= \langle u(\boldsymbol{k}) | u(\boldsymbol{k} + \delta k_x) \rangle \left\langle u(\boldsymbol{k} + \delta k_x) | u(\boldsymbol{k} + \delta k_x + \delta k_y) \right\rangle \\ &\times \left\langle u(\boldsymbol{k} + \delta k_x + \delta k_y) | u(\boldsymbol{k} + \delta k_y) \right\rangle \left\langle u(\boldsymbol{k} + \delta k_y) | u(\boldsymbol{k}) \right\rangle. \end{aligned} \tag{4.26}$$

The Chern number is an integer, labelled by the set of integer Z. Depending on other physically relevant symmetries, such as time-reversal symmetry (TRS) or particle-hole symmetry (PHS), the bands can be classified by other sets such as Z_2 (0,1) or 2Z (even number) [43]. For example, a two dimensional spin-hall insulator (with TRS) belongs to a Z_2 class, while an integer quantum hall insulator or a (chiral) *p*-wave superconductor (broken TRS) belongs to a Z class [43]. The classification of topological invariant in generic dimensions has been comprehensively studied in Ref. [44].

While the Chern number is a property of a gapped bulk, it also specifies the number of edge states on the material [35]. For example, a spinless $p + ip$ superconductor ($C = 1$) can only have one Majorana edge mode at a topological boundary, while a chiral triplet superconductor ($C = 2$) can have two Majorana edge modes.

In the following section, I will study a two dimensional example where the Chern number can choose any integer. I will show explicitly the Chern number is equal to the number of topologically protected edge states.

The following section is largely adapted from an unpublished paper "The anisotropic

Harper-Hofstadter model: spectra, Chern number and edge states" by Ran Wei and Erich J. Mueller.

4.4 Anisotropic Harper-Hofstadter Model

We consider a model of non-interacting particles on a two dimensional array of N coupled wires in a magnetic field,

$$H = \sum_{j=1}^{N} \int dx \left(\psi_j^\dagger(x) \left(-\frac{1}{2m} \partial_x^2 + V_j(x) \right) \psi_j(x) - \left(t\, e^{ipx} \psi_{j+1}^\dagger(x)\, \psi_j(x) + h.c. \right) \right), \quad (4.27)$$

where $\psi_j^\dagger(x)$ ($\psi_j(x)$) creates (annihilates) a particle on the jth wire, and t is the nearest neighboring tunneling amplitude between wires. The magnetic field $B = pc/de$ leads to a complex phase on the tunneling matrix element, where d is the wire spacing, c is the speed of light and e is the electron charge. We consider the case where p/q is a rational number, corresponding to a commensurate magnetic flux per unit cell. We take the potential along each wire to be $V_j(x) = 2v\cos(qx + \phi_j(x))$, with v and ϕ_j the intensity and the phase of the potential. For most of this section we will take $\phi_j(x) = \phi_0$ to be the same on each wire. This is the simplest case to implement experimentally. The ability to choose other phase profiles, however, is very powerful. For example, one can introduce dislocations through $\phi_j(x)$. Strategies for creating such profiles can be found in [45].

Imposing periodic boundary conditions along x, we write the Hamiltonian in the k_x-space,

$$H = \sum_{j=1}^{N} \sum_{k_x=-\infty}^{\infty} \left(\frac{k_x^2}{2m} \psi_{j,k_x}^\dagger \psi_{j,k_x} + \left(v\, e^{i\phi_0} \psi_{j,k_x}^\dagger \psi_{j,k_x+q} - t\, \psi_{j+1,k_x}^\dagger \psi_{j,k_x+p} + h.c. \right) \right), \quad (4.28)$$

where $\psi_{j,k_x} = \frac{1}{\sqrt{L}} \int dx\, e^{ik_x x} \psi_j(x)$, with L the length of the wire. The first term describes the parabolic energy-momentum dispersion of free particles, and the second term describes the potential-induced intra-wire scattering between the particles of momenta k_x and $k_x + q$, as illustrated in Fig. 4.1(a). The third term describes the tunneling induced inter-wire scattering between the particles of momenta k_x and $k_x + p$, as illustrated in Fig. 4.1(b). Note the momentum units in these figures are different.

Since p and q are commensurate, the Hamiltonian is periodic in the x-direction with period set by the greatest common divisor $\kappa \equiv \gcd(p, q)$. In k_x space, this real-space periodicity implies that states with momentum k_x are coupled only to those of momentum $k_x + n\kappa$ for integer n. Assuming the system is also periodic in the y-direction, we rewrite the Hamiltonian as (in the unit of κ^2/m)

$$H = \sum_{k_y=0}^{2\pi} \sum_{k_x=0}^{1} \sum_{n=-\infty}^{\infty} \frac{(k_x+n)^2}{2} \psi_n^\dagger \psi_n + \left(v\, e^{i\phi_0} \psi_n^\dagger \psi_{n+q} - t\, e^{-ik_y} \psi_n^\dagger \psi_{n+p} + h.c. \right), \tag{4.29}$$

where we have defined the dimensionless variables: $H \to H/\left(\kappa^2/m\right)$, $t \to t/\left(\kappa^2/m\right)$, $v \to v/\left(\kappa^2/m\right)$, $k_x \to k_x/\kappa$, $k_y \to k_y d$, $q \to q/\kappa$, and $p \to p/\kappa$. The dimensionless field operator in momentum space is denoted as $\psi_n \equiv \frac{1}{\sqrt{N}} \sum_{j=1}^{N} e^{ik_y j} \psi_{j,(k_x+n)\kappa}$, where n labels the quasi-energy band index. In the special case $k_y = 0$, Eq. (4.29) becomes the same as the model in **chapter 10**.

4.4.1 Chern number

Following the procedure described in **chapter 10**, one can write an effective model for Eq. (4.29) in the limit of $t, v \ll 1$,

$$\mathcal{H}_{\text{eff}} = \begin{pmatrix} -\frac{1}{2}\delta k_x & \alpha\Delta e^{i\chi} \\ \alpha\Delta e^{-i\chi} & \frac{1}{2}\delta k_x \end{pmatrix} + \text{const.}, \tag{4.30}$$

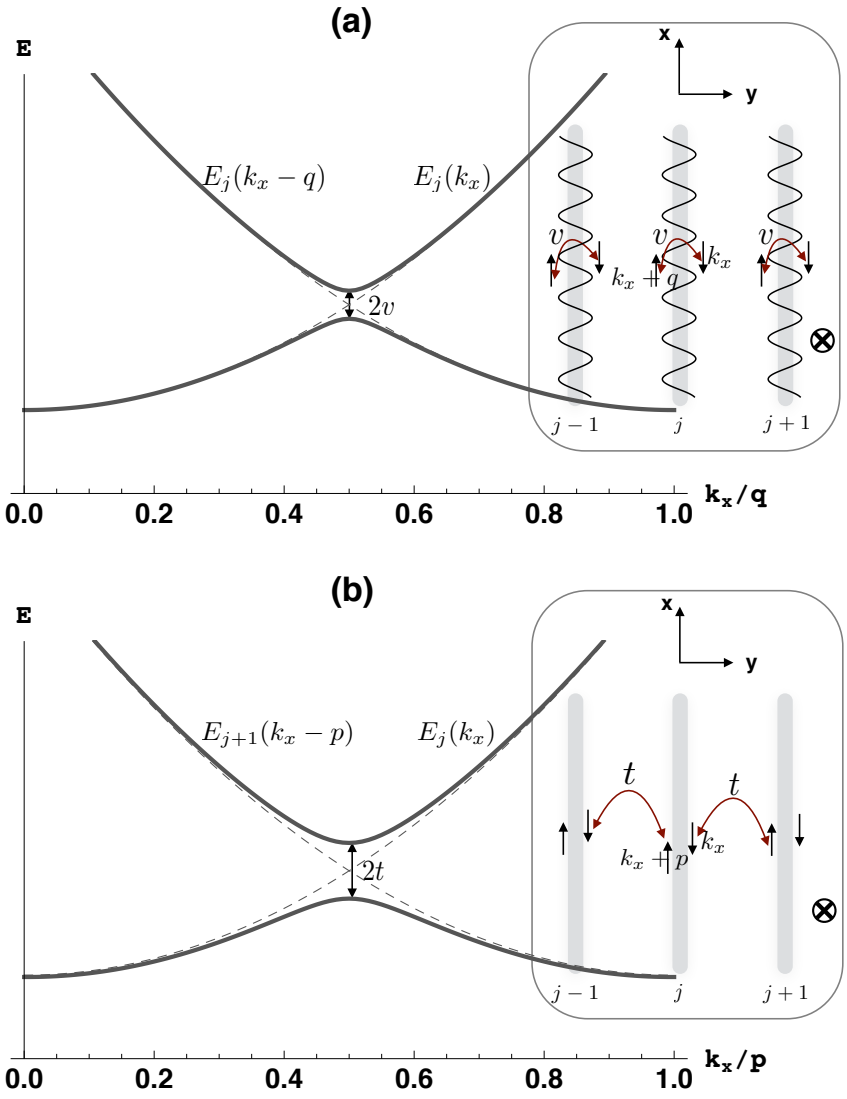

Figure 4.1: Single-particle spectra from Eq. (4.28). (a) Illustrates the case $t = 0$, corresponding to an array of uncoupled wires, with a periodic potential of wave-vector q along each of them. Dashed line corresponds to $v = 0$. (b) Illustrates the case $v = 0$, corresponding to coupled uniform wires in a constant magnetic field of strength $B = pc/de$, where d is the wire spacing, c is the speed of light and e is the electron charge. The tunneling strength is t. Dashed line corresponds to $t = 0$. Insets illustrate the scattering processes.

where $\delta k_x = k_x - 1/2$, $\Delta = v^{|r_m|}(-t)^{|s_m|}$, $\chi = -s_m k_y + r_m \phi_0$, and s_m, r_m correspond to the absolutely smallest solution to the Diophantine equation $sp + rq = 1$. The off-diagonal term splits the energy degeneracy at $k_x = 1/2$, and creates an energy

gap of size $2|\alpha\Delta|$.

Eq. (4.30) has the eigenstate,

$$|-\rangle = \begin{pmatrix} -\sin\frac{\beta}{2}e^{i\chi/2} \\ \cos\frac{\beta}{2}e^{-i\chi/2} \end{pmatrix}, \tag{4.31}$$

with $\tan\beta = -2\alpha\Delta/\delta k_x$. In the first Brillouin zone the states $|-\rangle$ form an energy band, and the topology of the band is characterized by a Chern number,

$$C = \frac{1}{2\pi}\int_{\mathrm{BZ}} \Omega_{k_x k_y} dk_x dk_y, \tag{4.32}$$

where the Berry curvature is

$$\Omega_{k_x k_y} = i\left(\partial_{k_y}\langle -|\partial_{k_x}|-\rangle - h.c.\right) = \frac{s_m}{2}\partial_{k_x}\cos\beta. \tag{4.33}$$

Integrating the Berry curvature yields the Chern number $C = s_m$, which is exactly equal to the solution to the Diophantine equation. As is well established [33], this Chern number corresponds to the transverse Hall conductance.

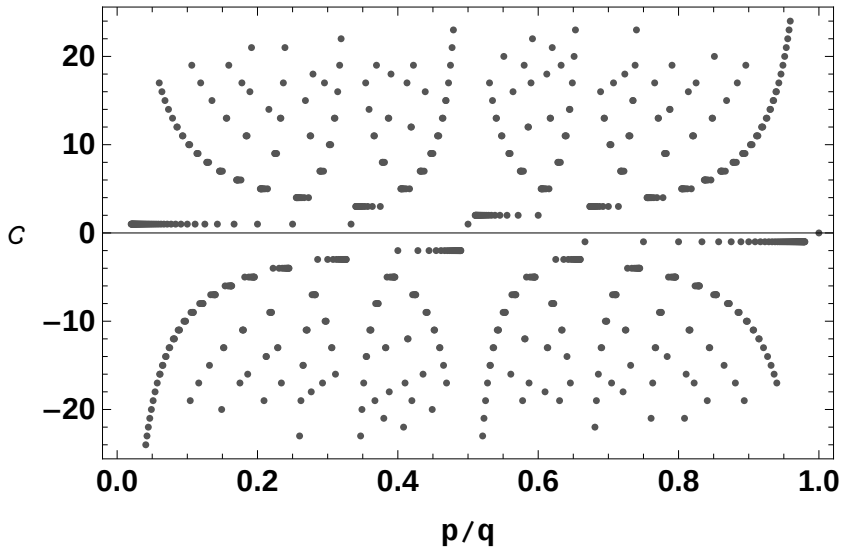

Figure 4.2: Chern number as a function of magnetic flux p/q for $1 \le p \le q \le 50$.

Fig. 4.2 shows C as a function of magnetic flux p/q for $1 \le p \le q \le 50$. We see the Chern number can be any integer ranging from $-q/2$ to $q/2$.

4.4.2 Topologically protected edge states

We here study Eq. (4.28) with an open boundary condition in the y-direction. Following the same procedure, we can construct the effective Hamiltonian,

(1) $s_m > 0$,

$$H_{\text{eff}} = \frac{\delta k_x}{2}\left(\sum_{j=1}^{s_m}\psi_{j,R}^{\dagger}\psi_{j,R} - \sum_{j=N-s_m+1}^{N}\psi_{j,L}^{\dagger}\psi_{j,L}\right) + \sum_{j=s_m+1}^{N}\left(\psi_{j-s_m,L}^{\dagger}, \psi_{j,R}^{\dagger}\right)\mathcal{H}_{\text{eff}}\begin{pmatrix}\psi_{j-s_m,L}\\ \psi_{j,R}\end{pmatrix}, \quad (4.34)$$

(2) $s_m < 0$,

$$H_{\text{eff}} = \frac{\delta k_x}{2}\left(\sum_{j=N+s_m+1}^{N}\psi_{j,R}^{\dagger}\psi_{j,R} - \sum_{j=1}^{-s_m}\psi_{j,L}^{\dagger}\psi_{j,L}\right) + \sum_{j=1}^{N+s_m}\left(\psi_{j-s_m,L}^{\dagger}, \psi_{j,R}^{\dagger}\right)\mathcal{H}_{\text{eff}}\begin{pmatrix}\psi_{j-s_m,L}\\ \psi_{j,R}\end{pmatrix}, \quad (4.35)$$

(3) $s_m = 0$,

$$H_{\text{eff}} = \sum_{j=1}^{N}\left(\psi_{j,L}^{\dagger}, \psi_{j,R}^{\dagger}\right)\mathcal{H}_{\text{eff}}\begin{pmatrix}\psi_{j,L}\\ \psi_{j,R}\end{pmatrix}, \quad (4.36)$$

where $\mathcal{H}_{\text{eff}}$ was defined in Eq. (4.29). Here we have defined the left mover $\psi_{j,L} \equiv \psi_{j,n=-1}|_{k_x\to 1/2}$ and the right mover $\psi_{j,R} \equiv \psi_{j,n=0}|_{k_x\to 1/2}$, and s_m is equal to the Chern number. The off-diagonal terms of $\mathcal{H}_{\text{eff}}$ couple the left movers and the right movers, so the bulk wires ($j = |s_m| + 1, ..., N - |s_m|$) are completely gapped. For $s_m > 0$, there are s_m left-moving edge modes on the wires $j = N - s_m + 1, ..., N$ and s_m right-moving edge modes on the wires $j = 1, ..., s_m$. For $s_m < 0$, there are $-s_m$ left-moving edge modes on the wires $j = 1, ..., -s_m$ and $-s_m$ right-moving edge modes on the wires $j = N + s_m + 1, ..., N$. For $s_m = 0$, the system is completely gapped, and there are no edge states. Including higher order terms or disorder will mix the states on one side of the sample, but since the modes are chiral, these coupling cannot open gaps. Exponentially small gaps can appear due to scattering between edge states on opposite sides of the sample.

4.4.3 Edge states induced by phase slips

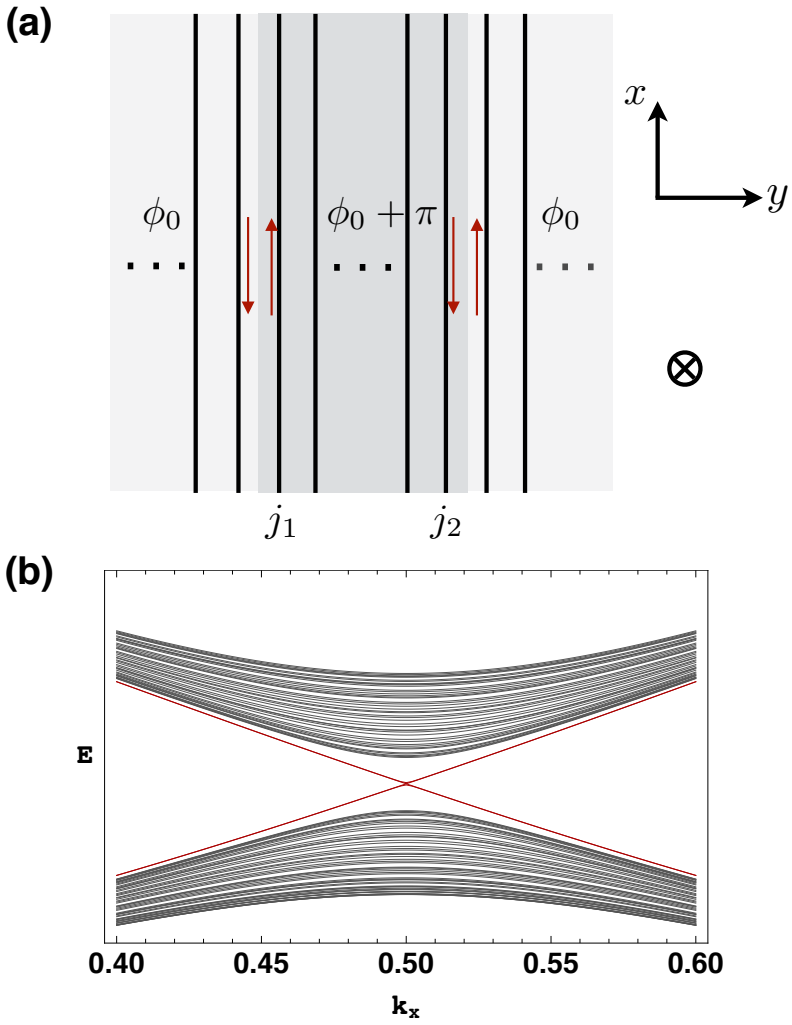

Figure 4.3: (a) Illustration of the coupled wires in a perpendicular magnetic field in the periodic potential $V_j(x) = 2v\cos(qx + \phi_j(x))$ with $\phi_j = \phi_0 + \pi\,(j_1 \leq j \leq j_2)$ and $\phi_j = \phi_0\,(j < j_1 \text{ or } j > j_2)$. At a particular strength of the magnetic field, the edge modes appear at the boundaries of the distinguished regions, as denoted by the red arrows. (b) Energy band structure for $p = 2$ and $q = 3$, where the gapless edge modes (denoted by the red lines) appear in the center of the bulk gap.

Finally we study the boundary of phase slip defects where the periodic potential is shifted on some wires. We find gapless edge states for particular strengths of the magnetic field. These edge states have no topological protec-

tion, and can be gapped out by disorder.

To be generic, we replace $\phi_0 \to \phi_j$ in Eq. (4.28). Using the similar procedure to derive an effective Hamiltonian on the basis of the left mover and the right mover, we obtain

$$\tilde{H}_{\text{eff}} = \sum_{j=1}^{N} \left(\psi^{\dagger}_{j-s_m,L}, \psi^{\dagger}_{j,R}\right) \tilde{\mathcal{H}}^{j}_{\text{eff}} \begin{pmatrix} \psi_{j-s_m,L} \\ \psi_{j,R} \end{pmatrix}, \tag{4.37}$$

where we have imposed the periodic boundary condition in the y-direction and defined $\psi_{-s_m} \equiv \psi_{N-s_m}$, and

$$\tilde{\mathcal{H}}^{j}_{\text{eff}} = \begin{pmatrix} -\frac{1}{2}\delta k_x & c_j\Delta \\ c_j^*\Delta & \frac{1}{2}\delta k_x \end{pmatrix} + \text{const.}, \tag{4.38}$$

where $c_j = \sum_{s=0}^{s=|s_m|} \alpha_s\, e^{i\phi_{j+s-1}}$, with α_s a real numerical pre-factor. Generally, the off-diagonal term of $\tilde{\mathcal{H}}^{j}_{\text{eff}}$ is nonzero, corresponding to an energy gap near $k_x \to 1/2$. However, we find for the special case where $p = 2, q = 3$, the effective Hamiltonian at $k_x = 1/2$ is

$$\tilde{\mathcal{H}}^{j}_{\text{eff}} = \frac{1}{3} \begin{pmatrix} -(v^2+t^2) & (e^{i\phi_{j-1}} + e^{i\phi_j})vt \\ (e^{-i\phi_{j-1}} + e^{-i\phi_j})vt & -(v^2+t^2) \end{pmatrix}. \tag{4.39}$$

At $\phi_{j-1} = \pi + \phi_j$, the Hamiltonian is diagonal, and the left mover and the right mover are not coupled, so there is a pair of gapless edge modes with the opposite current at the boundary between the regions with $\phi_j = \phi_0$ and $\phi_j = \phi_0 + \pi$.

To solidify our analytic argument, we numerically calculate the eigenvalues of the Hamiltonian in Eq. (4.28) for $\phi_0 \to \phi_j = \phi_0 + \pi\,(j_1 \le j \le j_2)$ and $\phi_0 \to \phi_j = \phi_0\,(j < j_1 \text{ or } j > j_2)$, and plot the energy bands as a function of k_x in Fig. 4.3(b). We see the bands cross at the center of the energy gap which correspond to the gapless edge modes. Note there are two boundaries of distinguished

regions, so there are two pairs of edge modes, as illustrated in Fig. 4.3(a). These edge modes have no topological protection, and can be gapped out by the local disorder near the boundary between distinguished regions.

CHAPTER 5

VORTEX STRUCTURES OF A TWO-COMPONENT BEC IN NARROW GEOMETRIES

This chapter was adapted from "Vortex structures of a two-component Bose-Einstein condensate for large anisotropies" by Ran Wei and Erich J. Mueller, published in Physical Review A 84, 063611 (2011).

5.1 Abstract

We calculate the vortex structures of an elongated two-component Bose-Einstein condensate. We study how these structures depend on the intra-component and inter-component interaction strengths. We present analytic and numeric results respectively at weak and strong interactions; finding lattices with different interlocking geometries: triangular, square, rectangular and double-core.

5.2 Introduction

One of the most exciting recent developments in cold atom experiments has been the production of artificial gauge fields, which couple to neutral atoms in the same way that magnetic fields couple to charged particles [1, 4]. While the greatest excitement surrounds the possibility of producing analogs of fractional quantum Hall states or topological insulators [46], these experiments also allow one to perform some extremely interesting experiments on vortices in Bose-Einstein condensates, similar to those performed on rotating gases [47, 48, 49, 50, 51, 52]. The resulting structures are particularly rich for multi-component

gases [53, 54, 55, 56]. As discussed below, although the current NIST experiments use roughly circular clouds, the technique naturally leads one to consider very narrow geometries. Here we theoretically investigate the vortex structures in a two-component Bose-Einstein condensate confined to a relatively narrow channel. We find a rich phase diagram which complements our understanding of the isotropic 2D system [53, 54, 55, 56].

In the NIST experiment the hyperfine states of ^{87}Rb are coupled by a series of Raman lasers. In the dressed state picture [1, 4], taking the strong Raman field limit, one arrives at an effective single particle Hamiltonian

$$H_1 = \frac{(p_x - A_x(y))^2}{2m} + \frac{p_y^2}{2m} + \frac{p_z^2}{2m} + V_{\text{eff}}(y, z). \tag{5.1}$$

The effective gauge field is bounded, $-\hbar k_R < A_x(y) < \hbar k_R$, where $\hbar k_R$ is the momentum kick from absorbing a photon from one beam and releasing it into another. One can generate arbitrarily large magnetic fields $B = -\partial_y A_x$, but due to the bounded nature of A_x, these can only exist over a finite extent in the y direction. It is therefore natural to choose the effective potential $V_{\text{eff}}(y, z)$ to restrict the particles to a small region of y, z, modeling it as $V_{\text{eff}}(y, z) = m\omega_y^{*2} y^2/2 + m\omega_z{}^2 z^2/2$. $V_{\text{eff}}(y, z)$ includes both the external potential and one induced by the Raman lasers.

In the NIST experiment, for large Raman Rabi frequency Ω, the only nonzero component of the vector potential is $A_x = -\hbar k_R \delta/\Omega$, where $\delta = \mu B_{\text{ext}}$ is the two-photon detuning, μ is the magnetic moment of the atom, and B_{ext} is the external magnetic field. To generate an artificial magnetic field, one applies a y-dependent B_{ext} so that the gradient $\delta' = d\delta/dy$ is nonzero. This technique unavoidably introduces an artificial scalar potential $V^* = -\hbar\delta^2/4\Omega$. For a constant δ', this yields an effective trapping frequency $\omega_y^* = \sqrt{\omega_y^2 - \hbar\delta'^2/2m\Omega}$.

The impact of the magnetic field on a single component Bose-Einstein condensate in such a narrow channel has been extensively studied [57, 58, 59]. As one increases the magnetic field from zero, the Bogoliubov spectrum starts to develop a "roton" minimum, whose energy falls with increasing B. When the roton energy hits zero, the system becomes unstable to undulations. At higher magnetic fields vortices enter the channel. Here we extend these results to the two-component gas.

The vortex structures in isotropic 2D two-component condensates are quite rich [53, 54]. Depending on the relative strength of the inter-component and intra-component scattering one can find interpenetrating lattices with different geometries: triangular, square, rectangular and double-core. Of these, triangular and square have been observed in experiments [60]. We find similar results in the anisotropic geometry.

A final motivation for thinking about the role of magnetic fields in very narrow geometries comes from solid state physics. In 2005, Seidel *et al.* [61] showed that the quantum Hall effect in narrow tori can be connected to charge density waves, with the fractionally charged vortices mapping onto fractionally charged domain walls. In this chapter we will focus on the Bose condensed regime, and will not be able to comment on this interesting physics. We do note, however, that our system undergoes a charge density wave instability before vortices enter the system. Investigating this instability in the low density "quantum" limit may be fruitful, even though the physics is likely to be very different from that in [61].

5.3 Model

There are four important lengths in Eq. (5.1), $d_z = \sqrt{\hbar/m\omega_z}, d_y = \sqrt{\hbar/m\omega_y^*}, \ell = \sqrt{\hbar/\bar{B}}$, and $R = \hbar k_R/\bar{B}$, where $\bar{B}$ is the peak value of B. These correspond to the trap length in the z and y direction, the magnetic length, and the spatial range over which the effective magnetic is nonzero. If d_z is sufficiently small, the kinetics becomes two dimensional. As we argue below, a sufficient condition will be $d_z \lesssim \ell$. If $d_y \ll R$, the gases will be confined to a region where the vector potential varies linearly and we can approximate: $A_x = -\bar{B}y$. In terms of the raw experimental parameters, $\bar{B} = \delta' \hbar k_R/\Omega$.

Taking $\Psi_1(\mathbf{r})$ and $\Psi_2(\mathbf{r})$ to annihilate atoms in the two (pseudo)-spin states, the short range interactions will be

$$H_{\text{int}} = \frac{1}{2}\int d\mathbf{r}\left(g_1\Psi_1^\dagger\Psi_1^\dagger\Psi_1\Psi_1 + g_2\Psi_2^\dagger\Psi_2^\dagger\Psi_2\Psi_2 + 2g_{12}\Psi_1^\dagger\Psi_2^\dagger\Psi_2\Psi_1\right). \tag{5.2}$$

The coupling constants are related to scattering lengths a_s via $g = 4\pi\hbar^2 a_s/m$. We will consider the case $g_1 = g_2 = g$, and $g_{12} = g_m$. For most experiments $g_1 \approx g_2 \approx g_{12}$, but one gains insight by relaxing this condition.

Following Sinha and Shlyapnikov [57], we diagonalize the single particle Hamiltonian in Eq. (5.1). The eigenstates are labeled by three quantum numbers K, n, n', with energies

$$E_{nn'}(K) = \mathcal{E}K^2 + n\hbar\omega_z + n'\hbar\tilde{\omega}_c. \tag{5.3}$$

where $\tilde{\omega}_c^2 = \omega_y^{*2} + \omega_c^2$, $\omega_c = \bar{B}/m$, and $\mathcal{E} = \hbar^2\omega_y^{*2}/4m\tilde{\omega}_c^2\tilde{\ell}^2$, $\tilde{\ell} = \sqrt{\hbar/m\tilde{\omega}_c}$, and we have neglected the zero-point energy. The continuous variable $K = \sqrt{2}\tilde{\ell}k$ is a dimensionless label of the momentum k along the x direction, while n and n' are discrete quantum numbers corresponding to the number of nodes in the z and

y directions. If the interaction energy per particle $\langle H_{\rm int}/N\rangle$ and the characteristic "kinetic energy" $\langle \mathcal{E}K^2\rangle$ are small compared to $\hbar\tilde{\omega}_c$ and $\hbar\omega_z$, one can truncate to the single particle eigenstates with $n = n' = 0$, which are of the form

$$\phi_K(x,y,z) = \frac{1}{\sqrt{\pi\tilde{\ell}d_z L}}\exp\left(i\frac{Kx}{\sqrt{2}\tilde{\ell}}\right)\exp\left(-\frac{(y-y_K)^2}{2\tilde{\ell}^2}\right)\exp\left(-\frac{z^2}{2d_z^2}\right) \tag{5.4}$$

where $y_K = \sqrt{2}\omega_c K\tilde{\ell}/2\tilde{\omega}_c$ and L is the length of x direction.

By taking the system sufficiently dilute, it is easy to arrange $\langle H_{\rm int}/N\rangle \ll \hbar\tilde{\omega}_c \sim \hbar\omega_z$. The other condition, $\mathcal{E}K^2 \ll \hbar\tilde{\omega}_c$, will be valid at strong magnetic fields. For our vortex lattices, we find the characteristic dimensionless wave-number to be $K \sim 1$, thus requiring $\omega_y^* \ll \omega_c$. Combining this with the previous constraint, $\omega_y^* \gg m\omega_c^2/\hbar k_R^2$, we see that our approximations break down unless the magnetic length is much larger than the wavelength of the Raman lasers, ie. $\omega_c \ll \hbar k_R^2/m$. This also establishes our requirement $d_z \lesssim \ell$.

Letting a_K annihilate the state in Eq. (5.4), the N-body Hamiltonian is

$$\begin{aligned}\frac{H}{\mathcal{E}} &= \sum_K K^2\left(a_{K\uparrow}^\dagger a_{K\uparrow} + a_{K\downarrow}^\dagger a_{K\downarrow}\right) + \frac{\beta}{N}\sum_q F_{\uparrow\uparrow}^\dagger(q)F_{\uparrow\uparrow}(q) \\ &+ \frac{\beta}{N}\sum_q F_{\downarrow\downarrow}^\dagger(q)F_{\downarrow\downarrow}(q) + \frac{2\beta_m}{N}\sum_q F_{\uparrow\downarrow}^\dagger(q)F_{\uparrow\downarrow}(q)\end{aligned} \tag{5.5}$$

where

$$F_{\sigma\tau}(q) = \sum_{K_1K_2}\delta_{q-K_1-K_2}e^{-\frac{1}{8}(K_1-K_2)^2}a_{K_1\sigma}a_{K_2\tau}, \tag{5.6}$$

and we have used $\uparrow,\downarrow$ in place of $1,2$. We take the continuum limit $\sum_K \to \left(\sqrt{2}L/4\pi\tilde{\ell}\right)\int dK$, and $\delta_K \to \left(2\sqrt{2}\pi\tilde{\ell}/L\right)\delta(K)$. The effective 1D parameters are $\beta = Nmg\tilde{\omega}_c^2\tilde{\ell}/\pi L d_z\omega_y^{*2}\hbar^2, \beta_m = \beta g_m/g$. From these definitions of the effective interaction parameters β,β_m, we see that increasing g, g_m has the same effect as increasing the magnetic field B, increasing the confinement ω_z, or reducing the confinement ω_y^*.

We consider a variational wavefunction corresponding to a Bose-Einstein condensate which is periodic in the x direction, with dimensionless wavelength $2\pi/K_0$, corresponding to a physical wavelength $\lambda = 2\sqrt{2}\pi\tilde{\ell}/K_0$,

$$|\psi\rangle = \exp\left(-\frac{N}{2} + \sum_{\sigma} \sqrt{N_\sigma}\left(\sum_n C_{n\sigma} a^\dagger_{nK_0\,\sigma}\right)\right)|\text{vac}\rangle. \tag{5.7}$$

Here $\sigma = \uparrow, \downarrow$. N_σ is the number of particles in state σ, and $N = N_\uparrow + N_\downarrow$. The coefficients $C_{n\sigma}$ are normalized to $\sum_n |C_{n\sigma}|^2 = 1$. In place of such a coherent state ansatz, some authors prefer to work with a "Fock" state

$$|\psi\rangle_F = \frac{1}{\sqrt{N_\uparrow! N_\downarrow!}}\left(\sum_n C_{n\uparrow} a^\dagger_{nK_0\uparrow}\right)^{N_\uparrow}\left(\sum_n C_{n\downarrow} a^\dagger_{nK_0\downarrow}\right)^{N_\downarrow}|\text{vac}\rangle. \tag{5.8}$$

For the quantities we are interested in, $|\psi\rangle$ and $|\psi\rangle_F$ are equivalent, and the variational parameters $C_{n\sigma}$ have the same meaning in each case: $|C_{n\sigma}|^2$ is the fraction of spin σ particles with momentum nK_0.

We take $N_\uparrow = N_\downarrow$, and further restrict ourselves to considering symmetric or antisymmetric wavefunctions: $C_{n,\sigma} = \pm C_{-n,\sigma}$. We classify our state by the value of K_0, and the number of non-zero C_n's which are needed to minimize the energy, ξ. For example, as illustrated in Fig. 5.1, for $(\beta, \beta_m) \sim (3, 1)$, we need only one n for each component: $n = 0$. We refer to this state as $(\xi_\uparrow, \xi_\downarrow) = (1, 1)$. This should be contrasted with the case at $(\beta, \beta_m) \sim (5, 2.5)$, where the energy is minimized by taking $n = -1, 0, 1$ in both components, a state we label as $(\xi_\uparrow, \xi_\downarrow) = (3, 3)$. Analytic expressions for the energies with small numbers of components are given in **Appendix 5.7.1**.

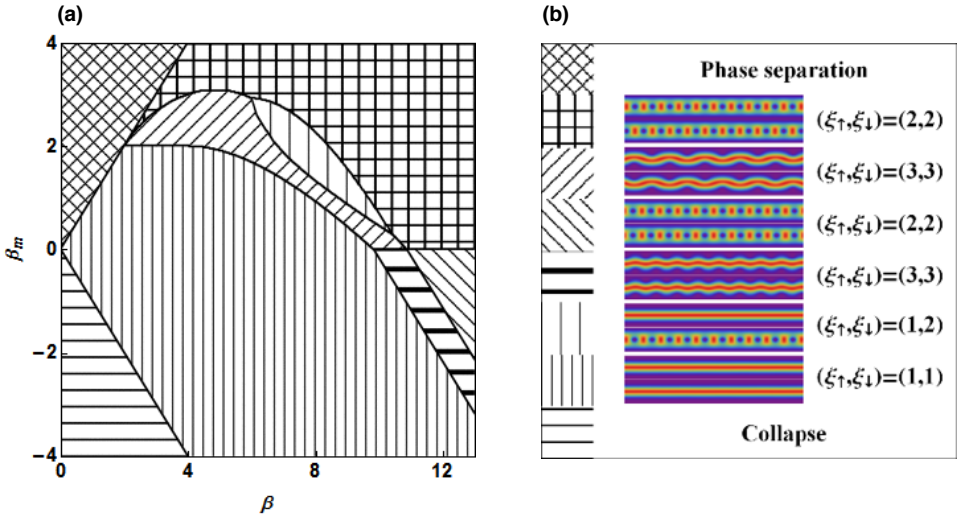

Figure 5.1: Top panel: phase diagram at small dimensionless intra-species and inter-species interactions β, β_m. Larger β, β_m corresponds to larger g, g_m, larger magnetic field, larger confinement ω_z, or weaker confinement ω_y^*. Hatched patterns represent states described by different number of Fourier components in each spin state: $(\xi_\uparrow, \xi_\downarrow)$. Bottom panel: the density profiles of the two-component wavefunction in the corresponding regimes. A color key for the density patterns is shown in Fig. 5.1.

5.4 Results at small β, β_m

The number of expansion parameters, $(\xi_\uparrow, \xi_\downarrow)$, grow with the magnitude of β, β_m. For small β and β_m, we only need a small number of terms in our wavefunctions, and we may use the analytic expressions in Eq. (5.9)-(5.23) to find the lowest energy state. We obtain a series of phase, as demonstrated in Fig. 5.1(a).

At $\beta_m = 0$, the $\uparrow$ and $\downarrow$ atoms decouple, and the physics is identical to the single component case, $\xi_\uparrow = \xi_\downarrow = \xi$. When $\beta < 9.8$, the ground state wavefunction has only one term ($\xi = 1$), which displays a Gaussian shape along y direction. As β increases past $\beta = 9.8$, the $\xi = 1$ wavefunction becomes unstable, and it undergoes a second-order phase transition to a density wave with $\xi = 3$. As β increases to $\beta = 10.8$, a first-order phase transition occurs to a state with $\xi = 2$,

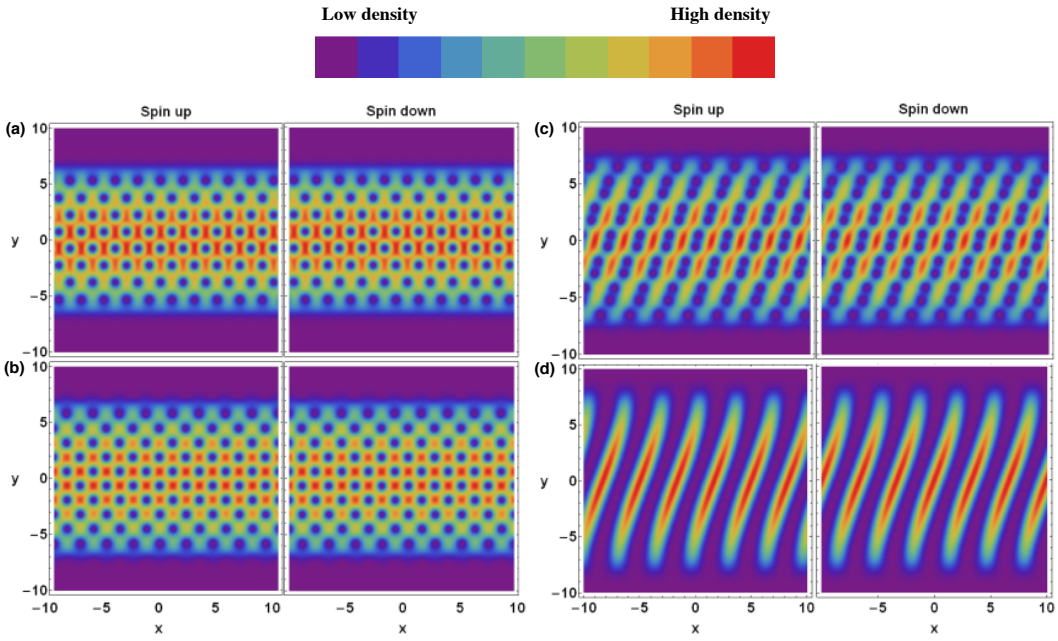

Figure 5.2: The density profiles of two-component BEC at large β, β_m, where x, y are in the unit of $\sqrt{2}\tilde{\ell}$. For (a)-(d), the parameters are $\beta_m/\beta = 0.1, 0.5, 1, 1.5$ respectively, with $\beta = 1000$. A color key is shown at the top.

characterized by a single row of vortices. These results have been extensively studied in Ref. [59].

In the regime of repulsive inter-component interaction ($\beta_m > 0$), the $\uparrow$ and $\downarrow$ particles try to avoid each-other. For strong repulsive interaction ($\beta_m > \beta$), the two components undergoes a microscale phase separate [62], which needs large (presumably infinite) ξ to describe. For weak repulsive interaction ($\beta_m < \beta$) rich structures, illustrated in Fig. 5.1 develop. For some β, β_m, we find $\xi_\uparrow \neq \xi_\downarrow$. For example, at $(\beta, \beta_m) = (8, 2)$, $\xi_\uparrow = 1$ and $\xi_\downarrow = 2$, and the $\downarrow$ atoms have a row of vortices, while the $\uparrow$ atoms show no structure. Under these circumstances there is a degenerate state with the $\uparrow$ and $\downarrow$ wavefunctions reversed. For other β, β_m, there is a symmetry between the two components with $\xi_\uparrow = \xi_\downarrow$. The vortices or density corrugations are displaced by half a period so that the density maxima

of the ↑ atoms line up with the density minima of the others. For example, when $(\beta, \beta_m) = (10, 3)$, each component displays a single row vortices, and the wavefunctions are related by a translation.

In the regime of attractive inter-component interaction ($\beta_m < 0$), one wants to maximize the overlap of the ↑ and ↓ wavefunctions. Generically, this means that the wavefunction of each component is identical, and the problem reduces to the single component case, but with a renormalized interaction $\beta \to \beta + \beta_m$. The phase diagram for $\beta_m < 0$ can be calculated from the phase diagram at $\beta_m = 0$ by mapping each point: $(\beta, \beta_m) \to (\beta - \beta_m, 0)$. For strong attractive interaction ($-\beta_m > \beta$), the BEC is unstable and expected to collapse, similar to the case of a single component BEC with attractive interaction [63].

5.5 Results at large β, β_m

For large β and β_m, the analytic expressions for the energy become unwieldy. We numerically minimize the expectation $\langle H \rangle$, varying $\{C_{n\sigma}, K_0\}$ in Eq. (5.7). The energy landscape has many local minima, and we use a range of starting parameters to try to find the absolute minimum. We cannot rule out the existence of even lower energy states. Moreover, for some parameters we found that the energy differences between competing minima became extremely small. In an experiment it is doubtful that one would find the true minimum energy state. Rather than systematically exploring the large β physics, we simply show a few examples.

Our results, illustrated in Fig. 5.2, are richer than those seen in the single component gas [59], showing structures similar to those in isotropic 2D studies

[53, 54]. When $\beta_m \ll \beta$ one finds two interlocking triangular lattices, as in Fig. 5.2(a) where $\beta_m/\beta = 0.1$. As one increases β_m the lattice structure changes: interlocking square lattices are shown in Fig. 5.2(b) where $\beta_m/\beta = 0.5$. When $\beta_m > \beta$ the non-rotating system would be expected to phase separate. Here, one finds more intricate vortex structures at $\beta_m \sim \beta$. At $\beta_m/\beta = 1$, we find double-core vortices (cf. [54]), as in Fig. 5.2(c). At $\beta_m/\beta = 1.5$ we find stripes, which are a microscopic version of phase separation. Close inspection of the image in Fig. 5.2(d), shows vortex cores in the low density regions. While these stripes are reminiscent of similar structures seen in the nonequilibrium dynamics of single component condensates [64], the physics is largely unconnected.

5.6 Summary and Conclusions

We have investigated the vortex structures in a two-component BEC with an artificial magnetic field, in an elongated geometry. Compared to the single component gas, the two-component vortex structures are more intricate.

To experimentally investigate these structures, one needs to find a system where the interspecies interactions can be tuned relative to the intraspecies. One promising approach is to use different atomic species for the two (pseudo)-spin states, and take advantage of an interspecies Feshbach resonance [65]. Some of the other newly condensed atomic systems may also be favorable [66, 67, 68, 69]. If one cannot separately tune β and β_m, one can still change the magnitude of them, fixing β_m/β. As seen in Fig. 5.1, such a cut through the phase diagram can still be quite rich, especially if $\beta_m/\beta \sim 0.25$.

There are several ways to extend the Raman scheme in [1] to produce an ar-

tificial magnetic field for a two-component gas. The conceptually simplest is to use two independent Raman lasers. Our results also apply to rotating clouds in anisotropic traps. As pointed out by Sinha and Shlyapnikov [57], when the rotation rate approaches the weakest trapping frequency the cloud becomes quite elongated.

5.7 Appendix

5.7.1 Analytic results for small number of components.

Here we give analytic results for the dimensionless energies of the states defined in Eq. (5.7), truncating the n-sums for each σ, and assuming symmetry/antisymmetry about the origin for each component.

State $(\xi_\uparrow, \xi_\downarrow) = (1, 1)$ is unique, and has energy

$$E_{1,1} = \frac{1}{2}(\beta + \beta_m) \tag{5.9}$$

State $(\xi_\uparrow, \xi_\downarrow) = (1, 2)$, with

$$\psi_\uparrow = \phi_{0\uparrow} \tag{5.10}$$

$$\psi_\downarrow = \frac{\sqrt{2}}{2}(\phi_{K_0\downarrow} + \phi_{-K_0\downarrow}) \tag{5.11}$$

is unique up to translation, and has energy

$$E_{1,2} = \frac{1}{2}K_0^2 + \frac{1}{4}\beta\left(e^{-K_0^2} + \frac{3}{2}\right) + \frac{1}{2}\beta_m e^{-\frac{1}{4}K_0^2} \tag{5.12}$$

State $(\xi_\uparrow, \xi_\downarrow) = (1, 3)$, with

$$\psi_\uparrow = \phi_{0\uparrow} \tag{5.13}$$

$$\psi_\downarrow \;=\; \sqrt{1-2|\varepsilon|^2}\phi_{0\downarrow} - \varepsilon(\phi_{K_0\downarrow} + \phi_{-K_0\downarrow}) \tag{5.14}$$

has energy

$$\begin{aligned} E_{1,3} &= \frac{1}{2}(\beta+\beta_m) + \left(K_0^2 + \beta\left(2e^{-\frac{1}{4}K_0^2} - e^{-\frac{1}{2}K_0^2} - 1\right) + \beta_m\left(e^{-\frac{1}{4}K_0^2} - 1\right)\right)\epsilon^2 \\ &+ \beta\left(e^{-K_0^2} + 2e^{-\frac{1}{2}K_0^2} - 4e^{-\frac{1}{4}K_0^2} + \frac{3}{2}\right)\epsilon^4 \end{aligned} \tag{5.15}$$

For state $(\xi_\uparrow, \xi_\downarrow) = (2,2)$, there are two distinct extremal states. Both components could be symmetric about the origin $\left(C_{1\uparrow} = C_{-1\uparrow} = C_{1\downarrow} = C_{-1\downarrow} = 1/\sqrt{2}\right)$, or one of them could be antisymmetric $\left(C_{1\uparrow} = C_{-1\uparrow} = C_{1\downarrow} = -C_{-1\downarrow} = 1/\sqrt{2}\right)$. This gives energies

$$E^s_{2,2} \;=\; K_0^2 + \frac{1}{4}(\beta+\beta_m) + \frac{1}{2}(\beta+\beta_m)e^{-K_0^2} \tag{5.16}$$

$$E^a_{2,2} \;=\; E^s_{2,2} - \frac{1}{2}\beta_m e^{-K_0^2} \tag{5.17}$$

For state $(\xi_\uparrow, \xi_\downarrow) = (2,3)$, the $\uparrow$ component can be symmetric or antisymmetric, resulting in energies

$$\begin{aligned} E^s_{2,3} &= \frac{1}{2}K_0^2 + \frac{1}{4}\beta\left(e^{-K_0^2} + \frac{3}{2}\right) + \frac{1}{2}\beta_m e^{-\frac{1}{4}K_0^2} + \left(K_0^2 + \beta\left(2e^{-\frac{1}{4}K_0^2} - e^{-\frac{1}{2}K_0^2} - 1\right)\right)\epsilon^2 \\ &+ \frac{1}{2}\beta_m\left(1 - 2e^{-\frac{1}{4}K_0^2} + 2e^{-K_0^2}\right)\epsilon^2 + \beta\left(\frac{3}{2} - 4e^{-\frac{1}{4}K_0^2} + 2e^{-\frac{1}{2}K_0^2} + e^{-K_0^2}\right)\epsilon^4 \end{aligned} \tag{5.18}$$

$$E^a_{2,3} \;=\; E^s_{2,3} - \beta_m e^{-K_0^2}\epsilon^2 \tag{5.19}$$

For state $(\xi_\uparrow, \xi_\downarrow) = (3,3)$, the optimal wavefunction is

$$\psi_\uparrow = \sqrt{1-2|\epsilon|^2}\phi_{0\uparrow} + i\epsilon\,(\phi_{K_0\uparrow} + \phi_{-K_0\uparrow}) \tag{5.20}$$

$$\psi_\downarrow = \sqrt{1-2|\epsilon|^2}\phi_{0\downarrow} \pm i\epsilon\,(\phi_{K_0\downarrow} + \phi_{-K_0\downarrow}) \tag{5.21}$$

with ϵ real.

If $\beta > \beta_m > 0$, the negative sign has lower energy,

$$\begin{aligned} E^-_{3,3} &= \frac{1}{2}(\beta+\beta_m) + \left(2K_0^2 + \beta\left(-2e^{-\frac{1}{2}K_0^2} + 4e^{-\frac{1}{4}K_0^2} - 2\right)\right)\epsilon^2 + \beta_m\left(2e^{-\frac{1}{2}K_0^2} - 2\right)\epsilon^2 \\ &+ \beta\left(2e^{-K_0^2} + 4e^{-\frac{1}{2}K_0^2} - 8e^{-\frac{1}{4}K_0^2} + 3\right)\epsilon^4 + \beta_m\left(2e^{-K_0^2} - 4e^{-\frac{1}{2}K_0^2} + 3\right)\epsilon^4 \end{aligned} \tag{5.22}$$

If $\beta > 0, \beta_m < 0$, the positive sign has lower energy,

$$E^+_{3,3} = E^-_{3,3} + 4\beta_m\left(e^{-K_0^2/4} - e^{-K_0^2/2}\right)\left(\epsilon^2 + 2\epsilon^4\right) \tag{5.23}$$

CHAPTER 6

PAIR DENSITY WAVES AND VORTICES IN AN ELONGATED TWO-COMPONENT FERMI GAS

This chapter was adapted from "Pair density waves and vortices in an elongated spin-1/2 Fermi gas" by Ran Wei and Erich J. Mueller, published in Physical Review Letter 108, 245301 (2012).

6.1 Abstract

We study the vortex structures of a spin-1/2 Fermi gas experiencing a uniform effective magnetic field in an anisotropic trap that interpolates between quasi-one dimensional (1D) and quasi-two dimensional (2D). At a fixed chemical potential, reducing the anisotropy (or equivalently increasing the attractive interactions or increasing the magnetic field) leads to instabilities towards pair density waves, and vortex lattices. Reducing the chemical potential stabilizes the system. We calculate the phase diagram, and explore the density and pair density. The structures are similar to those predicted for superfluid Bose gases. We further calculate the paired fraction, showing how it depends on chemical potential and anisotropy.

6.2 Introduction

Quantized vortices play an essential role in understanding the behavior of type-II superconductors and superfluids such as ^{3}He. In cold gases, these vortices were the smoking gun for superfluidity [70]. Here we study how confinement

influences the vortex structures in a trapped gas of ultracold fermions. We use the microscopic Bogoliubov-de-Gennes (BdG) equations, and consider anisotropic traps that interpolate between quasi-one dimensional (1D) and quasi-two dimensional (2D).

The behavior of topological defects in confined geometries can be quite rich. A good example is rotating bosons in anisotropic traps [57], where one sees multiple transitions in the structure of vortex lattices as the parameters are changed. Most intriguing, in the quasi-1D limit one sees a "roton" spectrum which softens as the rotation rate increases, signaling an instability to form a snake-like density wave. With recent experimental developments [1], we expect these structures can soon be explored in Bose gases, and related studies will be undertaken in Fermi gases. In the Fermi gas, we find parallels to all of the predicted boson physics. The single particle instability which drives density waves in the Bose case becomes a collective instability for the fermions, and instead drives pair density waves [71]. For a range of parameters we even find that the order parameter has the form predicted by Larkin and Ovchinnikov [72] for a polarized gas.

In very different contexts, studies of vortices in confined geometries lead to a number of interesting and important results such as "non-Hermitian" quantum mechanical analogies [73, 74, 75], and the destruction of superconductivity via phase slips [76]. Generically, reducing the dimensionality enhances fluctuations, leading to novel effects.

Driven partially by increased computer power and partially by interest in the BCS-BEC crossover, a number of research groups have recently produced Bogoliubov-de-Gennes (BdG) or density functional calculations of single vor-

tices [82, 83, 84, 85, 86, 87, 88, 89, 90], and vortex lattices [91, 92, 93]. These have largely been 2D or three dimensional (3D) calculations, with translational symmetry along the magnetic field. The numerical challenges of these calculations come from the large basis set needed to describe the single particle states. By truncating to the lowest Landau level, one can greatly simplify the problem [94, 95, 96]. As we explain below this limit is experimentally relevant [97, 98, 12].

6.3 Model

We start from the Hamiltonian of a spin-1/2 Fermi gas, with equal number of particles on the spin-up and spin down states. The total number of particles is $N = \int d\boldsymbol{r} \left(\Psi_\uparrow^\dagger(\boldsymbol{r})\Psi_\uparrow(\boldsymbol{r}) + \Psi_\downarrow^\dagger(\boldsymbol{r})\Psi_\downarrow(\boldsymbol{r})\right)$ and chemical potential is $\tilde{\mu}$,

$$\mathcal{K} = \int d\boldsymbol{r} \left(\sum_{\sigma=\uparrow,\downarrow} \Psi_\sigma^\dagger(\boldsymbol{r}) H_0 \Psi_\sigma(\boldsymbol{r}) + H_{\text{int}} \right) - \tilde{\mu} N, \tag{6.1}$$

where the single particle Hamiltonian $H_0 = (p_x - By)^2/2m + p_y^2/2m + p_z^2/2m + V(\boldsymbol{r})$, describes a neutral atom of mass m and momentum $\boldsymbol{p}$ experiencing a uniform effective magnetic field B in the z direction (Landau gauge), where the harmonic trap is $V(\boldsymbol{r}) = m\left(\omega_y^2 y^2 + \omega_z^2 z^2\right)/2$, and the inter-component interaction $H_{\text{int}} = g\Psi_\uparrow^\dagger(\boldsymbol{r})\Psi_\downarrow^\dagger(\boldsymbol{r})\Psi_\downarrow(\boldsymbol{r})\Psi_\uparrow(\boldsymbol{r})$, is attractive. Here the coupling constant is $g = 4\pi\hbar^2 a_s/m < 0$ [79], with $a_s < 0$ the s-wave scattering length. We do not treat the case where $g > 0$, in which the physics is more involved [80]. The single particle Hamiltonian is readily engineered in cold atoms either by using two counter-propagating Raman beams with spatially dependent detuning [1] or rotating the gas in anisotropic traps where the rotation rate approaches the weakest trapping frequency [81]. When ω_z is large, this model can be tuned from quasi-1D to quasi-2D by changing ω_y.

6.3.1 Lowest Landau level

Following Sinha *et al.* [57], the single particle Hamiltonian is readily diagonalized, with eigenstates labeled by three quantum numbers K, n, n', and energies given by

$$E_{nn'}(K) = \mathcal{E}K^2 + n\hbar\omega_z + n'\hbar\tilde{\omega}_c, \tag{6.2}$$

where the effective cyclotron frequency is $\tilde{\omega}_c = \sqrt{\omega_y^2 + \omega_c^2}$, the cyclotron frequency is $\omega_c = B/m$, the characteristic energy of motion in the x direction is $\mathcal{E} = \hbar\omega_y^2/4\tilde{\omega}_c$, and we have neglected the zero-point energy. The dimensionless wave-number $K = \sqrt{2}\tilde{\ell}k$ labels the momentum k along the x direction, where the effective magnetic length is $\tilde{\ell} = \sqrt{\hbar/m\tilde{\omega}_c}$. The discrete quantum numbers n and n' corresponds to the number of nodes in the z and y directions. In the absence of confinement in the y direction, $\mathcal{E} \to 0$, and we recover degenerate Landau levels. Hence, we refer to n as the Landau level index. If the interaction energy per particle $\langle H_{\text{int}}/N\rangle$ and the characteristic "kinetic energy" $\left\langle \mathcal{E}K^2 \right\rangle$ are small compared to $\hbar\tilde{\omega}_c$ and $\hbar\omega_z$, one can truncate to the lowest eigenstates with $n = n' = 0$, which are of the form

$$\phi_K(\boldsymbol{r}) = \frac{1}{\sqrt{\pi\tilde{\ell}d_z L}} \exp\left(i\frac{Kx}{\sqrt{2}\tilde{\ell}}\right) \exp\left(-\frac{(y-y_K)^2}{2\tilde{\ell}^2}\right) \exp\left(-\frac{z^2}{2d_z^2}\right), \tag{6.3}$$

where $y_K = \sqrt{2}\omega_c K\tilde{\ell}/2\tilde{\omega}_c$, $d_z = \sqrt{\hbar/m\omega_z}$ and L is the length in the x direction.

The conditions allowing us to truncate to the lowest Landau level constrain the 3D density n_{3D} and magnetic field strength B. For example, the condition $\langle H_{\text{int}}/N\rangle \ll \hbar\tilde{\omega}_c \sim \hbar\omega_z$ requires $n_{3D} \ll \hbar\tilde{\omega}_c/|g| \sim \hbar\omega_z/|g|$. The other condition, $\mathcal{E}K^2 \ll \hbar\tilde{\omega}_c$, requires $B \gg m\omega_y$. While such fields are challenging to produce in cold atoms, they are not completely unreasonable. In a very recent experiment performed by I. Bloch's group [12], the density is $n_{3D} \sim 10^{13}\text{cm}^{-3}$, and the

cyclotron frequency is $\omega_c \sim 100$kHz. Since this experiment involves coupled "wires", it is natural to use them for quasi-1D studies. Note, the magnetic field is "staggered" in that experiment, while we consider the uniform case.

Letting a_K annihilate the state in Eq. (5.1), one has an effective 1D model,

$$\frac{H}{\mathcal{E}} = \sum_{K,\sigma} \left(K^2 - \mu\right) a^\dagger_{K\sigma} a_{K\sigma} + \beta \sum_q f^\dagger(q) f(q), \tag{6.4}$$

where $f(q) \equiv \sum_K e^{-1/8(2K-q)^2} a_{q-K\downarrow} a_{K\uparrow}$, the dimensionless chemical potential is $\mu = \tilde{\mu}/\mathcal{E}$ and the effective interaction parameter is $\beta = \frac{2mg}{\pi\hbar^2 L}\left(\frac{\omega_z}{\tilde{\omega}_c}\right)^{1/2}\left(\frac{\tilde{\omega}_c}{\omega_y}\right)^2$. From the definition of β, one sees that increasing the interaction strength g has the same effect as increasing the magnetic field B, increasing the z-confinement ω_z, or reducing the y-confinement ω_y. In the following, we will investigate the properties of the confined Fermi gas by studying Eq. (6.4). One can show that the interaction in Eq. (6.4) is equivalent to $\beta \sum_q f^\dagger(q) f(q) = \beta \int d\boldsymbol{r} F^\dagger(\boldsymbol{r}) F(\boldsymbol{r})$, where $F(\boldsymbol{r}) = \sum_q f(q)\phi_q(\boldsymbol{r})$.

6.3.2 Bogoliubov de Gennes approach

We introduce the pair field $\Delta_q = \beta\langle f(q)\rangle$, and its transform $\Delta(\boldsymbol{r}) = \beta\langle F(\boldsymbol{r})\rangle$. We neglect the fluctuation $\left(f^\dagger(q) - \Delta_q^*/\beta\right)\left(f(q) - \Delta_q/\beta\right)$ to reduce Eq. (6.4) to a bilinear form,

$$\frac{H}{\mathcal{E}} = \sum_{K,\sigma} \left(K^2 - \mu\right) a^\dagger_{K\sigma} a_{K\sigma} + \sum_q \left(\Delta_q^* f(q) + \Delta_q f^\dagger(q) - \frac{|\Delta_q|^2}{\beta}\right). \tag{6.5}$$

Given Δ_q, one can diagonalize H, and then impose self-consistency. For arbitrary Δ_q, this process is unwieldy [91, 92, 93]. We here introduce two approximations which make the numerical calculations more efficient. First, we assume Δ_q is non-vanishing only when the central momentum of the paired fermions is

$q = nK_0$, where $n = 0, \pm 1, \pm 2, ...$ The characteristic wave-number K_0 is taken to be a variational parameter. This is equivalent to assuming $\Delta(\boldsymbol{r})$ is periodic in the x direction and treating the wavelength variationally. Second, we restrict ourselves to consider the symmetric pair field: $\Delta_q = \Delta_{-q}$. This implies a spatially symmetric field $\Delta(\boldsymbol{r}) = \Delta(-\boldsymbol{r})$. Under these assumptions, the Hamiltonian is reduced to

$$\frac{H}{\mathcal{E}} = \sum_{K,\sigma} \left(K^2 - \mu\right) a^\dagger_{K\sigma} a_{K\sigma} - \frac{\sum_n |\Delta_{|n|K_0}|^2}{\beta} + \sum_n \left(\Delta^*_{|n|K_0} f(nK_0) + \Delta_{|n|K_0} f^\dagger(nK_0)\right). \quad (6.6)$$

Since Eq. (6.6) will be calculated by taking the continuum limit $\sum_K \to \sqrt{2}L/4\pi\tilde{\ell} \int dK$ (see **Appendix 6.9.1**), it is useful to introduce a positive parameter $\alpha = -\sqrt{2}L\beta/4\pi\tilde{\ell}$ to characterize the effective attractive interaction. For small α, we find $\Delta_{|n|K_0} \neq 0$ for only a few values of n. We define ξ to be the number of nonzero $\Delta_{|n|K_0}$. The various phases can be distinguished by looking at the pair density $\left|\langle \Psi_\uparrow \Psi_\downarrow \rangle\right|^2$ and/or the particle density $\left\langle \Psi^\dagger_\uparrow \Psi_\uparrow \right\rangle$ (see Fig. 6.1(b)). The features are clearest in the pair density. If more than one Δ_{nK_0} is nonzero, we have either a pair density wave or vortices. For example, the case $\xi = 3$ ($\Delta_0 \neq 0, \Delta_{\pm K_0} \neq 0$), as illustrated in Fig. 6.1(b), corresponds to a pair density wave where $\left|\langle \Psi_\uparrow \Psi_\downarrow \rangle\right|^2$ has corrugations. The case $\xi = 2$ ($\Delta_0 = 0, \Delta_{\pm K_0} \neq 0$), consists of a single row of vortices. Larger ξ, for example in Fig. 6.3, corresponds to a vortex lattice. The case $\xi = 2$ gives an order parameter which can formally be identified with the Larkin-Ovchinnikov (LO) state [72] (see also [77]). Here, Δ_K is nonzero except when $K = \pm K_0$. Defining an effective 1D order parameter $\Delta^{1D}(x) = \sum_K e^{iKx} \Delta_K$, we have $\Delta^{1D}(x) = 2\Delta_{K_0} \cos K_0 x$. Note that unlike the LO state, the physical order parameter $\Delta(\boldsymbol{r}) = \sum_K \Delta_K \phi_K(\boldsymbol{r})$, is not a simple cosine. Also note that unlike LO's model, here we assume both spin states have equal chemical potentials. Instead of being driven by the polarization, our instability towards a paired density wave is driven by the form of the effective 1D interaction.

When $\xi = 1$ ($\Delta_0 \neq 0$), Eq. (6.6) can be analyzed analytically (see **Appendix 6.9.1**). One readily obtains the gap equation,

$$\frac{1}{\alpha} = \int dK \frac{e^{-K^2}}{2\epsilon_K}, \tag{6.7}$$

and the number equation,

$$N = \frac{\sqrt{2}L}{4\pi\tilde{\ell}} \int dK \left(1 - \frac{\epsilon_0}{\epsilon_K}\right). \tag{6.8}$$

where $\epsilon_K = \sqrt{\epsilon_0^2 + |\Delta_0|^2 e^{-K^2}}$ and $\epsilon_0 = K^2 - \mu$.

Unlike the traditional case, the integrand in the RHS of Eq. (6.7) has a factor e^{-K^2} in the numerator, which dominates the behavior of the integrand for $K \gg 1$. If $\mu \gg 1$ (meaning in physics units $\tilde{\mu} \gg \mathcal{E}$), and Δ_0 is sufficiently small, the integrand in Eq. (6.7) is bimodal. There is a gentle peak of height $1/2\mu$ and width 1 centered at $K = 0$, and a sharp peak of height $e^{-\mu/2}/2|\Delta_0|$ and width $|\Delta_0|e^{-\mu/2}/\sqrt{\mu}$ centered at $K = \sqrt{\mu}$. The power-law tails of this sharp peak give a contribution to the integral which scales as $A\,(\log|\Delta_0|)\,e^{-\mu}/\sqrt{\mu}$ as $\Delta_0 \to 0$, where A is a constant. Solving Eq. (6.7) in this regime yields an extremely small order parameter. In this weak pairing limit, our numerics are unstable and the vortex lattices are better treated by expanding the energies in power of Δ_0 [78].

Another instructive limit is $\mu < 0$ and $N/L \to 0$, where the behavior is dominated by two-body physics. Eq. (6.7) then becomes the Schrödinger equation of a two-body problem in momentum space [99], i.e.,

$$\alpha = \frac{2}{\int dK \frac{e^{-K^2}}{K^2 - \mu}} \tag{6.9}$$

where the two-body binding energy ε is identified with twice the chemical potential, $\varepsilon = 2\mu(\alpha)$.

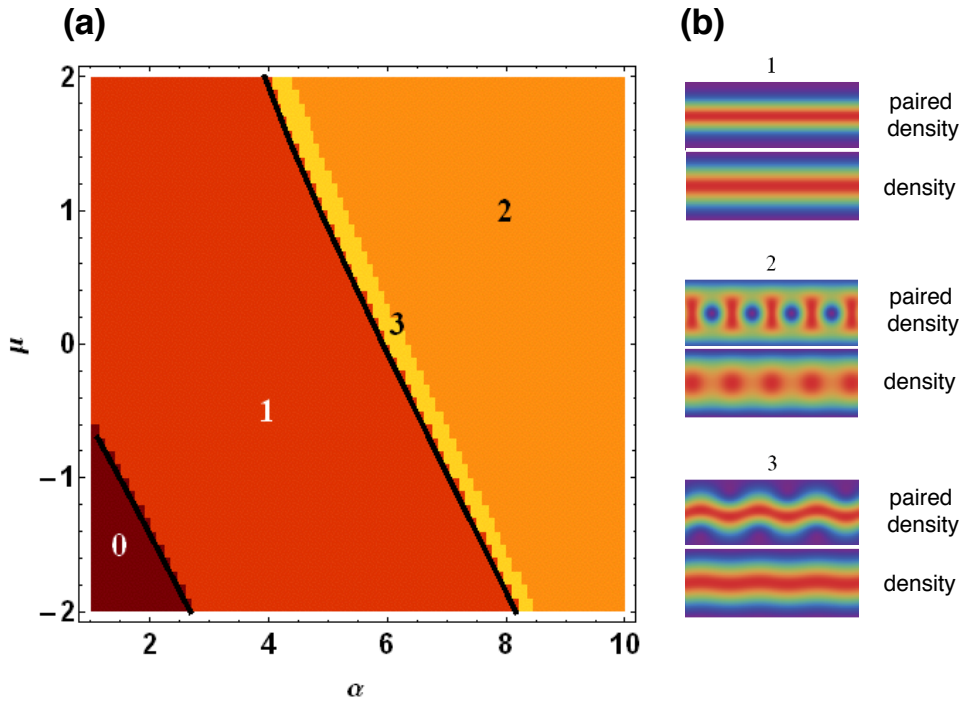

Figure 6.1: (a): The structure of phase diagram as a function of α and μ. The value of ξ (the number of nonzero $\Delta_{|n|K_0}$) is denoted in each region. The two black solid curves are the boundaries of two continuous transitions: $\xi = 0 \leftrightarrow \xi = 1$ and $\xi = 1 \leftrightarrow \xi = 3$. They show a fairly good agreement with numerics. (b): The structures of pair density $\left|\langle \Psi_\uparrow \Psi_\downarrow \rangle\right|^2$ and density $\left\langle \Psi_\uparrow^\dagger \Psi_\uparrow \right\rangle$ in the corresponding regions. The color key is shown in Fig. 6.3.

6.4 Phase diagram

We numerically minimize the energy by studying Eq. (6.6) (see **Appendix 6.9.2**). We find discrete jumps in ξ as a function of the dimensionless attractive interaction α and the dimensionless chemical potential μ. The resulting phase diagram is shown in Fig. 6.1(a). The darkest red region ($\xi = 0$) is the vacuum with no particles. Increasing α and/or μ brings one to a quasi-1D superfluid state. This state, characterized by $\xi = 1$, has no vortices and is translational invariant in the x direction. The $\xi = 0$ to $\xi = 1$ transition is continuous with $\Delta_0 \to 0$ and $N/L \to 0$ at the boundary. Further increasing α and/or μ leads to an instability towards a

$\xi = 3$ state (the narrow yellow region). This state breaks translational symmetry. The transition is continuous, and the boundary can be found via a linear stability analysis of the $\xi = 1$ state (see **Appendix 6.9.3**). At larger α and/or μ, there is a discontinuous transition to a state with $\xi = 2$. This sequence of instabilities closely mirrors what is found in calculations for Bose gases [57].

6.5 Pair fraction

It is useful to put these results in the context of the BCS-BEC crossover. In 3D Fermi gases one thinks of the superfluid with $\mu < 0$ as being formed from tightly bound bosonic pairs, analogous to ^{4}He. The superfluid with $\mu > 0$ is instead thought of within a BCS picture where diffuse pairs are formed by atoms at the Fermi surface. One can continuously tune between these two idealized limits by taking μ through zero: the size of the pairs varies continuously. Our approach to gaining insight into analogies with the 3D BCS-BEC crossover is to study the pair fraction $P = 2N_{\text{pair}}/N$ [100], as in Fig. 6.2. While some of the qualitative features of the 3D crossover persist in our effective 1D model, many of the details differ.

To understand this figure, one must note that in a quasi-1D system the ratio of the interaction to the kinetic energy is inverse proportional to the density, thus the strongly interacting regime can be reached by making the density small, or by making α large. The density increases monotonically with μ, but varies in a more complicated fashion with α. For small α and $\mu > 0$ we find $\partial N/\partial\alpha < 0$, while for large α and/or $\mu < 0$ we find $\partial N/\partial\alpha > 0$. At fixed α, the pair fraction decreases with μ (consistent with $\partial N/\partial\mu > 0$).

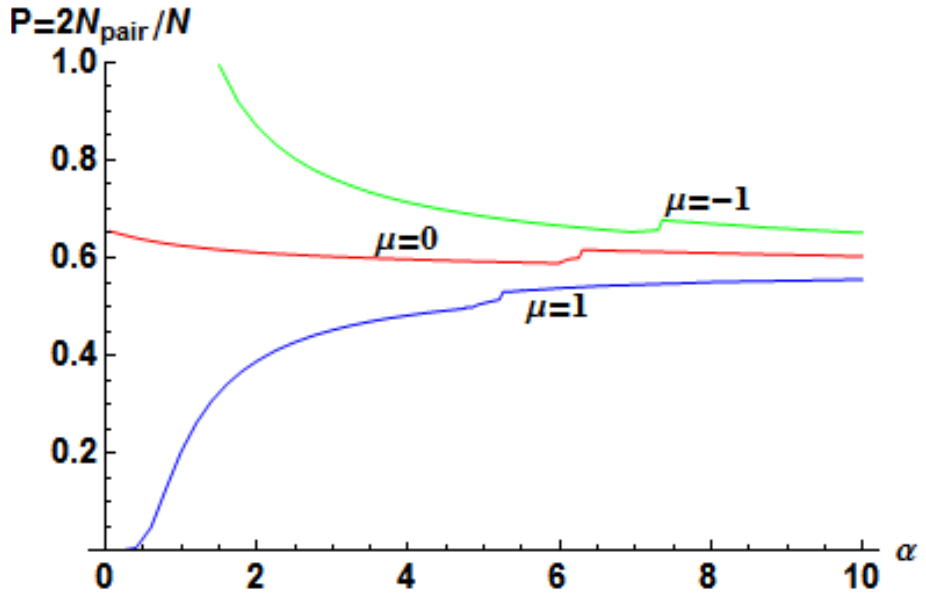

Figure 6.2: The pair fraction $P = 2N_{\text{pair}}/N$ versus α with $\mu = -1, 0, 1$. The exponential small P for $\mu = 1$ at $\alpha \to 0$ is reminiscent of the BCS limit, and the large value of P for $\mu = -1$ at $\alpha \approx 1.5$ is analogous to the BEC limit. The kink on each curve corresponds to the $\xi = 3 \leftrightarrow \xi = 2$ phase transition.

The top curve in Fig. 6.2, representing $\mu = -1$, starts at $P = 1$, roughly when $\alpha = 1.5$. Such a large value of P is reminiscent of the BEC limit. The density vanishes here, then grows as α increases. For $\mu = -1$, the pair fraction decreases with α, except for a small kink, corresponding to the first order $\xi = 3 \leftrightarrow \xi = 2$ phase transition.

On the contrary, for $\mu = 1$, P grows with α. As $\alpha \to 0$, P becomes exponentially small, as is predicted by the BCS theory. After a sharp rise, driven both by increasing α and decreasing N, the pair fraction levels out.

Each curve displays a kink, corresponding to the $\xi = 3 \leftrightarrow \xi = 2$ phase transition. As α increases to the region $\xi = 2$, one row of vortices enters the elongated superfluid. This transition is accompanied by density modulations.

To summarize we find that for $\mu > 0$ and small α the system behaves analogously to the BCS limit, while for $\mu < 0$ and $\alpha \sim |\mu|$ the system behaves more like the BEC limit. The density vanishes if $\mu < 0$ and $\alpha \lesssim |\mu|$. For most of our parameter range, we observe physics analogous to the crossover regime.

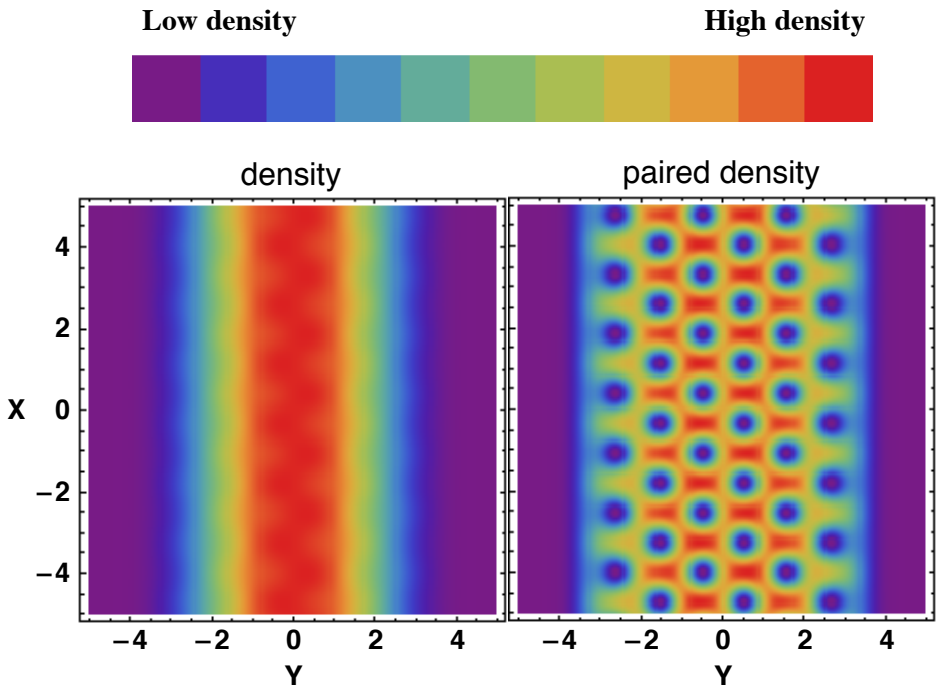

Figure 6.3: The profile of density (left panel) and pair density (right panel) at $\alpha = 65, \mu = 2$, where the dimensionless coordinates are $\mathrm{X} = x/\sqrt{2}\tilde{\ell}, \mathrm{Y} = y/\sqrt{2}\tilde{\ell}$. The color key is shown on the top.

6.6 Vortex lattice

With increasing α, the number of Fourier components ξ increases, and the width in the y direction grows. We illustrate the large α limit in Fig. 6.3 by calculating the density and the pair density of the state with $\mu = 2, \alpha = 65$ and $\xi = 7$. Only "faint" vortices are seen in the density (left panel). Unpaired fermions fill the vortex cores leading to very poor contrast. On the contrary, one sees a clear

stretched triangular lattice in the pair density (right panel). The lattice spacing is $\sim 2\pi\sqrt{2}\tilde{\ell}/K_0$ and the size of the vortex core is $\sim \tilde{\ell}$. Note the dimensionless wavenumber K_0 varies slightly with α but is of order 2. The vortex lattice is slightly deformed from a regular triangular lattice, but we expect this deformation to disappear in the quasi-2D limit ($\alpha \to \infty$).

6.7 Observation

Since the density depletion in the vortex core is highly suppressed, directly imaging the vortices through phase contrast or absorption imaging would be challenging. Coherent Bragg scattering of light may be a promising route for increasing the sensitivity of such optical probes [101]. One can also study the structures of pair density through photoassociation [102, 103], where the paired state is transformed to a bound molecular state after illuminated with light.

6.8 Summary

We have studied the spin-1/2 Fermi gases in elongated geometries. Truncating the BdG equations to the lowest Landau level, we investigate the vortex structures that emerge as the trap evolves from quasi-1D and quasi-2D. We calculate the phase diagram and find instabilities towards pair density waves and vortex lattices. We explore the structures of density and pair density, and calculate the pair fraction. We hope our results can soon be explored in experiment.

6.9 Appendix

6.9.1 Derivation of gap equation and number equation

Here we analyze the special case where $\xi = 1$, corresponding to a 1D model with translational invariance: $\Delta_q = 0$ unless $q = 0$. Under these circumstances, Eq. (6.6) simplifies to

$$\mathcal{H}_0 \equiv \frac{H}{\mathcal{E}} = \sum_{K,\sigma} (K^2 - \mu) a^\dagger_{K\sigma} a_{K\sigma} + \Delta_0^* f(0) + \Delta_0 f^\dagger(0) - \frac{|\Delta_0|^2}{\beta}, \tag{6.10}$$

where $f(0) = \sum_K e^{-\frac{1}{2}K^2} a_{-K\downarrow} a_{K\uparrow}$.

$\mathcal{H}_0$ can be diagonalized in terms of non-interacting Bogoliubov quasi-particle operators ξ_K, χ_K by the transformation

$$\begin{pmatrix} a_{K\uparrow} \\ a^\dagger_{-K\downarrow} \end{pmatrix} = \begin{pmatrix} u_K & -v_K^* \\ v_K & u_K^* \end{pmatrix} \begin{pmatrix} \xi_K \\ \chi_K^\dagger \end{pmatrix} \tag{6.11}$$

yielding the diagonalized Hamiltonian,

$$\mathcal{H}_0 = \sum_K \left(\epsilon_K (\xi_K^\dagger \xi_K + \chi_K^\dagger \chi_K) + \epsilon_0 - \epsilon_K \right) - \frac{|\Delta_0|^2}{\beta} \tag{6.12}$$

where

$$u_K = \sqrt{\frac{\epsilon_K + \epsilon_0}{2\epsilon_K}}, v_K = \sqrt{\frac{\epsilon_K - \epsilon_0}{2\epsilon_K}} \tag{6.13}$$

$$\epsilon_K = \sqrt{\epsilon_0^2 + |\Delta_0|^2 e^{-K^2}}, \epsilon_0 = K^2 - \mu \tag{6.14}$$

We introduce the dimensionless energy $\mathcal{F} \equiv \left(2\sqrt{2}\pi\tilde{\ell}/L\mathcal{E}\right) \langle GS|H|GS\rangle$, where the ground state $|GS\rangle$ is annihilated by quasi-particle operators ξ_K, χ_K,

$$\mathcal{F} = \int dK \, (\epsilon_0 - \epsilon_K) + \frac{|\Delta_0|^2}{\alpha}, \tag{6.15}$$

where we have taken the continuum limit $\sum_K \to \left(\sqrt{2}L/4\pi\tilde{\ell}\right)\int dK$.

Making $(1/|\Delta_0|)\,\partial\mathcal{F}/\partial|\Delta_0| = 0$ yields the gap equation (6.7). Letting $N = -\left(\sqrt{2}L/4\pi\tilde{\ell}\right)\partial\mathcal{F}/\partial\mu$ yields the number equation (6.8). These equations are further explored in the main text.

6.9.2 Numerical approach

We here describe our numerical approach to solving the BdG equations in the general case where $\xi > 1$. Formally, Eq. (6.6) can be expressed in terms of non-interacting Bogoliubov quasi-particles by a canonical transformation

$$\begin{pmatrix} a_{K_n\uparrow} \\ a^\dagger_{-K_n\downarrow} \end{pmatrix} = \sum_{n'} \begin{pmatrix} u_{n'n} & -v^*_{n'n} \\ v_{n'n} & u^*_{n'n} \end{pmatrix} \begin{pmatrix} \xi_{K_{n'}} \\ \chi^\dagger_{K_{n'}} \end{pmatrix}, \tag{6.16}$$

where we have defined $K_n \equiv K - nK_0$, and $u_{n'n} \equiv u_{n'}(K_n)$, $v_{n'n} \equiv v_{n'}(K_n)$. The matrix elements $u_{n'n}, v_{n'n}$ are governed by the following BdG equations,

$$\epsilon_{K_n} \begin{pmatrix} u_{nn} \\ v_{nn} \end{pmatrix} = \sum_{n'} \begin{pmatrix} \varepsilon_{n'}\delta_{nn'} & \Delta^n_{n'} \\ \left(\Delta^n_{n'}\right)^* & -\varepsilon_{n'}\delta_{nn'} \end{pmatrix} \begin{pmatrix} u_{n,n-n'} \\ v_{n,n-n'} \end{pmatrix} \tag{6.17}$$

where ϵ_{K_n} is the dimensionless excitation energy of Bogoliubov quasi-particles, and $\varepsilon_n = K_n^2 - \mu$, $\Delta^n_{n'} = \Delta_{|n'|K_0} e^{-\frac{1}{8}(2K_n + n'K_0)^2}$, and $\delta_{nn'}$ is the δ-function. In terms of the Bogoliubov operators the Hamiltonian is diagonal,

$$\frac{H}{\mathcal{E}} = \sum_n \left(\sum_{K=-K_0/2}^{K_0/2} (\varepsilon_n - \epsilon_{K_n}) - \frac{|\Delta_{|n|K_0}|^2}{\beta} + \sum_{K=-K_0/2}^{K_0/2} \epsilon_{K_n} \left(\xi^\dagger_{K_n} \xi_{K_n} + \chi^\dagger_{K_n} \chi_{K_n} \right) \right). \tag{6.18}$$

The dimensionless ground state energy $\mathcal{F} = \left(2\sqrt{2}\pi\tilde{\ell}/L\mathcal{E}\right)\langle GS|H|GS\rangle$ can be written as

$$\mathcal{F} = \sum_n \left(\int_{-K_0/2}^{K_0/2} dK\, (\varepsilon_n - \epsilon_{K_n}) + \frac{|\Delta_{|n|K_0}|^2}{\alpha} \right). \tag{6.19}$$

For a given $\{\mu, K_0, \Delta_{|n|K_0}\}$, we truncate Eq. (6.17), and use standard linear algebra packages to extract ϵ_{K_n}. This effectively gives us $\mathcal{F}$ as a function of $\{\mu, \alpha, K_0, \Delta_{|n|K_0}\}$. This $\mathcal{F}$ is a variational upperbound on the true ground state energy. We fix $\{\mu, \alpha\}$ and numerically minimize $\mathcal{F}$, varying $\{K_0, \Delta_{|n|K_0}\}$, using a quasi-Newton algorithm. We restrict the sum over n in Eq. (6.19) to $-\zeta \leq n \leq \zeta$. We find for the parameters studied, our results are independent of ζ if $\zeta \geq 6$.

6.9.3 Linear stability analysis

Here we find the $\xi = 1$ to $\xi = 3$ phase boundary through a linear stability analysis. We take $\Delta_0 > 0$, and assume $\Delta_{K_0} = \Delta_{-K_0} = i\delta$ is small. We have chosen this factor of i, as the unstable direction will then yield real δ. We will calculate $D = \partial^2\mathcal{F}/\partial\delta^2|_{\delta=0}$. For small α the curvature D is positive and the state with $\delta = 0$ is stable. We find the instability by seeking the point with when $D = 0$.

Within our ansatz for $\Delta_{|n|K_0}$, the mean field Hamiltonian is

$$\frac{H}{\mathcal{E}} = \mathcal{H}_0 + i\delta\Lambda - \frac{2\delta^2}{\beta}, \tag{6.20}$$

where

$$\Lambda = f^\dagger(K_0) + f^\dagger(-K_0) - f(K_0) - f(-K_0). \tag{6.21}$$

Making use of the Hellmann-Feynman theorem, the second derivative of $\mathcal{F}$ can be expressed as

$$\begin{aligned}
\frac{\partial^2\mathcal{F}}{\partial\delta^2} &= \frac{2\sqrt{2}\pi\tilde{\ell}}{L}\frac{\partial^2}{\partial\delta^2}\left\langle GS\left|i\Lambda\delta - \frac{2\delta^2}{\beta}\right|GS\right\rangle &(6.22)\\
&= \frac{2\sqrt{2}\pi\tilde{\ell}}{L}\frac{\partial}{\partial\delta}\left\langle GS\left|i\Lambda - \frac{4\delta}{\beta}\right|GS\right\rangle &(6.23)\\
&= -i\frac{4}{\alpha}\frac{\partial}{\partial\delta}\left\langle GS\left|\beta f^\dagger(K_0)\right|GS\right\rangle + \frac{4}{\alpha}. &(6.24)
\end{aligned}$$

Setting $D = \partial^2 \mathcal{F}/\partial\delta^2|_{\delta=0} = 0$, one finds that the points of instability is given by

$$-i = \beta \frac{\partial}{\partial \delta} \left\langle GS \left| f^\dagger(K_0) \right| GS \right\rangle . \tag{6.25}$$

Since the formal manipulations of perturbation theory are more transparent of finite temperature, it is convenient to rewrite Eq. (6.25) as

$$\begin{aligned} -i &= \lim_{\mathcal{T}\to 0} \beta \frac{\partial}{\partial \delta} \frac{\mathrm{Tr}\left(e^{-\mathcal{H}/\mathcal{T}} f^\dagger(K_0)\right)}{\mathrm{Tr}\left(e^{-\mathcal{H}/\mathcal{T}}\right)} \\ &= -i\beta \lim_{\mathcal{T}\to 0} \frac{\int_0^{1/\mathcal{T}} d\tau \, \mathrm{Tr}\left(e^{-\tau\mathcal{H}_0} \Lambda e^{(-1/\mathcal{T}+\tau)\mathcal{H}_0} f^\dagger(K_0)\right)}{\mathrm{Tr}\left(e^{-\mathcal{H}_0/\mathcal{T}}\right)} \end{aligned} \tag{6.26}$$

where $\mathcal{T}$ is a formal parameter.

Substituting the results of Eq. (6.12)-(6.13) to Eq. (6.26), we obtain

$$\alpha \int dK \, \frac{\left(u_K u_{K-K_0} + v_K v_{K-K_0}\right)^2 e^{-\frac{1}{4}(K_0-2K)^2}}{\epsilon_{K-K_0} + \epsilon_K} = 1. \tag{6.27}$$

This integral must be performed numerically, giving the second (right) black solid curve in Fig. 6.1(a).

CHAPTER 7

THEORY OF BOSONS IN TWO-LEG LADDERS WITH LARGE MAGNETIC FIELDS

This chapter was adapted from "Theory of bosons in two-leg ladders with large magnetic fields" by Ran Wei and Erich J. Mueller, published in Physical Review A 89, 063617 (2014).

7.1 Abstract

We calculate the ground state of a Bose gas trapped on a two-leg ladder where Raman-induced hopping mimics the effect of a large magnetic field. In the mean-field limit, where there are large numbers of particles per site, this maps onto a uniformly frustrated two-leg ladder classical spin model. The net particle current always vanishes in the ground state, but generically there is a finite "chiral current", corresponding to equal and opposite flow on the two legs. We vary the strength of the hopping across the rungs of the ladder and the interaction between the bosons. We find three phases: (1) A "saturated chiral current phase" (SCCP), where the density is uniform and the chiral current is simply related to the strength of the magnetic field. In this state the only broken symmetry is the U(1) condensate phase. (2) A "biased ladder phase" (BLP), where the density is higher on one leg than the other. The fluid velocity is higher on the lower density leg, so the net current is zero. In addition to the U(1) condensate phase, this has a broken Z_2 reflection symmetry. (3) A "modulated density phase" (MDP), where the atomic density is modulated along the ladder. In addition to the U(1) condensate phase, this has a second broken U(1) symmetry corresponding to translations of the density wave. We further study the fluctuations of the con-

densate in the BLP, finding a roton-maxon like excitation spectrum. Decreasing the hopping along the rungs softens the spectrum. As the energy of the "roton" reaches to zero, the BLP becomes unstable. We describe the experimental signatures of these phases, including the response to changing the frequency of the Raman transition.

7.2 Introduction

The study of condensed bosons under rotation is an important and rich problem: rotation probes superfluidity [104] just like magnetic fields probe superconductivity [78]. Such systems can be mapped onto a frustrated XY spin model [105], and for large frustration and sufficiently large on-site interactions one finds the bosonic versions of the fractional quantum Hall effect [106, 107, 108, 109]. In the weakly interacting limit there are a rich variety of vortex phases [110]. Here we study a Bose gas trapped on a two-leg ladder where Raman-induced hopping mimics the effect of a large magnetic field.

The bosonic two-leg ladder is appealing, as it is the simplest model for studying the response of bosons to a magnetic field. Thus the experimental observations are particularly easy to interpret. Further, the ladder geometry is straightforward to model, admitting approaches ranging from the density matrix renormalization group [111] through bosonization [112]. In the strongly interacting limit, there is an interesting interplay between Mott physics and the single particle band structure [113, 114, 115, 116, 117, 118]. Here we use a mean-field analysis, which is appropriate for describing experiments on arrays of weakly coupled ladders when the number of particles per site is large.

Experimentalists in Munich have recently engineered this model [15]. Their technique builds upon work performed at NIST, where Raman lasers created artificial magnetic fields in the absence of a lattice [4]. Bloch's group generalized this idea and produced a staggered magnetic flux on an optical lattice [12]. Later, both the Munich and MIT groups extended this to uniform fields [13, 14]. Other approaches to producing artificial gauge fields are reviewed by Dalibard *et al*. [2].

In this chapter, we use a variational approach to analytically calculate the ground state of a bosonic ladder with an analog of a magnetic field. We vary the strength of the hopping aross the rungs of the ladder, and the interaction between the bosons. We find three phases shown in Fig. 7.1: (1) A "saturated chiral current phase" (SCCP), where the density is uniform and opposite currents flow on each leg. The magnitude of the chiral current is set by strength of the magnetic field and is independent of the interactions or the inter-leg hopping strength. In this regime the only spontaneous broken symmetry is the U(1) condensate phase. (2) A "biased ladder phase" (BLP), where the density is higher on one leg than the other. The fluid velocity is higher on the lower density leg, so the net current is zero. In addition to the U(1) condensate phase, this has a spontaneous broken Z_2 reflection symmetry. (3) A "modulated density phase" (MDP), where the atomic density is modulated along the ladder. In addition to the U(1) condensate phase, this has a second spontaneous broken U(1) symmetry corresponding to translations of the density wave. We further study the fluctuations of the condensate in the BLP, finding a roton-maxon like excitation spectrum. Decreasing the hopping along the rungs softens the spectrum. As the energy of the "roton" reaches to zero, the BLP becomes unstable. We describe the experimental signatures of these phases, including the response to changing

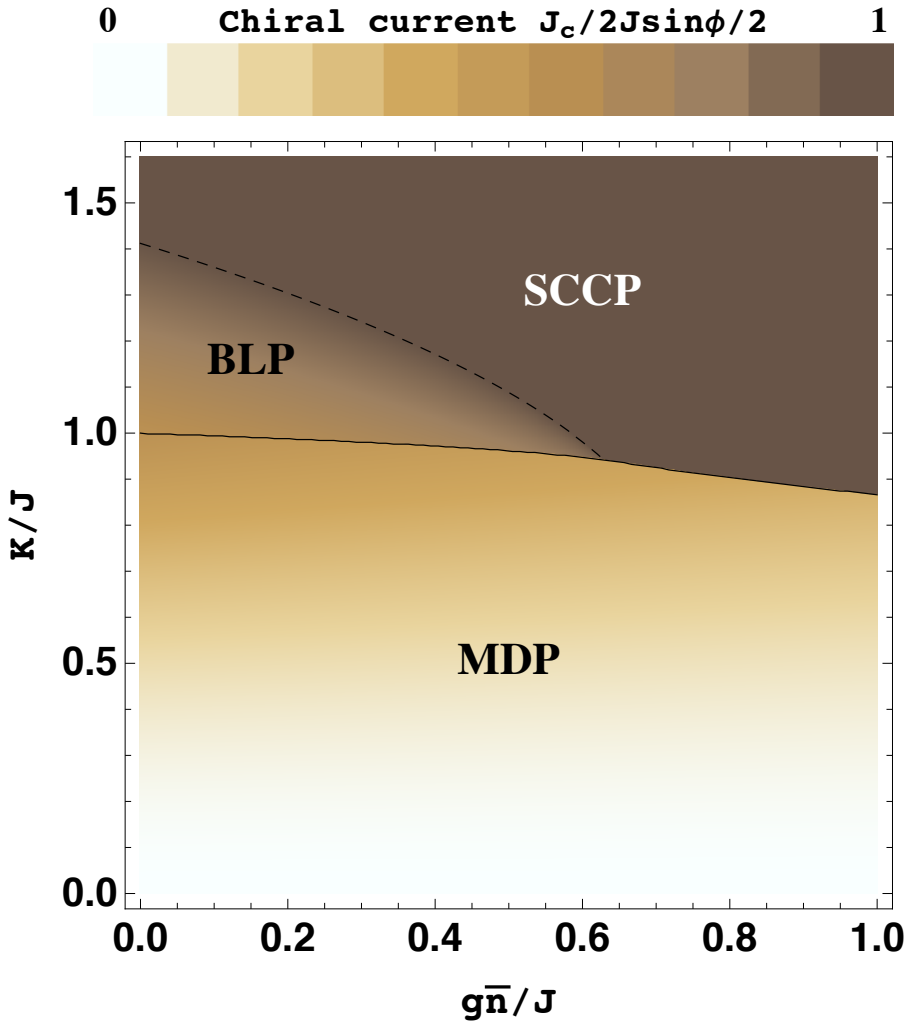

Figure 7.1: Phase diagram of a two-leg bosonic ladder as a function of the tunneling strength K between the legs and interaction strength $g\bar{n}$ for a fixed flux per plaquette $\phi = \pi/2$. These energies are measured in terms of the strength of tunneling along the legs, J. There are three phases: the "saturated chiral current phase" (SSCP), the "biased ladder phase" (BLP) and the "modulated density phase" (MDP). The transition at the solid line is first-order, and the transition at the dashed line is second-order. The color represents the magnitude of the chiral current described by Eq. (7.12). Darker colors correspond to larger currents. The current is constant in the SSCP but varies in the BLP and MDP.

the frequency of the Raman transition.

The SCCP and MDP were first introduced by Orignac and Giamarchi [119],

and the experimentalists interpreted their results in terms of these phases [15]. The BLP has not previously been discussed, but as we explain, the experimental data shows hints of it.

7.3 Model

We consider the Hamiltonian of an interacting Bose gas trapped on a two-leg ladder in a uniform magnetic field,

$$H_0 = -J \sum_{\ell} \left(a^{\dagger}_{\ell+1} a_{\ell} + b^{\dagger}_{\ell+1} b_{\ell} + H.c. \right) - K \sum_{\ell} \left(a^{\dagger}_{\ell} b_{\ell} e^{i\ell\phi} + H.c. \right), \tag{7.1}$$

$$H_1 = \frac{g}{2} \sum_{\ell} \left(a^{\dagger}_{\ell} a^{\dagger}_{\ell} a_{\ell} a_{\ell} + b^{\dagger}_{\ell} b^{\dagger}_{\ell} b_{\ell} b_{\ell} \right), \tag{7.2}$$

where ℓ corresponds to the positions along the ladder and the bosonic operator a_{ℓ} (b_{ℓ}) annihilates a boson on site ℓ of the left (right) leg. The tunneling strength along the legs is J, the tunneling strength across the rungs is K, and the magnetic flux per unit cell is ϕ. The model was proposed by Atala *et al.* to describe their experiment on trapped Rubidium atoms [15]. The intra-leg hopping J is set by the intensity of the lasers which create their lattice potential. The inter-leg hopping K is set by the intensity of a second set of lasers which drive a Raman transition that allows hopping between the legs. The interaction strength g is controlled by modifying the transverse confinement [120]. In the experiment, there is only a weak trap in the z-direction, and g is very small [15]. One could also use a Feshbach resonance to tune g [65].

The single-body Hamiltonian H_0 is characterized by a 2 by 2 matrix in the momentum space,

$$H_0 = \sum_{k} \boldsymbol{c}^{\dagger}_{k} \mathcal{H}(k) \boldsymbol{c}_{k}, \tag{7.3}$$

$$\mathcal{H}(k) \;=\; -2J\cos k\cos\frac{\phi}{2} + 2J\sin k\sin\frac{\phi}{2}\sigma_z - K\sigma_x, \tag{7.4}$$

where $\boldsymbol{c}_k^\dagger = \left(a_k^\dagger, b_k^\dagger\right)$ with $a_k = \frac{1}{\sqrt{L}}\sum_\ell e^{-i\left(k+\frac{\phi}{2}\right)\ell}a_\ell, b_k = \frac{1}{\sqrt{L}}\sum_\ell e^{-i\left(k-\frac{\phi}{2}\right)\ell}b_\ell$, and σ_x, σ_z are the Pauli matrices, and L is the length of the ladder. Note k, ϕ and L are dimensionless. This Hamiltonian is readily diagonalized by

$$\begin{pmatrix} a_k \\ b_k \end{pmatrix} = \begin{pmatrix} \cos\frac{\theta_k}{2} & -\sin\frac{\theta_k}{2} \\ \sin\frac{\theta_k}{2} & \cos\frac{\theta_k}{2} \end{pmatrix}\begin{pmatrix} \alpha_k \\ \beta_k \end{pmatrix} \tag{7.5}$$

with $\tan\theta_k = \frac{-K/J}{2\sin k\sin\frac{\phi}{2}}$, yielding $H_0 = \sum_k\left(E_+(k)\alpha_k^\dagger\alpha_k + E_-(k)\beta_k^\dagger\beta_k\right)$, where the two bands are described by $E_\pm(k) = -2J\cos k\cos\frac{\phi}{2} \pm \sqrt{4J^2\sin^2 k\sin^2\frac{\phi}{2} + K^2}$. For $K \geq 2J\tan\frac{\phi}{2}\sin\frac{\phi}{2}$, the lower band $E_-(k)$ has a single minimum at $k = 0$. For $K < 2J\tan\frac{\phi}{2}\sin\frac{\phi}{2}$, it has two minima at $k = \pm k_0$, where $\frac{\partial E_-}{\partial k}|_{k=\pm k_0} = 0$. We consider the N-body variational wavefunction

$$|G_{k_0}\rangle = \frac{1}{\sqrt{N!}}\left(\cos\gamma\beta_{k_0}^\dagger + \sin\gamma\beta_{-k_0}^\dagger\right)^N|\text{vac}\rangle, \tag{7.6}$$

where $|\text{vac}\rangle$ is the vacuum state and $0 < \gamma < \pi/2$ for $k_0 > 0$ and $\gamma = 0$ for $k_0 = 0$. In the absence of interactions, this is the ground state for any choice of γ. Even infinitesimal interactions, however, can split this degeneracy.

7.4 Current and density

In this section we explore the properties of Eq. (7.6). In particular we calculate densities and currents, which are experimental observables [15].

To satisfy the continuity equation, we define the net current and the chiral current,

$$J_n \equiv \frac{1}{N}\left\langle G_{k_0}\left|\sum_k \boldsymbol{c}_k^\dagger\frac{\partial\mathcal{H}(k)}{\partial k}\boldsymbol{c}_k\right|G_{k_0}\right\rangle = \cos^2\gamma\left(J_{k_0}^a + J_{k_0}^b\right) + \sin^2\gamma\left(J_{-k_0}^a + J_{-k_0}^b\right), \tag{7.7}$$

$$J_c \equiv \frac{1}{N}\left\langle G_{k_0}\left|\sum_k \boldsymbol{c}_k^\dagger \sigma_z \frac{\partial \mathcal{H}(k)}{\partial k}\boldsymbol{c}_k\right|G_{k_0}\right\rangle = \cos^2\gamma\left(J^a_{k_0}-J^b_{k_0}\right)+\sin^2\gamma\left(J^a_{-k_0}-J^b_{-k_0}\right), \quad (7.8)$$

where the currents on each leg are

$$J^a_{k_0} = 2J\sin\left(k_0+\frac{\phi}{2}\right)\sin^2\frac{\theta_{k_0}}{2}, \quad (7.9)$$

$$J^b_{k_0} = 2J\sin\left(k_0-\frac{\phi}{2}\right)\cos^2\frac{\theta_{k_0}}{2}. \quad (7.10)$$

Using the equation $\frac{\partial E_-(k)}{\partial k}|_{k=\pm k_0}=0$ and the relation $\sin^2\frac{\theta_{k_0}}{2}=\cos^2\frac{\theta_{-k_0}}{2}$, one can read off $J^a_{k_0}=J^a_{-k_0}=-J^b_{k_0}=-J^b_{-k_0}$. This implies the net current always vanishes at equilibrium and the chiral current is independent of γ:

$$J_n = 0, \quad (7.11)$$

$$J_c = 4J\sin\left(k_0+\frac{\phi}{2}\right)\sin^2\frac{\theta_{k_0}}{2}. \quad (7.12)$$

We also define the local density on each leg,

$$n^a(\ell) \equiv \left\langle G_{k_0}\left|a^\dagger_\ell a_\ell\right|G_{k_0}\right\rangle = \bar{n}^a+\delta n^a_\ell \quad (7.13)$$

$$n^b(\ell) \equiv \left\langle G_{k_0}\left|b^\dagger_\ell b_\ell\right|G_{k_0}\right\rangle = \bar{n}^b+\delta n^b_\ell, \quad (7.14)$$

where the average density on each is $\bar{n}^a/\bar{n}=\cos^2\gamma\sin^2\frac{\theta_{k_0}}{2}+\sin^2\gamma\cos^2\frac{\theta_{k_0}}{2}$ and $\bar{n}^b/\bar{n}=\cos^2\gamma\cos^2\frac{\theta_{k_0}}{2}+\sin^2\gamma\sin^2\frac{\theta_{k_0}}{2}$, where $\bar{n}=N/L$ is the average density. The density modulations are the same on each leg: $\delta n^a_\ell/\bar{n}_a=\delta n^b_\ell/\bar{n}_b=\frac{1}{2}\sin2\gamma\sin\theta_{k_0}\cos2k_0\ell$. Note the modulation is largest at $\gamma=\pi/4$ and vanishes at $\gamma=0$.

7.5 Phase diagram

We now consider the interaction term H_1. Treating Eq. (7.6) variationally and allowing k_0 to be a free parameter, we study the energy

$$E(\gamma,k)\equiv\frac{1}{N}\langle G_k|H_0+H_1|G_k\rangle = E_-(k)+E_{\rm int}(k), \quad (7.15)$$

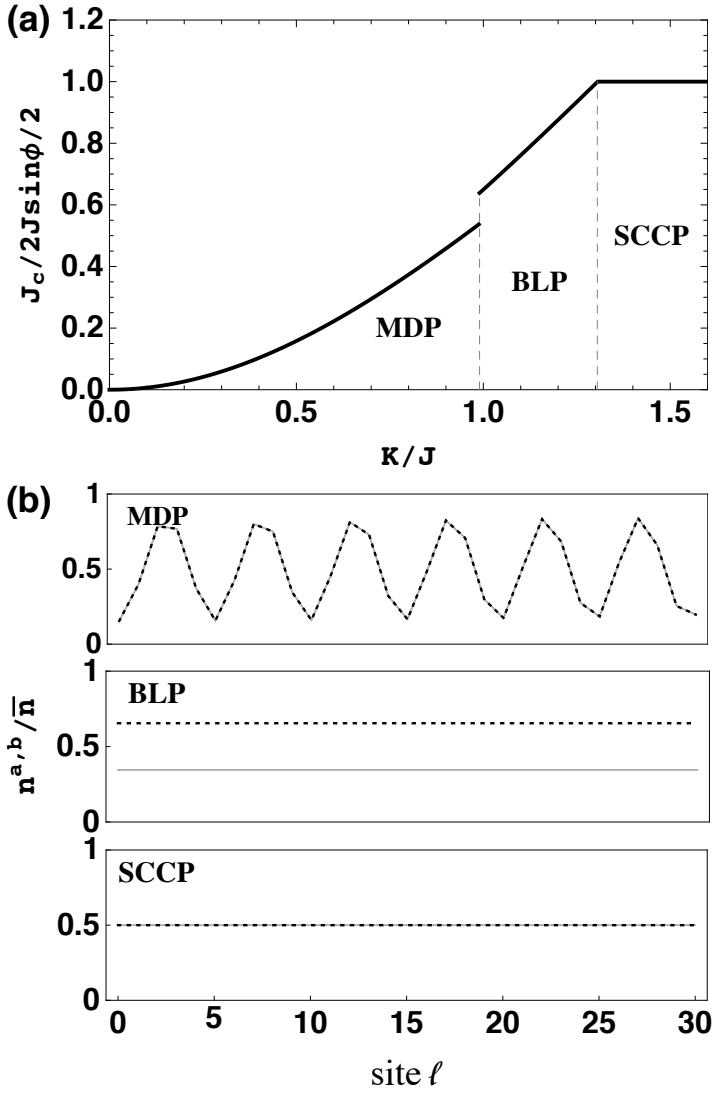

Figure 7.2: Chiral current and atomic density. (a) Chiral current as a function of tunneling strength K/J. The current is discontinuous at the boundary between the MDP and BLP, indicating a first-order transition, whereas the current is continuous across the BLP to SCCP boundary. The slope is discontinuous indicating a second-order transition. (b) Atomic density as a function of lattice site ℓ. In the MDP, the density of each leg is equal but modulated along the ladder. In the BLP, the density is higher on one leg than the other. In the SCCP, the density of each leg is equal and uniform. For these plots the interaction strength is $g\bar{n}/J = 0.2$ and the magnetic flux is $\phi = \pi/2$.

where

$$E_{\text{int}}(k) = \frac{g\bar{n}}{2}\left(\left(\frac{3}{4}\sin^2\theta_k - \frac{1}{2}\right)\sin^2 2\gamma - \frac{1}{2}\sin^2\theta_k + 1\right).$$

(7.16)

This ansatz describes the three phases in Fig. 7.1. We minimize $E(\gamma, k)$ with respect to γ and k. The only γ-dependence is in Eq. (7.16). For $\frac{3}{4}\sin^2\theta_k - \frac{1}{2} \geq 0$, the energy minimum is at $\gamma = 0$. For $\frac{3}{4}\sin^2\theta_k - \frac{1}{2} < 0$, the energy minimum is at $\gamma = \pi/4$. As can be inferred from the expressions following Eq. (7.5), $\sin^2\theta_k = \frac{K^2}{K^2+4J^2\sin^2 k \sin^2\phi/2}$.

For $\gamma = 0$, the density is uniform along the ladder, and the chiral current is given by Eq. (7.12), with $\frac{\partial E(\gamma=0,k)}{\partial k}|_{k=\pm k_0} = 0$. When $k_0 = 0$, the density of the each leg is equal, with $n_a = n_b = n_0/2$, and the chiral current is saturated, with $J_c = 2J\sin\frac{\phi}{2}$. We call this phase the "saturated chiral current phase" (SCCP), as shown in Fig. 7.2. In the SCCP, the only broken symmetry is the U(1) condensate phase. For $k_0 > 0$, the density is higher on one leg than the other, which breaks the Z_2 reflection symmetry. We call this phase the "biased ladder phase" (BLP). The transition between the BLP and SCCP is second-order, and as illustrated in Fig. 7.2(a), the chiral current is continuous across transition. Note the BLP has a two-fold degeneracy since the choice of the leg with a higher (lower) density is arbitrary. In our ansatz, this two-fold degeneracy is associated with symmetry $k_0 \to -k_0$.

For $\gamma = \pi/4$, the density is modulated along the ladder, which supplements the broken U(1) condensate phase, with a second broken U(1) symmetry: the energy is unchanged if one adds an arbitrary phase to $\beta^\dagger_{k_0}$ or $\beta^\dagger_{-k_0}$ in Eq. (7.6). This second U(1) phase is related to translations of the density modulation. We call this regime the "modulated density phase" (MDP). The transition between MDP and the former two phases is first-order, as γ changes discontinuously. Furthermore, we see the chiral current has a discontinuous jump between the

MDP and BLP in Fig. 7.2(a). The size of the current jump is determined by the interaction strength g, and disappears when g is zero.

Note for $\gamma = \pi/4$, Eq. (7.6) is a special case of a more generic ansatz $|T_{k_0}\rangle = \frac{1}{\sqrt{N!}}\left(\sum_n c_n \beta^\dagger_{nk_0}\right)^N |\text{vac}\rangle$ where $\sum_n |c_n|^2 = 1$ [16]. Although we do not plot the results, we have studied this more general ansatz. We find very few changes: the boundary between the phases is only shifted to a slightly larger tunneling strength K/J. The symmetry of each phase is unchanged. The shift vanishes as $g \to 0$.

7.6 Stability and Roton

We now study the stability of Eq. (7.6) when $\gamma = 0$. We find the excitation spectrum of the BLP has a maxon-roton like structure.

To calculate the excitation spectrum, we truncate the Hamiltonian to the lowest band

$$H = \sum_k E_-(k)\beta^\dagger_k \beta_k + \frac{1}{2L}\sum_{kpq} \Gamma_{kpq}\beta^\dagger_{k+q}\beta^\dagger_{p-q}\beta_p\beta_k \tag{7.17}$$

where

$$\Gamma_{kpq} = g\Big(\sin\frac{\theta_{k+q}}{2}\sin\frac{\theta_{p-q}}{2}\sin\frac{\theta_p}{2}\sin\frac{\theta_k}{2} + \cos\frac{\theta_{k+q}}{2}\cos\frac{\theta_{p-q}}{2}\cos\frac{\theta_p}{2}\cos\frac{\theta_k}{2}\Big). \tag{7.18}$$

The ansatz in Eq. (7.6) with $\gamma = 0$ is equivalent to setting $\beta_k = \sqrt{N}\delta_{kk_0}$. We add fluctuations, writing $\beta_k = \sqrt{N}\delta_{kk_0} + (1-\delta_{kk_0})\chi_{k-k_0}$. To quadratic order in the operators χ_k,

$$\bar{H} = -\frac{gN\bar{n}}{2}\left(\sin^4\frac{\theta_{k_0}}{2} + \cos^4\frac{\theta_{k_0}}{2}\right) - \sum_{k>0}\zeta(-k)$$

$$+ \quad \sum_{k>0} \left(\chi_k^\dagger, \chi_{-k}\right) \begin{pmatrix} \zeta(k) & \eta(k) \\ \eta(k) & \zeta(-k) \end{pmatrix} \begin{pmatrix} \chi_k \\ \chi_{-k}^\dagger \end{pmatrix} \tag{7.19}$$

where

$$\zeta(k) = E_-(k+k_0) + 2g\bar{n}\left(\sin^2\frac{\theta_{k_0}}{2}\sin^2\frac{\theta_{k_0+k}}{2} + \cos^2\frac{\theta_{k_0}}{2}\cos^2\frac{\theta_{k_0+k}}{2}\right) - \mu, \tag{7.20}$$

$$\eta(k) = g\bar{n}\left(\sin^2\frac{\theta_{k_0}}{2}\sin\frac{\theta_{k_0+k}}{2}\sin\frac{\theta_{k_0-k}}{2} + \cos^2\frac{\theta_{k_0}}{2}\cos\frac{\theta_{k_0+k}}{2}\cos\frac{\theta_{k_0-k}}{2}\right), \tag{7.21}$$

where we have subtracted the chemical potential $\mu = E_-(k_0) + g\bar{n}\left(\sin^4\frac{\theta_{k_0}}{2} + \cos^4\frac{\theta_{k_0}}{2}\right)$ and defined $\bar{H} = H - \mu N$. We perform the Bogoliubov transformation $\chi_k = u\rho_{-k} - v\rho_k^\dagger$ and $\chi_{-k}^\dagger = -v\rho_{-k} + u\rho_k^\dagger$, where ρ_k is the bosonic quasiparticle and $u^2 - v^2 = 1$. The Hamiltonian is then diagonalized as

$$\bar{H}/N = \sum_{k>0} \epsilon_k \rho_k^\dagger \rho_k + \epsilon_{-k}\rho_{-k}^\dagger \rho_{-k} + \text{const.} \tag{7.22}$$

where the Bogoliubov excitation spectrum is

$$\epsilon_k = \sqrt{\frac{(\zeta(k)+\zeta(-k))^2}{4} - \eta^2(k)} + \frac{\zeta(-k) - \zeta(k)}{2}. \tag{7.23}$$

In the BLP, this spectrum has a maxon-roton like structure, as shown in Fig. 7.3. Decreasing the tunneling strength K/J softens the spectrum. As the energy of the roton reaches to zero, the BLP becomes unstable. This corresponds to a spinodal, and the first-order transition between the BLP and MDP generically preempts it.

7.7 Experimental signatures

In this section we describe experimental signatures of these phases. A local density measurement can distinguish the three phases, as can a measure of local

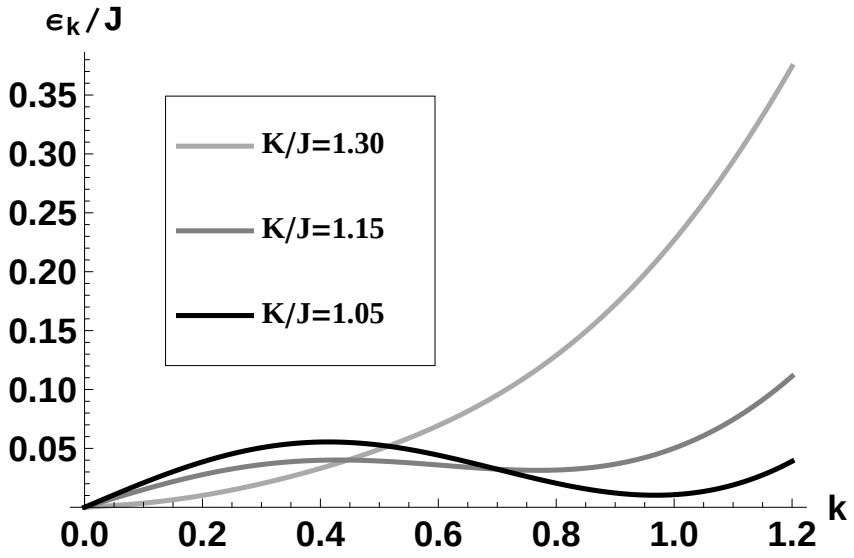

Figure 7.3: Bogoliubov excitation spectrum ϵ_k/J for $g\bar{n}/J = 0.2$. The "maxon-roton" like structure develops as one decreases the tunneling strength K/J. When the energy of the "roton" hits zero, the BLP is unstable. This corresponds to a spinodal, and the first-order thermodynamic BLP-MDP phase transition generically preempts it.

currents. Some of the phases can be distinguished via time-of-flight measurements. Finally, we argue that a susceptibility measurement can readily identify the BLP.

While local density and current measurements can be difficult, the experimentalists in Ref. [15] devised an ingenious surrogate. They isolate each leg of their ladder and further break each leg into a set of dimers. By looking at the time evolution of this ensemble of isolated dimers, they extract averages of various local correlation functions. In particular they find that the chiral current saturates for $K/J > \sqrt{2}$. Given their weak interactions, this is consistent with the SCCP in Fig. 7.1. They also find signatures of spatial inhomogeneities along each leg for $K/J < 1$ (see Fig. 4(b) of Ref. [15]). This is consistent with a transition to the MDP. For $1 < K/J < \sqrt{2}$, they appear to have a state which is translationally invariant along the ladder, and has a non-saturated chiral cur-

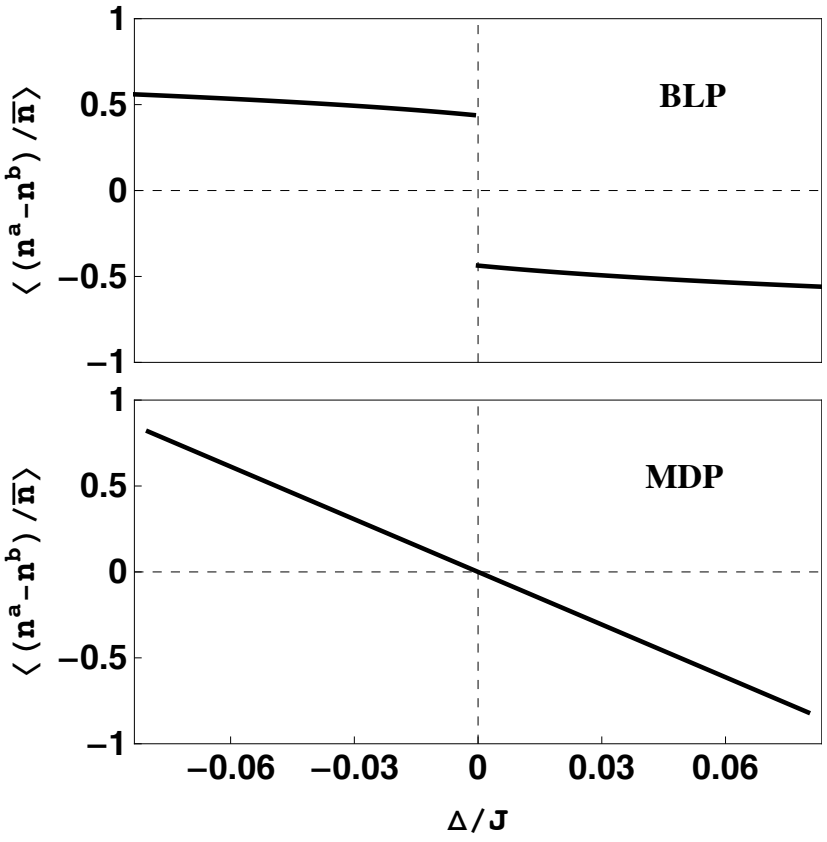

Figure 7.4: Averaged density asymmetry $\left\langle \left(n^a - n^b\right)/\bar{n} \right\rangle$ as a function of the detuning Δ/J. The density is calculated by averaging over 30 sites along the ladder, where we set $g\bar{n}/J = 0.2$, and $K/J = 0.2$ for the MDP and $K/J = 1.1$ for the BLP.

rent. This is consistent with the BLP. The experimentalists interpreted their data in terms of the SCCP and MDP, which they referred to as the "Meisner phase" and "vortex phase". They were unaware of the possibility of the BLP, as it has not been previously discussed. The experimentalists make a plot of J_c vs K/J, similar to Fig. 7.2(a). While the phase transitions should all be visible in this graph, the discontinuity between the BLP and MDP vanishes as the interaction parameter $g \to 0$.

Another direct probe of these states is the left-right asymmetry $\delta = n^a - n^b$. In the BLP, $\delta \neq 0$. Unfortunately, the experiment is performed on an array of

ladders, and one would expect each ladder to randomly have $\delta > 0$ or $\delta < 0$. The ensemble average will be zero in all phases. To avoid this issue, we propose a susceptibility measurement. We envision detuning the Raman lasers from resonance, which adds to Eq. (7.1) a term $H_\Delta = \sum_\ell \Delta \left(a_\ell^\dagger a_\ell - b_\ell^\dagger b_\ell \right)$. Such a term can also be engineered by adjusting the geometry of their lattice beams. In the BLP, any bias Δ, no matter how small, will yield a finite left-right asymmetry. In the MDP or SCCP, the asymmetry will instead be linear in Δ.

Figure 7.4 shows the averaged density asymmetry $\left\langle \left(n^a - n^b \right) / \bar{n} \right\rangle$ as a function of the detuning Δ/J over 30 sites along one ladder. The discontinuity seen for the BLP can be interpreted as a divergent susceptibility. In an experiment one would likely see hysteresis in the chiral current for the BLP. By contrast the MDP has a finite susceptibility.

Finally we consider time-of-flight expansion. In principle one can use this technique to directly measure the momenta of all the particles. In the SCCP, the atoms on the left legs all have momentum $k_0 = \phi/2$ along the ladder, and the atoms on the right legs all have momentum $-k_0$. In the BLP the characteristic momentum is reduced to $k_0 < \phi/2$, but there is still only one momentum peak for each leg. In the MDP the distribution is bimodal: on each leg there are two different momenta.

To fully interpret time-of-flight images from arrays of ladders, one must take into account inter-ladder coherences. Thus we consider a more general two dimensional model with

$$\begin{aligned} H_0 &= -J \sum_{\ell j} \left(a_{\ell+1}^{(j)\dagger} a_\ell^{(j)} + b_{\ell+1}^{(j)\dagger} b_\ell^{(j)} + H.c. \right) - K \sum_{\ell j} \left(a_\ell^{(j)\dagger} b_\ell^{(j)} e^{i(\ell+j)\phi} + H.c. \right) \\ &- \Lambda \sum_{\ell j} \left(e^{-i\lambda} a_\ell^{(j+1)\dagger} b_\ell^{(j)} e^{i(\ell+j+1)\phi} + H.c. \right), \end{aligned} \tag{7.24}$$

where the superscript labels the ladder, and the tunneling strength between adjacent ladders is Λ. The phase factors $e^{i(\ell+j)\phi}$ and $e^{i(\ell+j+1)\phi}$ are related to the experimental geometry of the Raman beams, and $e^{-i\lambda}$ involves details of the excited state in the Raman transition. Diagonalizing this Hamiltonian in momentum space, one finds the lower energy band $E_-(k_x, k_y) = -2J\cos k_y \cos(\phi/2) - \sqrt{4J^2 \sin^2 k_y \sin^2(\phi/2) + K^2 + \Lambda^2 + 2K\Lambda\cos(k_x + \lambda - \phi)}$, where k_y is the canonical momentum in the y-direction (along the leg of the ladder), and k_x is the canonical momentum in the x-direction (perpendicular to the leg of the ladder). Time-of-flight measures the real momentum, $\boldsymbol{p}$, where $a_{\boldsymbol{p}} = a_{\boldsymbol{k}-\boldsymbol{q}}$ and $b_{\boldsymbol{p}} = b_{\boldsymbol{k}+\boldsymbol{q}}$ with $\boldsymbol{q} = (\phi/2)(\hat{x} + \hat{y})$. For completely decoupled ladders, $\Lambda = 0$, the energy is independent of k_x. For any finite coupling, $\Lambda > 0$, the energy minimum is given by $k_x = \phi - \lambda$. We then see that the atoms on the left legs have $p_x = k_x - \phi/2 = \phi/2 - \lambda$, and the atoms on the right legs have $p_x = k_x + \phi/2 = 3\phi/2 - \lambda$. Thus atoms from the two legs become spatially separated during time-of-flight. This spatial structure is seen in Ref. [15].

7.8 Conclusions

We have studied the ground state of a bosonic two-leg ladder in a magnetic field. We found three phases, corresponding to different types of broken symmetries. We further studied the fluctuation of the condensate and found a roton-maxon like excitation spectrum. Finally, we described the experimental evidence of these phases, and proposed a susceptibility measurement to further characterize them.

CHAPTER 8

MAJORANA FERMIONS IN ONE DIMENSIONAL SPIN-ORBIT COUPLED FERMI GASES

This chapter was adapted from "Majorana fermions in one dimensional spin-orbit-coupled Fermi gases" by Ran Wei and Erich J. Mueller, published in Physical Review A 86, 063604 (2012).

8.1 Abstract

We theoretically study trapped one dimensional Fermi gases in the presence of spin-orbit coupling induced by Raman lasers. The gas changes from a conventional (non-topological) superfluid to a topological superfluid as one increases the intensity of the Raman lasers above a critical chemical-potential dependent value. Solving the Bogoliubov-de Gennes equations self-consistently, we calculate the density of states in real and momentum space at finite temperatures. We study Majorana fermions (MFs) which appear at the boundaries between topologically trivial and topologically non-trivial regions. We linearize the trap near the location of a MF, finding an analytic expression for the localized MF wavefunction and the gap between the MF state and other edge states.

8.2 Introduction

Majorana fermions (MFs), exotic excitations which are their own antiparticles, have attracted a great deal of attention recently [121, 122]. Condensed matter systems with MFs possess degeneracies that are intrinsically nonlocal, and can

be manipulated geometrically. They can, in principle, be used to make a robust quantum computer [123]. Condensed matter theorists have proposed various ways to explore MFs during the past several years [124, 125, 126, 127, 128, 129, 130, 131, 132, 133]. Four experimental groups have recently reported evidence of MFs in semiconducting wires on superconducting substrates [134, 135, 136, 137]. In those experiments, spin-orbit (SO) coupling was important. Here we study MFs in a related cold atom system.

Two groups [138, 139] have successfully generated SO coupled Fermi gases based on a Raman technique pioneered by Spielman's group at NIST [6]. Several theoretical groups have proposals for creating and probing MFs in these SO coupled Fermi gases [140, 141, 142, 143, 144, 145, 146]. We build upon the studies of Jiang *et al.* [144] and Liu *et al.* [145], which find MFs in a 1D geometry.

We study a 1D (pseudo) spin-1/2 Fermi gas with point interactions. In the presence of Raman lasers, the energy spectrum has two helical bands. We study this two-band model in a harmonic trap. Solving the Bogoliubov-de Gennes (BdG) equations self-consistently, we calculate the density of states (DOS) in real and momentum space at finite temperatures. We linearize the trap near the location of a MF, finding an analytic expression for the localized MF wavefunction and the gap between the MF state and other edge states.

Our numerical calculations extend the similar studies of Ref. [145]. We explore a larger range of temperatures, and delve deeper into the physics near the MFs. We also investigate a truncated one-band model.

One concern with mean-field calculations such as ours, is that they are unable to capture the large phase fluctuations found in 1D. As shown by Ref. [147,

148, 149], the MF physics is robust against these fluctuations. Moreover, an actual experiment would be performed on a bundle of weakly coupled tubes [150]. This latter setting also avoids issues of number conservation [147, 148, 149]. Our 1D model faithfully describes the properties of a single tube within such a bundle when the tunneling is weak.

This chapter is organized as follows. In Sec. II, we discuss the homogeneous gas: We start with the two-band model, and in Sec. II(A) show how it relates to a one-band model with p-wave interactions. In Sec. II(B), we describe the band structure and topology of the two-band model. In Sec. III, we calculate the properties of trapped gases: In Sec. III(A), we write the BdG equations and self-consistently calculate the order parameter and density. In Sec. III(B), we visualize the MFs by calculating the DOS in real space and momentum space. In Sec. III(C), we introduce MF operators and construct the localized MF states. In Sec. III(D), we linearize the trap near the location of a MF, finding an analytic expression for the localized MF wavefunction and the gap between the MF state and other edge states. Finally we conclude in Sec. IV.

8.3 Homogeneous gas

We start from the Hamiltonian of the 1D (pseudo) spin-1/2 Fermi gases with chemical potential μ,

$$H = \int dx\, \Psi^\dagger(x)\,(H_0(x) - \mu)\,\Psi(x) + H_I, \tag{8.1}$$

where $\Psi(x) = (\psi_\uparrow(x), \psi_\downarrow(x))^\intercal$ annihilates the spin-up and spin-down states. In an experiment, $\psi_\uparrow$ and $\psi_\downarrow$ correspond to two different hyperfine states of a fermionic atom such as ^{40}K. The single-particle Hamiltonian $H_0(x) = -\frac{\hbar^2}{2m}\partial_x^2 + \frac{i\hbar^2 k_L}{m}\partial_x\sigma_z +$

$\frac{\hbar\Omega}{2}\sigma_x + E_r$ can be engineered by Raman lasers [6], whose intensity is characterized by the Rabi frequency Ω. The recoil momentum of the Raman lasers is $\hbar k_L$, $E_r = \hbar^2 k_L^2/2m$ is the recoil energy, and $\boldsymbol{\sigma} = (\sigma_x, \sigma_y, \sigma_z)$ is the vector of Pauli matrices. For ultra-cold fermions, the interaction may be modeled by $H_I = g_{1D} \int dx \psi_\uparrow^\dagger(x)\psi_\downarrow^\dagger(x)\psi_\downarrow(x)\psi_\uparrow(x)$, with coupling constant g_{1D}. This coefficient can be related to the three-dimensional scattering length and the geometry of the confinement [23]. In a typical experiment, $|g_{1D}| \sim 70\, a_0 E_r$ [150], where a_0 is the Bohr radius. We restrict ourselves to attractive interactions, $g_{1D} < 0$. We note that if we rotate our spin basis ($\sigma_x \to \sigma_z, \sigma_z \to \sigma_y$) and identify $Z = \hbar\Omega/2$ as a Zeeman field, and $\alpha = \hbar^2 k_L/2m$ as the SO coupling strength, we recover the Hamiltonian of a semiconducting wire. Note H_I is very different for a wire [125, 126, 127, 128, 129, 130]. In the following sections we explore the physics of Eq. (8.1).

8.3.1 One-band model

To get insight into Eq. (8.1), we first consider an approximation where we truncate to a single band. We emphasize however that in all other sections, we work with the full two-band Hamiltonian.

The physics of the single particle Hamiltonian is most transparent in momentum space, $H = \sum_k \Psi_k^\dagger \left(\frac{\hbar^2 k^2}{2m} + E_r - \frac{\hbar^2 k k_L}{m}\sigma_z + \frac{\hbar\Omega}{2}\sigma_x\right)\Psi_k$, where $\Psi_k = (\psi_{k\uparrow}, \psi_{k\downarrow})^\intercal$. This Hamiltonian is readily diagonalized by

$$\begin{pmatrix} d_k \\ c_k \end{pmatrix} = \begin{pmatrix} \cos\frac{\theta_k}{2} & \sin\frac{\theta_k}{2} \\ -\sin\frac{\theta_k}{2} & \cos\frac{\theta_k}{2} \end{pmatrix} \begin{pmatrix} \psi_{k\uparrow} \\ \psi_{k\downarrow} \end{pmatrix} \tag{8.2}$$

with $\tan\theta_k = -m\Omega/2k\hbar k_L$, yielding $H = \sum_k \left(E_- c_k^\dagger c_k + E_+ d_k^\dagger d_k\right)$. The energy spec-

trum has two helical bands, illustrated in Fig. 8.1. If the effective chemical

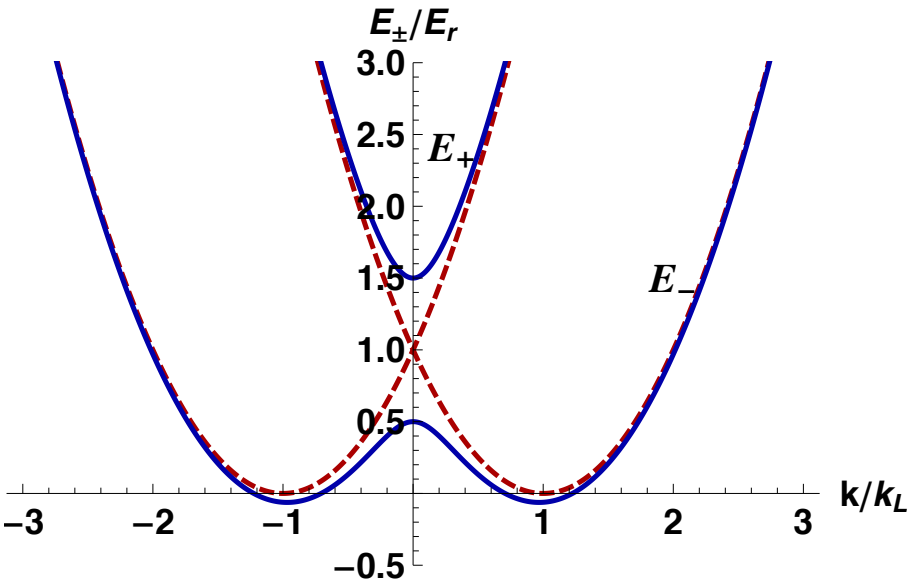

Figure 8.1: Band structure of a 1D (pseudo) spin-1/2 gas. The red (dashed) curves are the bare bands in the absence of SO coupling. The blue (thick) curves are the upper band E_+ and lower band E_- in the presence of SO coupling, with the coupling strength $\hbar\Omega/E_r = 1$.

potential $\tilde{\mu} = \mu - E_r \ll \hbar\Omega/2$, only the lower band E_- is filled with fermions. Projecting the interactions into this band, we find

$$H_I^{1B} = \tilde{g}_{1D} \sum_{kqq'} \left(V_{kq} c^\dagger_{\frac{k}{2}+q} c^\dagger_{\frac{k}{2}-q} \right) \left(V_{kq'} c_{\frac{k}{2}-q'} c_{\frac{k}{2}+q'} \right), \tag{8.3}$$

where $\tilde{g}_{1D} = g_{1D}/L_{1D}$, with L_{1D} the length of the gas. The fermionic anticommutation relation, $c^\dagger_{k/2+q} c^\dagger_{k/2-q} = -c^\dagger_{k/2-q} c^\dagger_{k/2+q}$, implies that the interaction coefficient V_{kq} is odd with respective to q, $V_{kq} = \frac{1}{2}\sin\frac{\theta_{k/2+q} - \theta_{k/2-q}}{2}$. At zero center of mass momentum, $V_q \equiv V_{k=0,q} = \frac{q}{2\sqrt{q^2 + \hbar^2 k_L^2 \Omega^2/16 E_r^2}}$. In Fig. 8.2, we plot V_{kq} as a function of q. The dependence on k is weak for $k \lesssim k_L$.

The interaction in Eq. (8.3) is separable. Given that $\tilde{g}_{1D} < 0$, this interaction can lead to pairing with zero center of mass and an order parameter $\Delta_q = \tilde{g}_{1D} V_q \sum_{q'} \left\langle V_{q'} c_{-q'} c_{q'} \right\rangle$, where $\langle ... \rangle \equiv \frac{\mathrm{Tr}\left(e^{-H/k_b T} ...\right)}{\mathrm{Tr}\left(e^{-H/k_b T}\right)}$ is the thermal average, k_b is

the Boltzman constant and T is the temperature. The mean-field interaction becomes $H_I^{1B} = \sum_q \left(\Delta_q c_q^\dagger c_{-q}^\dagger + \Delta_q^* c_{-q} c_q\right) - \tilde{g}_{1D} \left|\sum_q V_q \left\langle c_{-q} c_q \right\rangle\right|^2$. By virtue of the symmetry of V_q, the order parameter has a p-wave symmetry $\Delta_{-q} = -\Delta_q$. As is well established, such a p-wave superfluid may possess Majorana edge modes [42]. We will discuss these Majorana modes at length in the two-band model.

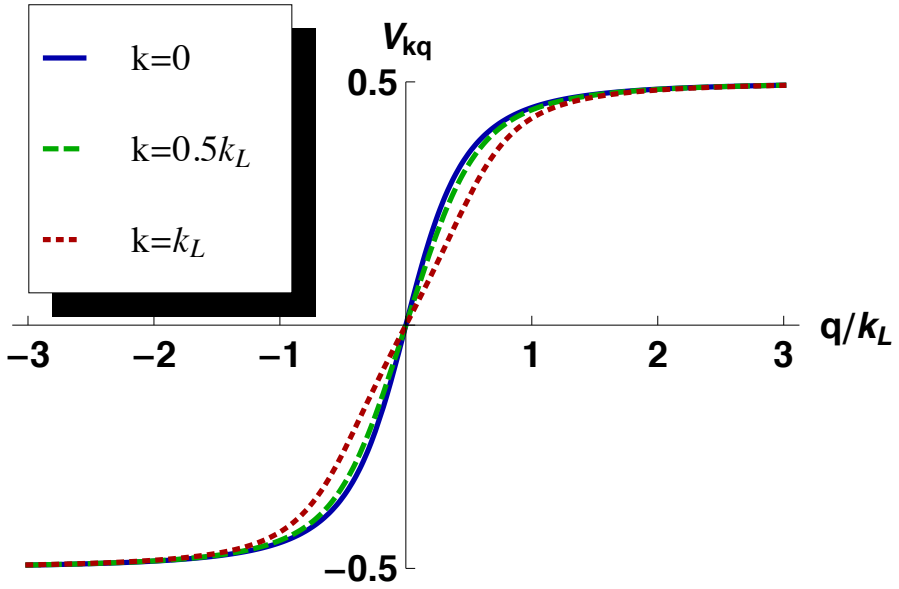

Figure 8.2: Interaction coefficient V_{kq} versus dimensionless momentum q/k_L for $\hbar\Omega/E_r = 2$. The blue (thick), green (dashed) and red (dotted) curves correspond to $k = 0, 0.5k_L$ and k_L respectively.

8.3.2 Two-band model

While the one-band model connects the SO coupled gases and p-wave superconductors, we will focus on the richer two-band model in the remainder of the chapter. Within the mean-field approach, the interaction term is bilinear

$$H_I = g_{1D} \int dx \psi_\uparrow^\dagger(x) \psi_\downarrow^\dagger(x) \psi_\downarrow(x) \psi_\uparrow(x) \tag{8.4}$$

$$\approx \int dx \left(\Delta(x) \left(\psi_\uparrow^\dagger(x) \psi_\downarrow^\dagger(x) + \psi_\downarrow(x) \psi_\uparrow(x) \right) - \frac{\Delta(x)^2}{g_{1D}} \right), \tag{8.5}$$

where the order parameter $\Delta(x) = g_{1D} \langle \psi_\downarrow(x) \psi_\uparrow(x) \rangle$ is assumed to be real. Defining the operator $\tilde{\Psi}^\dagger(x) = \left(\psi_\uparrow^\dagger(x), \psi_\downarrow^\dagger(x), \psi_\downarrow(x), \psi_\uparrow(x) \right)$, the Hamiltonian can be written as,

$$H = \int \left(\frac{1}{2} \tilde{\Psi}^\dagger(x) \mathcal{H} \tilde{\Psi}(x) - \frac{\Delta(x)^2}{g_{1D}} \right) dx + \frac{1}{2} \left(T_- + T_+ \right), \tag{8.6}$$

where

$$\mathcal{H} = \left(-\frac{\hbar^2}{2m} \partial_x^2 - \tilde{\mu} \right) \tau_z + \frac{i \hbar^2 k_L}{m} \partial_x \tau_z \sigma_z + \frac{\hbar \Omega}{2} \tau_z \sigma_x + \Delta(x) \tau_x \sigma_z, \tag{8.7}$$

$$T_\pm = \mathrm{Tr} \left(-\frac{\hbar^2}{2m} \partial_x^2 - \tilde{\mu} \pm \frac{i \hbar^2 k_L}{m} \partial_x \right). \tag{8.8}$$

The Pauli matrices $\boldsymbol{\sigma}, \boldsymbol{\tau}$ operate in the spin subspace and particle-hole subspace respectively,

$$\sigma_x = \begin{pmatrix} & 1 & & \\ 1 & & & \\ & & & 1 \\ & & 1 & \end{pmatrix}, \tau_x = \begin{pmatrix} & & 1 & \\ & & & 1 \\ 1 & & & \\ & 1 & & \end{pmatrix} \tag{8.9}$$

$$\sigma_z = \begin{pmatrix} 1 & & & \\ & -1 & & \\ & & 1 & \\ & & & -1 \end{pmatrix}, \tau_z = \begin{pmatrix} 1 & & & \\ & 1 & & \\ & & -1 & \\ & & & -1 \end{pmatrix}. \tag{8.10}$$

The elementary excitations can be found by solving the BdG equations $\mathcal{H} W = E W$. When $\Delta(x) = \Delta$ is spatially homogeneous, one can write the BdG equations in momentum space as $\mathcal{H}_k W(k) = E(k) W(k)$, where $\mathcal{H}_k$ is the 4×4 matrix produced by replacing $-i\partial_x \to k$ in Eq. (8.7). The excitation spectrum $E(k)$ is most

simply calculated by squaring $\mathcal{H}_k$ twice, and extracting the characteristic polynomial [132]. This procedure yields

$$E_{\pm}^2(k) = \epsilon_0^2 + \frac{2E_r\hbar^2k^2}{m} + \frac{1}{4\hbar^2\Omega^2} + \Delta^2 \pm \hbar\sqrt{\frac{8E_r\epsilon_0^2k^2}{m} + \Omega^2\epsilon_0^2 + \Omega^2\Delta^2}, \tag{8.11}$$

where $\epsilon_0 = \frac{\hbar^2k^2}{2m} - \tilde{\mu}$. The four bands $E_+(k), E_-(k), -E_-(k), -E_+(k)$, as shown in Fig. 8.4, correspond to the four eigenvectors $W^{p+}(k)$, $W^{p-}(k)$, $W^{h-}(k)$, $W^{h+}(k)$. The Hamiltonian $\mathcal{H}$ has the intrinsic symmetry, $\left\{\mathcal{H}, \tau_y\right\} = 1$. Given two eigenvectors $W^{p\pm}$ with eigenvalues $E^{\pm}$, one can always construct the other two $W^{h\pm} = i\tau_y W^{p\pm}$ with eigenvalues $-E^{\pm}$. We therefore denote,

$$W^{p+}(k) = \left(u_{k\uparrow}^+, u_{k\downarrow}^+, -v_{k\downarrow}^+, -v_{k\uparrow}^+\right)^{\mathsf{T}} \tag{8.12}$$

$$W^{p-}(k) = \left(u_{k\uparrow}^-, u_{k\downarrow}^-, -v_{k\downarrow}^-, -v_{k\uparrow}^-\right)^{\mathsf{T}} \tag{8.13}$$

$$W^{h-}(k) = \left(v_{k\downarrow}^-, v_{k\uparrow}^-, u_{k\uparrow}^-, u_{k\downarrow}^-\right)^{\mathsf{T}} \tag{8.14}$$

$$W^{h+}(k) = \left(v_{k\downarrow}^+, v_{k\uparrow}^+, u_{k\uparrow}^+, u_{k\downarrow}^+\right)^{\mathsf{T}}. \tag{8.15}$$

The unitary condition on the 4 by 4 matrix $\left(W^{p+}(k), W^{p-}(k), W^{h-}(k), W^{h+}(k)\right)$ also leads to the equalities $u_{k\downarrow}^{\pm} = \left(u_{-k\uparrow}^{\pm}\right)^*$ and $v_{k\downarrow}^{\pm} = -\left(v_{-k\uparrow}^{\pm}\right)^*$.

In Fig. 8.4, the spectrum is shown for a range of parameters. One important feature is the $k = 0$ gap $E_0 \equiv 2E_-(k = 0) \equiv 2|G|$, where $G \equiv \sqrt{\tilde{\mu}^2 + \Delta^2} - \hbar\Omega/2$. When $\Omega = 0$, the two positive energy bands touch at $k = 0$, and $E_0 > 0$. The gas is in the same universality class as a conventional s-wave superconductor. Increasing the Raman laser strength such that $0 < \hbar\Omega < 2\sqrt{\Delta^2 + \tilde{\mu}^2}$ separates the two bands and reduce E_0. At $\hbar\Omega = 2\sqrt{\Delta^2 + \tilde{\mu}^2}$, E_0 is zero, and there is a topological transition. Once $\hbar\Omega > 2\sqrt{\Delta^2 + \tilde{\mu}^2}$, E_0 is again positive, but the gas is no longer a conventional superfluid, instead it has a non-trivial topological invariant.

The relevant topological invariant is a Berry phase. Eqs. (8.12-8.15) can be

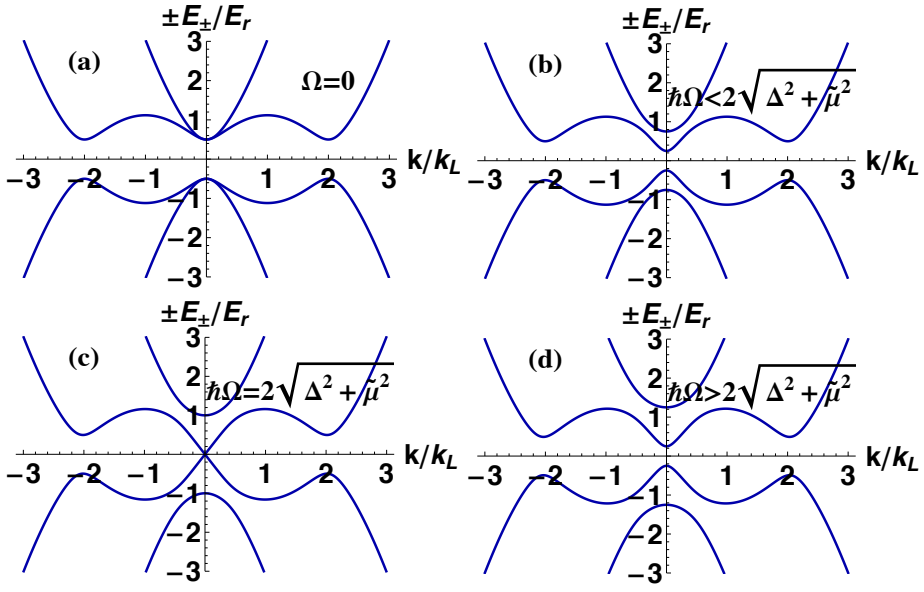

Figure 8.3: Band structure of homogeneous gas. From the top to the bottom, the four bands are $E_+, E_-, -E_-, -E_+$ respectively. The parameters are $\mu = E_r, \Delta = 0.5E_r$, and (a) $\Omega = 0$, (b) $\Omega = 0.5E_r$, (c) $\Omega = E_r$, (d) $\Omega = 1.5E_r$.

thought of as maps from the real line ($-\infty \leq k \leq \infty$) to the space of unit vectors in SU(4). One can generate a closed path by taking

$$C : W^{p+}(-\infty) \to W^{p+}(\infty) = W^{p-}(-\infty) \to W^{p-}(+\infty) \quad = W^{p+}(-\infty). \tag{8.16}$$

The equalities follow from noting that up to phases

$$W^{p+}(-\infty) \quad = \quad W^{p-}(\infty) = (0,1,0,0)^\intercal \tag{8.17}$$

$$W^{p-}(-\infty) \quad = \quad W^{p+}(\infty) = (1,0,0,0)^\intercal . \tag{8.18}$$

Given this closed path, one can define the Berry phase

$$\begin{aligned} \gamma &= i \oint_C dk\, \mathbf{W}^* \cdot \partial_k \mathbf{W} \\ &= i \int_{-\infty}^{\infty} dk\, \left(W^{p+}(k)\right)^* \cdot \partial_k W^{p+}(k) + i \int_{-\infty}^{\infty} dk\, \left(W^{p-}(k)\right)^* \cdot \partial_k W^{p-}(k). \end{aligned} \tag{8.19}$$

In the case of a gauge which is not smooth, one would instead use

$$\begin{aligned} e^{i\gamma} &= \lim_{\delta k \to 0} \left(\prod_{k=-\infty}^{\infty} \left(W^{p+}(k)\right)^* \cdot W^{p+}(k-\delta k) \times \prod_{k=-\infty}^{\infty} \left(W^{p-}(k)\right)^* \cdot W^{p-}(k-\delta k) \right) \\ &\times \left(W^{p+}(-\infty)\right)^* \cdot W^{p-}(\infty) \left(W^{p-}(-\infty)\right)^* \cdot W^{p+}(\infty). \end{aligned} \tag{8.20}$$

Since H has real valued matrix elements, $e^{i\gamma} = \pm 1$. The Berry phase γ is only well defined if the spectrum has no degeneracies. We restrict $0 \leq \gamma < 2\pi$. For $G > 0$, we find $\gamma = \pi$. For $G < 0$, $\gamma = 0$. Somewhat counter-intuitively the $\gamma = 0$ sector corresponds to the "topologically non-trivial" state analogous to a 1D spinless p-wave superconductor.

8.4 Traps

In this section we will solve the BdG equations for a trapped gas. The qualitative features of our results can be anticipated by treating the system as locally homogeneous: the properties at position x will be reminiscent of those corresponding to a homogeneous gas with chemical potential $\tilde{\mu}(x) = \tilde{\mu} - V(x)$. Within this local density approximation (LDA), one can define a function $G(x) = \sqrt{\tilde{\mu}(x) + \Delta(x)^2} - \hbar\Omega/2$, where $G(x) = 0$ corresponds to the boundaries between topologically distinct regions. One expects there will be Majorana excitations at the boundaries. We will use numerical solution of the BdG equation to explore this physics beyond the LDA. Further, in Sec. III(D) we will linearize the BdG equations about the points $G(x) = 0$, and analytically investigate these Majorana modes, without making a LDA.

8.4.1 Order parameter and density

In the presence of a trap, we write the BdG equations in real space,

$$\mathcal{H}_{trap} W_n(x) = E_n W_n(x), \tag{8.21}$$

where

$$\mathcal{H}_{trap} = \left(-\frac{\hbar^2}{2m}\partial_x^2 - \tilde{\mu} + V(x)\right)\tau_z + \frac{i\hbar^2 k_L}{m}\partial_x \tau_z \sigma_z + \frac{\hbar\Omega}{2}\tau_z\sigma_x + \Delta(x)\tau_x\sigma_z. \tag{8.22}$$

The eigenvectors $W_n(x)$ come in pairs, $W_n^p(x)$ and $W_n^h(x)$, which correspond to eigenvalues $E_n \geq 0$ and $-E_n$,

$$W_n^p(x) = (u_{n\uparrow}(x), u_{n\downarrow}(x), v_{n\downarrow}(x), v_{n\uparrow}(x))^\mathsf{T} \tag{8.23}$$

$$W_n^h(x) = \left(v_{n\uparrow}^*(x), v_{n\downarrow}^*(x), u_{n\downarrow}^*(x), u_{n\uparrow}^*(x)\right)^\mathsf{T}. \tag{8.24}$$

To make contact with our previous discussion, we note that in the spatially homogeneous case, n can be represented by a momentum k_n and a sign $\varepsilon_n = \pm$, so that $W_n^p(x) = e^{ik_n x}\left(u_{k_n\uparrow}^{\varepsilon_n}, u_{k_n\downarrow}^{\varepsilon_n}, v_{k_n\downarrow}^{\varepsilon_n}, v_{k_n\uparrow}^{\varepsilon_n}\right)^\mathsf{T}$ and $W_n^h(x) = e^{ik_n x}\left((v_{k_n\uparrow}^{\varepsilon_n})^*, (v_{k_n\downarrow}^{\varepsilon_n})^*, (u_{k_n\downarrow}^{\varepsilon_n})^*, (u_{k_n\uparrow}^{\varepsilon_n})^*\right)^\mathsf{T}$. One then recovers Eqs. (8.12)-(8.15).

Fixing $\{\tilde{\mu}, \Omega, g_{1D}\}$, we solve Eqs. (8.21) iteratively. We discretize space into n_{grid} equally spaced points, and use a finite difference method with a pseudo-spectral scheme to represent $\mathcal{H}_{trap}$ as a $4n_{\text{grid}}$ by $4n_{\text{grid}}$ matrix. In the jth iteration, we numerically diagonalize the matrix $\mathcal{H}_{trap}^{(j)}$ with the order parameter $\Delta^{(j)}(x)$. We start with a constant $\Delta^{(0)}(x) = \Delta_0$. We extract the eigenvectors $W_n^{(j)}(x)$ and calculate the order parameter $\Delta^{(j+1)}(x) = g_{1D}\sum_n \left(u_{n\downarrow}^{(j)} v_{n\uparrow}^{*(j)} \left\langle \xi_n \xi_n^\dagger \right\rangle + v_{n\downarrow}^{*(j)} u_{n\uparrow}^{(j)} \left\langle \xi_n^\dagger \xi_n \right\rangle\right)$, where ξ_n is the annihilation operator of the Bogoliubov particle. At temperature T, $\left\langle \xi_n^\dagger \xi_n \right\rangle = 1/\left(e^{E_n/k_bT} + 1\right)$. Then we diagonalize $\mathcal{H}_{trap}^{(j+1)}$ and repeat the procedure. We stop iterating when $\left|\Delta^{(j+1)}(x) - \Delta^{(j)}(x)\right|$ falls below a threshold. The final convergent order parameter $\Delta^{(N)}(x)$ is largely independent of n_{grid} and $\Delta^{(0)}(x)$ when $n_{\text{grid}} \geq 1200$. In **Appendix 8.6.1** we explore the convergence with the real space grid size n_{grid}.

The order parameters and density profiles for a gas in a harmonic trap $V(x) = \lambda\,(x/L)^2\,E_r$ are shown in Fig. 8.4, where the dimensionless parameter $\lambda = 4$ characterizes the stiffness of the trap, and $2L$ is the simulation length with $k_L L = 100$.

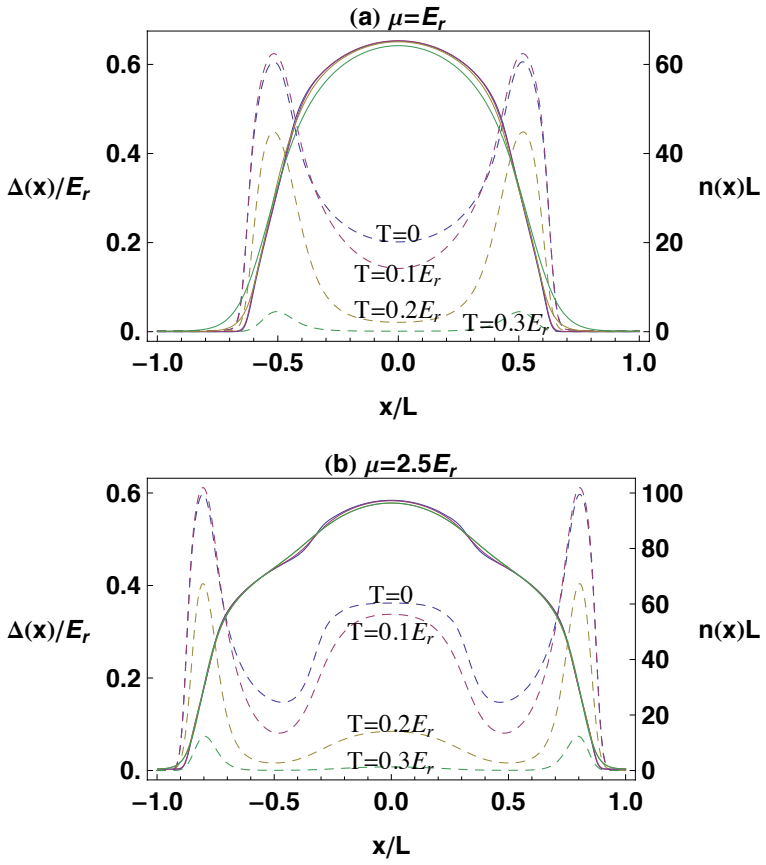

Figure 8.4: Order parameter $\Delta(x) = g_{1D} \sum_n \left(u_{n\downarrow}(x) v^*_{n\uparrow}(x) \left\langle \xi_n \xi^\dagger_n \right\rangle + v^*_{n\downarrow}(x) u_{n\uparrow}(x) \left\langle \xi^\dagger_n \xi_n \right\rangle \right)$ (dashed) and density $n(x) = \sum_{n\sigma} \left(|v_{n\sigma}(x)|^2 \left\langle \xi_n \xi^\dagger_n \right\rangle + |u_{n\sigma}(x)|^2 \left\langle \xi^\dagger_n \xi_n \right\rangle \right)$ (solid) at temperatures $T = 0, 0.1E_r, 0.2E_r, 0.3E_r$. Other parameters are $g_{1D} = -0.03E_r L, \hbar\Omega = 2E_r, \lambda = 4, k_L L = 100$, and (a) $\mu = E_r$ and (b) $\mu = 2.5E_r$.

We choose the Rabi frequency to be $\hbar\Omega = 2E_r$, and take $g_{1D} = -0.03E_r L$, corresponding to the dimensionless interaction strength $\beta = m|g_{1D}|/\hbar^2 n_0 \sim 2$, where n_0 is the central density at zero temperature. For comparisons, experiments on 1D Fermi gases at Rice have $\beta \sim 3$ [150]. If $E_r/\hbar = 50$kHz (a typical experimental value), then these parameters correspond to a trap with small oscillation frequency $\omega = 2$kHz. The order parameter has qualitatively different behavior if the center of the trap has one or two bands occupied. For relatively small chemical potential $E_r - \sqrt{(\hbar\Omega/2)^2 - \Delta(x)^2} \lesssim \mu \lesssim E_r + \sqrt{(\hbar\Omega/2)^2 - \Delta(x)^2}$, the center of the trap will be topologically non-trivial while the wings will be trivial. This

regime is illustrated in Fig. 8.4(a). The order parameter grows near the edge of the cloud. This is a feature of 1D where, due to the divergence of the low energy density of state, the interactions are stronger for lower density [151]. For $\mu \gtrsim E_r + \sqrt{(\hbar\Omega/2)^2 - \Delta(x)^2}$, the center will be topologically trivial, but there will be a band of the non-trivial state further out. Here the order parameter profile is quite rich, with a central plateau, surrounded by two valleys and two peaks. The central plateau roughly corresponds to where both bands are occupied. The order parameter is sensitive to temperature. The bulk Δ is significantly suppressed and vanishes for $T \gtrsim 0.2E_r$. The density has no notable structure and is nearly independent of temperature for $T \lesssim 0.3E_r$.

8.4.2 Density of states (DOS)

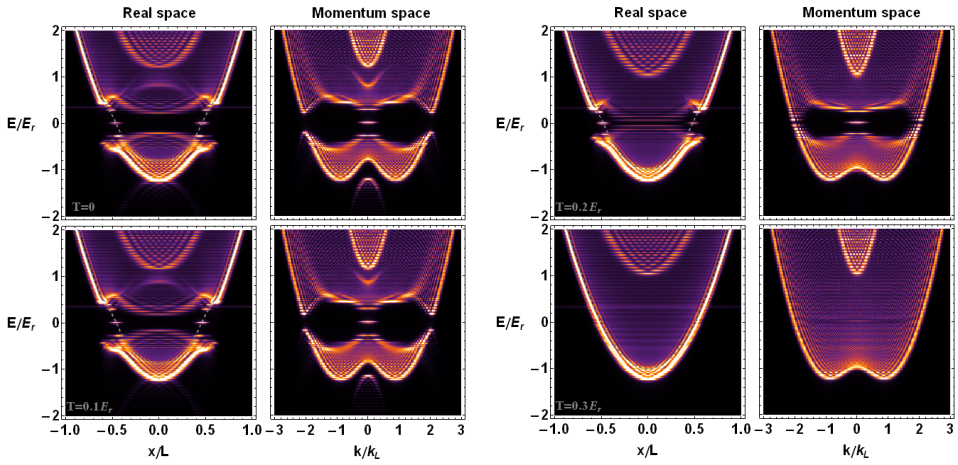

Figure 8.5: Density of states (DOS) in real space (left panel) and momentum space (right panel) at $T = 0, 0.1E_r, 0.2E_r, 0.3E_r$ from the top to the bottom, with order parameters identical to those in Fig. 8.4(a). The grey (dashed) in the left panels is plotted with $G(x) = \sqrt{\tilde{\mu}(x)^2 + \Delta(x)^2} - \hbar\Omega/2$, where the zero points of $G(x)$ pinpoint the position of MFs. The brighter color corresponds to the higher spectral weight.

The elementary excitations are encoded in the single particle Green func-

tion $G_{\sigma\sigma'}(x,t,x',t') = -i\left\langle \hat{T}\psi_\sigma(x,t)\psi^\dagger_{\sigma'}(x',t')\right\rangle$ and the associated spectral density $A_{\sigma\sigma'}(x,x',E) = -2\,\mathrm{Im}\int dt\, e^{iEt}G_{\sigma\sigma'}(x,t,x',0)$, where $\hat{T}$ is the time-ordering operator. A local tunneling experiment can measure the density of states (DOS) $\rho(E,x) = A_{\uparrow\uparrow}(x,x,E) + A_{\downarrow\downarrow}(x,x,E)$. This quantity gives the number of single particle states with energy E at position x. It can be understood as an application of Fermi's Golden rule to the response to a tunneling probe. Within our mean-field theory

$$\rho(E,x) = \sum_{\sigma=\uparrow,\downarrow}\left(\rho^h_\sigma(-E,x) + \rho^p_\sigma(E,x)\right), \tag{8.25}$$

where

$$\rho^h_\sigma(E,x) = \sum_n |v_{n\sigma}(x)|^2\,\delta(E_n - E) \tag{8.26}$$

$$\rho^p_\sigma(E,x) = \sum_n |u_{n\sigma}(x)|^2\,\delta(E_n - E). \tag{8.27}$$

We can similarly introduce a momentum resolved DOS $\rho(E,k) = \int dx\,dx' e^{ik(x-x')}$ $(A_{\uparrow\uparrow}(x,x',E) + A_{\downarrow\downarrow}(x,x',E))$, which can be measured with momentum resolved radio-frequency spectroscopy [139]. In the present case

$$\rho(E,k) = \sum_{\sigma=\uparrow,\downarrow}\left(\rho^h_\sigma(-E,k) + \rho^p_\sigma(E,k)\right), \tag{8.28}$$

where

$$\rho^h_\sigma(E,k) = \sum_n \left|\int dx\, v_{n\sigma}(x)\, e^{ikx}\right|^2 \delta(E_n - E) \tag{8.29}$$

$$\rho^p_\sigma(E,x) = \sum_n \left|\int dx\, u_{n\sigma}(x)\, e^{ikx}\right|^2 \delta(E_n - E). \tag{8.30}$$

In Figs. 8.5 and 8.6 we plot the DOS for the trapped gas with the order parameters calculated in Sec. 8.4.1. We also show a dashed curve corresponding to $G(x) = \sqrt{\tilde{\mu}(x)^2 + \Delta(x)^2} - \hbar\Omega/2$. The point where $G(x) = 0$ represents the boundary between topologically distinct regions defined in Sec. 8.3.2. For the parameters

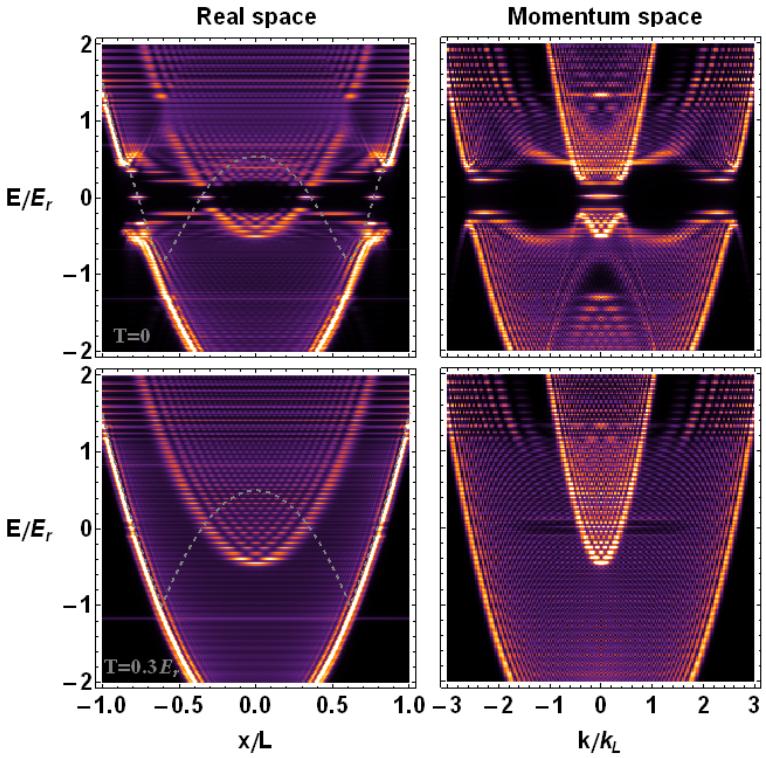

Figure 8.6: Density of states (DOS) in real space (left panel) and momentum space (right panel) at $T = 0$ and $0.3E_r$, with parameters identical to those in Fig. 8.4(b). The brighter color corresponds to the higher spectral weight.

in Fig. 8.5, $G(x) = 0$ at two locations, and we find that the BdG equations have two zero-energy modes, localized near these points. As will be discussed later, these modes may be interpreted as MFs. They are clearly spectrally separated from all other states. Fig. 8.6 shows the case where $G(x) = 0$ at four locations, representing four MFs. The right panels of Figs. 8.5 and 8.6 show the momentum space DOS. The MF modes sit in a large gap at $k = 0$.

As we have shown in Sec. 8.4.1, the order parameter decreases with temperature. In real space, the bulk Δ becomes very small at $T = 0.2E_r$, while Δ at the edges remains large: the MFs at the edges are very clear for $T \lesssim 0.2E_r$. At $T = 0.3E_r$, the order parameter is nearly zero and the gas becomes normal.

The evolution of the momentum space DOS parallels the real space DOS. As temperature is increased from $T = 0$, the gaps at large k shrink. The gap at $k = 0$ remains robust until $T = 0.3E_r$.

Finally for comparison, we plot the DOS within a LDA. As illustrated in Fig. 8.7, the LDA prediction for the DOS is qualitatively similar to the BdG result. The main difference is that the LDA misses physics related to quantization. In particular, the zero energy modes are not spectrally isolated in the LDA. They are, however, still located at roughly the same place in space.

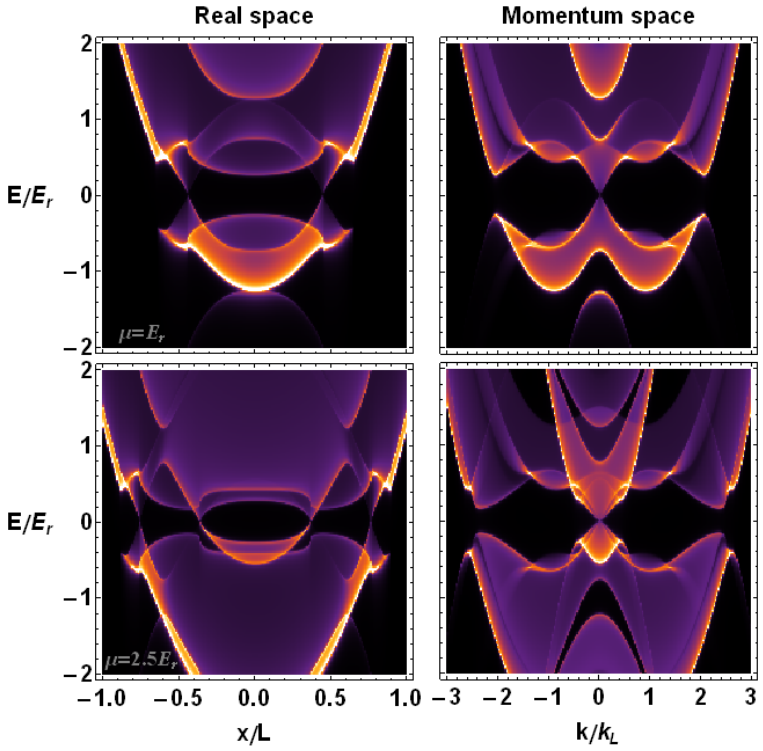

Figure 8.7: Density of states (DOS) at zero temperature under the local density approximation (LDA). The parameters are identical to those in Fig. 8.4, except $\Delta(x)$ is calculated within the LDA. The brighter color corresponds to the higher spectral weight.

8.4.3 Majorana fermions (MFs)

Here we explore the structure of the zero-energy states seen in Fig. 8.5. From our numerical solutions to the BdG equations, we have two wavefunctions

$$W_0^p(x) = e^{i\varphi_1'}\left(u_{0\uparrow}(x), u_{0\downarrow}(x), v_{0\downarrow}(x), v_{0\uparrow}(x)\right)^{\mathsf{T}} \tag{8.31}$$

$$W_0^h(x) = e^{i\varphi_2'}\left(v_{0\uparrow}^*(x), v_{0\downarrow}^*(x), u_{0\downarrow}^*(x), u_{0\uparrow}^*(x)\right)^{\mathsf{T}}, \tag{8.32}$$

which define operators

$$\xi_0 = \int dx \left(W_0^p(x)\right)^\dagger \cdot \tilde{\Psi}(x) \tag{8.33}$$

$$\xi_0^\dagger = e^{i(\varphi_2'-\varphi_1')} \int dx \left(W_0^h(x)\right)^\dagger \cdot \tilde{\Psi}(x), \tag{8.34}$$

and obey $\mathcal{H}_{trap} W_0^p(x) \approx \mathcal{H}_{trap} W_0^h(x) \approx 0$. The phases φ_1' and φ_2' are not unique, and the factor in Eq. (8.31) must be introduced to make $\xi_0^\dagger$ conjugate to ξ_0. By construction these are fermionic operators $\left\{\xi_0, \xi_0^\dagger\right\} = 1$.

As zero-energy solutions to the BdG equations, both ξ_0 and $\xi_0^\dagger$ commute with H. Hence the ground state is degenerate: $\xi_0 |GS_1\rangle = 0$ and $|GS_2\rangle = \xi_0^\dagger |GS_1\rangle$. These two degenerate states can be used as a qubit for quantum information processing [123].

The operator $\xi_0^\dagger$ which couples $|GS_1\rangle$ to $|GS_2\rangle$ is intrinsically nonlocal, with weight at two spatially separated points. One can however introduce operators

$$\chi_0 = \frac{1}{\sqrt{2}} e^{i\varphi}\left(\xi_0 + e^{-2i\varphi}\xi_0^\dagger\right) = \int dx\, f_0^\dagger(x) \cdot \tilde{\Psi}(x) \tag{8.35}$$

$$\bar{\chi}_0 = \pm\frac{1}{\sqrt{2}i} e^{i\varphi}\left(\xi_0 - e^{-2i\varphi}\xi_0^\dagger\right) = \int dx\, \bar{f}_0^\dagger(x) \cdot \tilde{\Psi}(x) \tag{8.36}$$

where

$$f_0(x) = \frac{1}{\sqrt{2}} e^{i\varphi_1}\left(W_0^p(x) + e^{-i\varphi_2} W_0^h(x)\right) \tag{8.37}$$

$$\bar{f}_0(x) = \pm\frac{1}{\sqrt{2}i} e^{i\varphi_1}\left(W_0^p(x) - e^{-i\varphi_2} W_0^h(x)\right), \tag{8.38}$$

with arbitrary phases $\varphi_1 = \varphi - \varphi_1'$ and $\varphi_2 = 2\varphi - \varphi_1' + \varphi_2'$. By choosing the appropriate φ_2, these operators can be made local. In particular if $G(x) = 0$ at $x = x_1, x_2$, then $f_0(x)$ can be chosen to be nonzero only near x_1, and $\bar{f}_0(x)$ only near x_2.

The operators χ_0 and $\bar{\chi}_0$ obey the Majorana algebra: $\chi_0^\dagger = \chi_0, \bar{\chi}_0^\dagger = \bar{\chi}_0$, $\{\chi_0, \bar{\chi}_0\} = 0$, $\{\chi_0, \chi_0\} = \{\bar{\chi}_0, \bar{\chi}_0\} = 1$. They commute with the Hamiltonian.

Note, as we will use in the next subsection, $f_0(x) \equiv e^{i\varphi_f}\left(u_{f\uparrow}(x), u_{f\downarrow}(x), v_{f\downarrow}(x), v_{f\uparrow}(x)\right)$ obeys the BdG equations, but the resulting Bogoliubov transformation is not unitary as it changes the commutation relations. Since $\chi_0 = \chi_0^\dagger$, we have $u_{f\sigma}(x) = e^{-2i\varphi_f} v_{f\sigma}^*(x)$. For smaller systems, coupling between these modes push them away from $E_0 = 0$.

8.4.4 Eigen-energies of excited states near a MF

As seen in Figs. 8.5-8.6, the MFs are localized in real space and momentum space. Thus we can calculate their properties by linearizing the trap around their locations in position space, and linearizing momentum around $k = 0$. As previously discussed, the locations of the MFs can be found via the LDA. There are generally four MFs, localized at $x_m = \pm L\sqrt{R_{\pm m}/\lambda E_r}$, where $R_{\pm m} \equiv \tilde{\mu} \pm \sqrt{\hbar^2\Omega^2/4 - \Delta_m^2}$, with $\Delta_m \equiv \Delta(x = x_m)$. We restrict ourselves to the location of one MF, $x_m = L\sqrt{R_{+m}/\lambda E_r}$. We write the linearized BdG Hamiltonian as the sum of two terms $\mathcal{H}_{lin} = \mathcal{H}_0 + \mathcal{H}_i$,

$$\mathcal{H}_0 = \frac{\hbar\Omega}{2}\tau_z\sigma_x + \Delta_m\tau_x + \sqrt{\hbar^2\Omega^2/4 - \Delta_m^2}\tau_x\sigma_z \tag{8.39}$$

$$\mathcal{H}_i = \tilde{\lambda}(x - x_m)\tau_z - \kappa\tau_z\sigma_z, \tag{8.40}$$

where $\tilde{\lambda} = 2\lambda x_m E_r/L^2$ and $\kappa = \hbar^2 k_L k/m$. The "interaction" term $\mathcal{H}_i$ can be treated as a perturbation, and it vanishes as $x \to x_m, k \to 0$. In the absence of perturbations, $\mathcal{H}_{lin} = \mathcal{H}_0$ has two degenerate zero-energy states

$$\mathcal{D}_1 = \frac{\sqrt{2}}{2}(\sin\phi, -\cos\phi, -\cos\phi, \sin\phi) \tag{8.41}$$

$$\mathcal{D}_2 = \frac{\sqrt{2}}{2}(-\cos\phi, \sin\phi, -\sin\phi, \cos\phi), \tag{8.42}$$

where $\sin\phi = \sqrt{(\hbar\Omega/2 + \Delta_m)/\hbar\Omega}$. Following the standard approach to first-order degenerate perturbation theory, we diagonalize the Hamiltonian projected into the subspace $\{\mathcal{D}_1, \mathcal{D}_2\}$,

$$\mathscr{H}_{lin} = \begin{pmatrix} \mathcal{D}_1 \\ \mathcal{D}_2 \end{pmatrix} H_{lin}(\mathcal{D}_1, \mathcal{D}_2) = K\bar{\sigma}_z + X\bar{\sigma}_x, \tag{8.43}$$

where $K = -2\hbar\Delta_m k_L k/m\Omega$ and $X = -4\lambda E_r x_m(x - x_m)R_{+m}/\hbar\Omega L^2$. The Pauli matrices $\bar{\sigma}$ operate in the subspace $\{\mathcal{D}_1, \mathcal{D}_2\}$. Noting that $[X, K] = iC$ with $C = 16\sqrt{\lambda}E_r^{3/2}R_{+m}^{3/2}\Delta_m/\hbar^2\Omega^2 k_L L$, one can define the operators $a = \frac{K-iX}{\sqrt{2C}}, a^\dagger = \frac{K+iX}{\sqrt{2C}}$ that satisfy $\left[a, a^\dagger\right] = 1$. The eigen-equations of $\mathscr{H}_{lin}$ then become

$$\frac{\sqrt{2C}}{2}\begin{pmatrix} -\left(a^\dagger + a\right) & i\left(a^\dagger - a\right) \\ i\left(a^\dagger - a\right) & a^\dagger + a \end{pmatrix}\begin{pmatrix} \bar{u}_n \\ \bar{v}_n \end{pmatrix} = \bar{E}_n \begin{pmatrix} \bar{u}_n \\ \bar{v}_n \end{pmatrix} \tag{8.44}$$

where $\bar{u}_n = \mathcal{D}_1 \cdot W_n, \bar{v}_n = \mathcal{D}_2 \cdot W_n$. Combining $\bar{u}_n, \bar{v}_n$ gives the equations

$$-\sqrt{2C}\begin{pmatrix} 0 & a^\dagger \\ a & 0 \end{pmatrix}\begin{pmatrix} \bar{u}_n + i\bar{v}_n \\ \bar{u}_n - i\bar{v}_n \end{pmatrix} = \bar{E}_n \begin{pmatrix} \bar{u}_n + i\bar{v}_n \\ \bar{u}_n - i\bar{v}_n \end{pmatrix}. \tag{8.45}$$

Squaring Eq. (8.45) yields harmonic oscillator Hamiltonian, and allows one to read off

$$\bar{E}_n = \pm\sqrt{2C}\sqrt{n} \quad (n = 0, 1, 2, ...). \tag{8.46}$$

Not only is there a zero-energy mode $\bar{E}_0 = 0$ (the Majorana mode), but there is a ladder of localized fermionic modes, whose energy spacing is proportional

to $\lambda^{1/4}$, and whose wavefunction components are excited harmonic oscillator states. For a homogeneous gas where $\lambda = 0$, the energy spacing becomes zero.

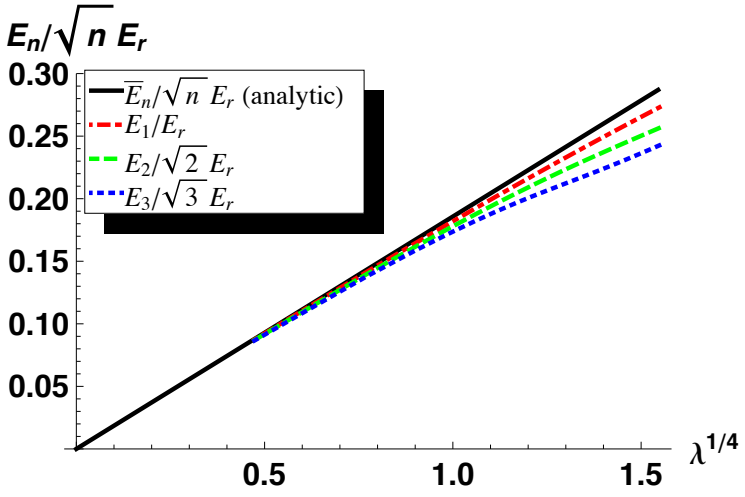

Figure 8.8: The gap between the MF state and excited states as a function of trap stiffness $\lambda^{1/4}$: the trapping potential is $V(x) = \lambda(x/L)^2 E_r$. The black (thick) curve is plotted based on the analytic Eq. (8.46). The red (dot-dashed), green (dashed), blue (dotted) curves are the energy levels E_1/E_r, $E_2/\sqrt{2}E_r$, $E_3/\sqrt{3}E_r$ respectively. They are numerically calculated from Eq. (8.21) with the parameters identical to the thick curve.

In Fig. 8.8, we plot $\bar{E}_n/\sqrt{n}E_r$ as a function of $\lambda^{1/4}$ (black thick curve) based on Eq. (8.46), and compare to the numerical results calculated from Eq. (8.21). The dot-dashed (red), dashed (green), and dotted (blue) curves show the energy levels of the first three excited states. We see the analytic results agree well with the numerics for small λ. For larger λ, the corrections to Eq. (8.21) are important, and the discrepancy between the analytic and numerical results becomes notable, especially for larger n.

At $n = 0$ ($\bar{E}_0 = 0$), the zero-energy mode has wavefunction

$$\bar{u}(x) = \frac{1}{2\sigma\sqrt{\pi}} e^{-(x-x_m)^2/2\sigma^2} \tag{8.47}$$

$$\bar{v}(x) = \frac{1}{2i\sigma\sqrt{\pi}} e^{-(x-x_m)^2/2\sigma^2}, \tag{8.48}$$

where the width $\sigma = \sqrt{\Delta_m L E_r^{1/2} / R_{+m}^{3/2} k_L \lambda^{1/2}}$ is proportional to $\lambda^{-1/4}$.

8.5 Summary

We have investigated a (pseudo) spin-1/2 spin-orbit (SO) coupled Fermi gas in a one dimensional geometry. We first relate this system to a one-band model with p-wave interactions. We then described the band structure and calculated the Berry phase γ of the full two-band model. We found γ distinguishes two topologically distinct sectors, with $\gamma = \pi$ corresponding to a conventional superconductor. By self-consistently solving the Bogoliubov-de Gennes equations and calculating both the position resolved and momentum resolved density of states, we visualized the Majorana fermion (MF) states in real and momentum space at finite temperatures. These spectra can be probed using the position resolved or momentum resolved radio-frequency spectroscopy [139, 152]. We introduced MF operators and constructed the localized MF states. We further linearized the trap near the location of a MF, finding an analytic expression for the localized MF wavefunction and the gap between the MF state and other edge states.

This physics can be experimentally studied in a bundle of weakly coupled tubes containing fermionic atoms [150]. By applying appropriate Raman lasers to these quasi-1D tubes [138, 139], one can produce an array of quasi-1D SO coupled Fermi clouds. Our calculations show that the MFs can be observed in such settings.

There are, however, significant experimental challenges. Most notably, the

Raman induced SO coupling relies on the ability of optical photons to flip the atomic hyperfine spin. As Spielman argues [4], if the Raman lasers are detuned by a frequency Δ from an excited state multiplet (and $\hbar\Delta$ is large compared to the fine structure splitting A_f), then the coupling strength Ω scales as $1/\Delta^2$. (This is contrasted with typical AC stark shifts, which instead scale as $1/\Delta$. The extra suppression is due to quantum interference between the amplitudes arising from different intermediate states.) The rate of inelastic light scattering Γ_i also scales as $1/\Delta^2$. The ratio $\upsilon = \Gamma_i/\Omega$ is therefore roughly independent of detuning. In terms of microscopic parameters, $\upsilon \propto \hbar/A_f\tau$, where τ is the lifetime of the excited states. For ^{6}Li, $\hbar/A_f\tau \sim 5.8 \times 10^{-4}$, for ^{40}K, $\hbar/A_f\tau \sim 3.5 \times 10^{-6}$ and for ^{87}Rb, $\hbar/A_f\tau \sim 8.3 \times 10^{-7}$. One sees ^{40}K has a much longer lifetime than ^{6}Li in a SO coupled Fermi experiment. The situation is even less favorable at the typical magnetic field $\sim$ 830G [153] where one encounters Feshbach resonances in ^{6}Li. The large magnetic field decouples the electron spin and the nuclear spin, and the relevant hyperfine states effectively only differ by their nuclear spin. As a result, the Raman laser couplings vanish between these states. However for ^{40}K, the typical resonance field $\sim$ 200G [154] is much smaller, and the relevant hyperfine states have larger Raman couplings. We therefore expect ^{40}K is a promising candidate for producing an interacting SO coupled Fermi gas.

8.6 Appendix

8.6.1 Convergence with grid spacing

In this Appendix, we explore the convergence of our self-consistent calculations with the grid spacing $\delta x = 2L/n_{\text{grid}}$. We show how the energy and the order parameter for a zero-temperature homogeneous gas in a box of size $2L$ with periodic boundary conditions depends on n_{grid}.

Within our mean-field theory, the energy of this homogeneous gas is

$$E_g = \sum_k \left(\epsilon_0(k) - \frac{1}{2}\left(E_+(k) + E_-(k)\right) \right) - \frac{|\Delta|^2}{\tilde{g}_{1D}}, \tag{8.49}$$

where $\tilde{g}_{1D} = g_{1D}/2L, \epsilon_0(k) = \frac{\hbar^2 k^2}{2m} - \tilde{\mu}$, and $E_\pm(k)$ is the excitation spectrum given in Eq. (8.11). The summation index k is discretized as $k = -\frac{n_{\text{grid}}}{2L}\pi, -\left(\frac{n_{\text{grid}}-2}{2L}\right)\pi, ..., \left(\frac{n_{\text{grid}}-4}{2L}\right)\pi, \left(\frac{n_{\text{grid}}-2}{2L}\right)\pi$, and Eq. (8.49) can be calculated numerically.

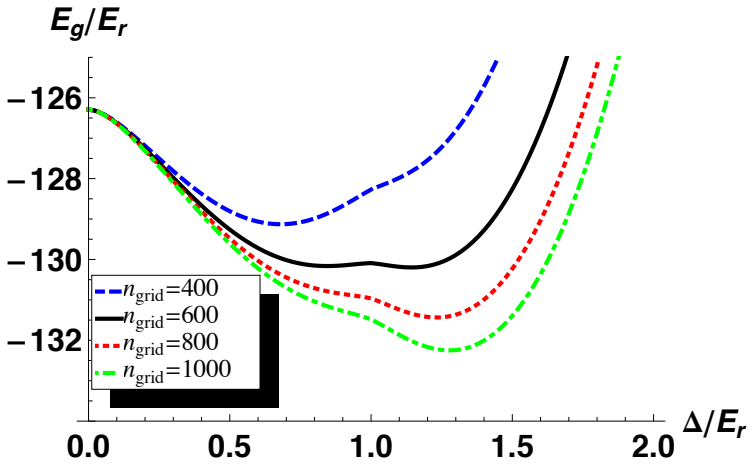

Figure 8.9: Ground state energy E_g/E_r versus order parameter Δ/E_r. The curves in blue (dashed), black (thick), red (dotted), and green (dot-dashed) correspond to $n_{\text{grid}} = 400$, 600, 800, and 1000 respectively. Other parameters are $\tilde{g}_{1D} = -0.02E_r, \hbar\Omega = 2E_r, \lambda = 0, k_L L = 100, \mu = E_r$.

Fig. 8.9 shows E_g as a function of Δ for $n_{\text{grid}} = 400, 600, 800, 1000$. We find non-trivial behavior at intermediate n_{grid}. In particular, for these parameters and $n_{\text{grid}} = 600$, the energy has two local minima, and the gap equations has four solutions, corresponding $\Delta = 0$ and other three stationary points. Such behavior is an artifact of the discretization, as it goes away for $n_{\text{grid}} \gtrsim 800$. It does, however, indicate that in the presence of an appropriate tuned optical lattice, there will be metastable superfluid states.

In Fig. 8.10, we show how the order parameter Δ depends on n_{grid}. We calculate Δ by minimizing E_g,

$$\left.\frac{\partial E_g}{\partial |\Delta|}\right|_{|\Delta|>0} = 0. \tag{8.50}$$

We see Δ converges to a finite value as $n_{\text{grid}} \to \infty$. For the simulation size $n_{\text{grid}} = 1200$ used in the main text, the finite grid error is $\frac{|\Delta(n_{\text{grid}}=\infty)-\Delta(n_{\text{grid}}=1200)|}{\Delta(n_{\text{grid}}=\infty)} \leq 12\%$.

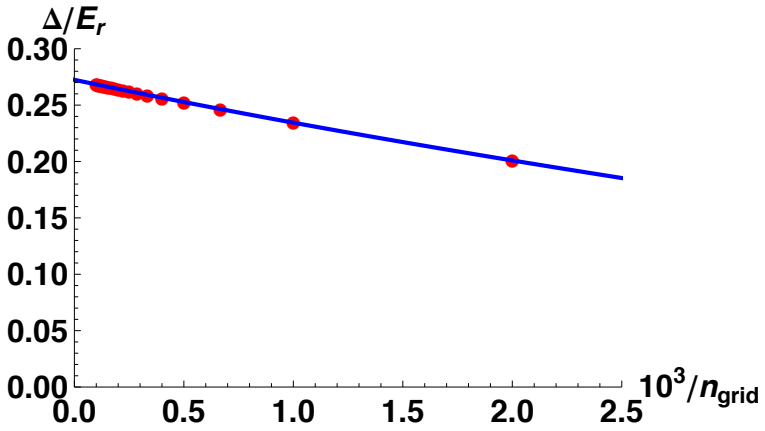

Figure 8.10: Order parameter Δ/E_r versus $10^3/n_{\text{grid}}$. The red dots are calculated from Eq. (8.50). The blue (thick) curve is an extrapolation. The parameters here are identical to those in Fig. 8.4(a) except for $\lambda = 0$.

CHAPTER 9

MAGNETIC FIELD DEPENDENCE OF RAMAN COUPLING IN ALKALI ATOMS

This chapter was adapted from "Magnetic-field dependence of Raman coupling in alkali-metal atoms" by Ran Wei and Erich J. Mueller, published in Physical Review A 87, 042514 (2013).

9.1 Abstract

We calculate the magnetic field dependence of Rabi rates for two-photon optical Raman processes in alkali atoms. Due to a decoupling of the nuclear and electronic spins, these rates fall with increasing field. At the typical magnetic fields of alkali atom Feshbach resonances ($B \sim$ 200G$-$1200G), the Raman rates have the same order of magnitude as their zero field values, suggesting one can combine Raman-induced gauge fields or spin-orbit coupling with strong Feshbach-induced interactions. The exception is ^{6}Li, where there is a factor of 7 suppression in the Raman coupling, compared to its already small zero-field value.

9.2 Introduction

Two-photon "Raman" transitions act as an important control parameter in cold atom experiments. These optical transitions couple motional and internal degrees of freedom, mimicking important physical processes such as gauge fields [1, 12] and spin-orbit coupling [6, 138, 139, 155]. They have also been used

as spectroscopic probes, for example allowing scientists to measure excitation spectra [138, 156, 157]. The most exciting future applications of these techniques will involve strongly interacting atoms near Feshbach resonances [144, 158, 159, 160, 161, 162, 163, 164, 165, 166]. Here we study the Raman couplings as a function of magnetic field, quantifying the practicality of such experiments. We find that for relatively heavy atoms, such as ^{40}K, the Raman techniques are compatible with the magnetic fields needed for Feshbach resonances. Despite important experimental demonstrations [139], lighter atoms, such as ^{6}Li are less promising, as the ratio of Raman Rabi frequency to the inelastic scattering rate is not sufficiently large. This problem is exacerbated by the magnetic field.

We are interested in two-photon transitions which take an atom between two hyperfine states $|g_1\rangle$ and $|g_2\rangle$. Optical photons only couple to electronic motion in an atom. Hence such Raman transitions rely on fine and hyperfine interactions. The former couple electronic spins and motion, and the latter couple nuclear spins to the electronic angular momentum. One expects that magnetic fields will reduce these Raman matrix elements, as the disparate Zeeman coupling of electronic and nuclear degrees of freedom competes with the fine and hyperfine interactions. We find that at the typical magnetic fields of Feshbach resonance ($B \sim$ 200G$-$1200G [65]), the Raman couplings are still quite strong. The exception is ^{6}Li, where there is a factor of 7 suppression, compared to its already small zero-field value.

A key figure of merit in experiment is the ratio of the Raman Rabi frequency to the inelastic scattering rate $\beta \equiv \Omega_R/\Gamma_{\text{ine}}$. The inverse Rabi frequency gives the time required for an atom to flip between $|g_1\rangle$ and $|g_2\rangle$, and the inverse inelastic scattering rate gives the average time between photon absorption events,

which leads to heating. For equilibrium experiments on Raman-dressed atoms, one needs $\Omega_R \sim \mu/\hbar \sim$ kHz, where μ is the chemical potential. A typical experiment takes one second. Thus if $\beta \lesssim 10^3$, the inelastic light scattering has a large impact. As argued by Spielman [4], both of these rates at sufficiently large detuning limit are proportional to the laser intensity and inversely proportional to the square of the detuning. We numerically calculate this ratio as a function of magnetic field, including all relevant single-particle physics. We also explore the detuning dependence of this ratio.

The remainder of this chapter is organized as follows. In Sec. II, we estimate the ratio of the Raman Rabi frequency to the inelastic scattering rate in the absence of magnetic field for various alkali atoms. In Sec. III, we calculate the magnetic field dependence of electric dipole transitions: We introduce the single-particle Hamiltonian in Sec. III(A), and in Sec. III(B) we introduce the formal expression of the electric dipole transitions. The analytical discussions and numerical results are elaborated in Sec. III(C) and Sec. III(D). In Sec. IV, we calculate the ratios for ^{23}Na, ^{40}K, ^{85}Rb, ^{87}Rb and ^{133}Cs, and further study ^{6}Li and explore how the ratio depends on detuning. Finally we conclude in Sec. V.

9.3 Raman coupling

We consider a typical setup of a Raman experiment, as shown in Fig. 9.1: Two hyperfine ground states $|g_1\rangle$ and $|g_2\rangle$ with energies E_g, are coupled to a pair of excited multiplets $\left\{|e_\mu\rangle, |e_\nu\rangle\right\}$ by two lasers, where the coupling strengths are characterized by the Rabi frequencies Ω_1 and Ω_2. The states $|e_\mu\rangle$ and $|e_\nu\rangle$ are states in the $J = 1/2$ and $J = 3/2$ manifolds, with energies E_μ and E_ν, and the energy

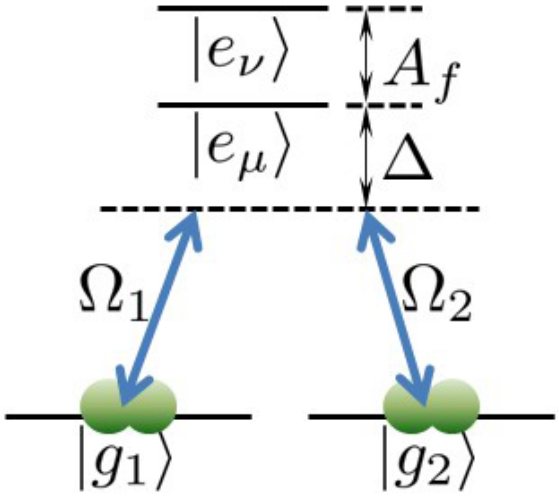

Figure 9.1: Sketch of the energy level structures in a Raman experiment. The Rabi frequencies Ω_1, Ω_2 characterize the coupling strengths between the ground states $|g_1\rangle, |g_2\rangle$ and the excited states. The fine structure energy splitting between $|e_\mu\rangle$ and $|e_\nu\rangle$ is $A_f = E_\nu - E_\mu$. The laser detuning is $\Delta = \left(E_\mu - E_g\right) - \hbar\omega$.

difference $A_f = E_\nu - E_\mu$. For ^{6}Li, $A_f \sim (2\pi\hbar) \times 10$GHz. For heavier atoms such as ^{40}K, $A_f \sim (2\pi\hbar) \times 1$THz. The laser detuning $\Delta = \left(E_\mu - E_g\right) - \hbar\omega$, characterizes the energy mismatch between the laser frequency $f = \omega/2\pi$ and the atomic D1 transition.

Within such a setup, the two lasers couple $|g_1\rangle$ and $|g_2\rangle$ via two-photon transitions, and the Raman Rabi frequency, which characterizes the (Raman) coupling strength, is

$$\Omega_R = \sum_\mu \frac{\hbar\Omega_{1\mu}\Omega_{2\mu}}{4\Delta} + \sum_\nu \frac{\hbar\Omega_{1\nu}\Omega_{2\nu}}{4\left(\Delta + A_f\right)}, \tag{9.1}$$

where the optical Rabi frequency $\Omega_{i\epsilon} = \boldsymbol{E}_i \cdot \langle g_i|\boldsymbol{d}|e_\epsilon\rangle / \hbar$ with electronic dipole $\boldsymbol{d} = e\boldsymbol{r}$, characterizes the individual transition element between the ground state $|g_i\rangle$ and the excited state $|e_\epsilon\rangle$ ($i = 1, 2$ and $\epsilon = \mu, \nu$). In our following calculations, we assume $|g_1\rangle$ and $|g_2\rangle$ are the lowest two ground states.

This expression can be simplified by noting that the ground state quadrupole

matrix element $\left\langle g_i|d_a d_b|g_j\right\rangle = 0$ unless $i = j$ and $a = b$ ($a, b = x, y, z$). This reflects the spherical symmetry of the electron wavefunction, and the fact that the electronic dipole does not couple to spin. Inserting a complete set of exited states, we find $\sum_\mu \Omega_{1\mu}\Omega_{2\mu} + \sum_\nu \Omega_{1\nu}\Omega_{2\nu} = 0$, allowing us to write Eq. (9.1) solely in terms of the matrix elements for the D1 line,

$$\Omega_R = \frac{\hbar A_f}{4\Delta\left(\Delta + A_f\right)} \sum_\mu \Omega_{1\mu}\Omega_{2\mu}. \tag{9.2}$$

It is thus clear that $\Omega_R \sim A_f/\Delta^2$ for $\Delta \gg A_f$. The inelastic scattering rate that emerges from the spontaneous emission of the excited states is

$$\Gamma_{\text{ine}} = \gamma\left(\sum_\mu \frac{\hbar^2\left(\Omega_{1\mu}^2 + \Omega_{2\mu}^2\right)}{4\Delta^2} + \sum_\nu \frac{\hbar^2\left(\Omega_{1\nu}^2 + \Omega_{2\nu}^2\right)}{4\left(\Delta + A_f\right)^2}\right) \tag{9.3}$$

where γ denotes the decay rate of these excited states. For $\Delta \gg A_f$, this rate scales as $\Gamma_{\text{ine}} \sim \gamma/\Delta^2$. Explicit calculations show that to a good approximation $\beta \equiv \Omega_R/\Gamma_{\text{ine}} \approx \beta_e \equiv A_f/12\hbar\gamma$ for $\Delta \gg A_f$. The factor of $\frac{1}{12}$ can crudely be related to cancellation of terms of opposite signs in the expression for Ω_R. As an illustration, we show A_f, γ, and β_e for various alkali atoms in Tab. I. We also present results of our numerical calculation of β. The details of this calculation will be given in Sec. III.

Alkalis	^{6}Li($2p$)	^{6}Li($3p$)	^{23}Na	^{40}K	^{85}Rb	^{87}Rb	^{133}Cs
$A_f/(2\pi\hbar)$GHz	10.0	2.88	515	1730	7120	7120	16600
$\gamma/(2\pi)$MHz	5.87	0.754	9.76	6.04	5.75	5.75	4.57
$\beta_e/10^3$	0.14	0.32	4.4	24	103	103	303
$\beta/10^3$	0.13	0.30	4.0	23	101	103	304

Table 9.1: Fine structure energy splitting A_f, spontaneous decay rate γ, and ratios β_e and β for various alkali atoms. For ^{6}Li, we consider either $2p$ states or $3p$ states as the excited multiplet. For other atoms, we consider the lowest p multiplet. The ground states for all alkali atoms are the two lowest magnetic substates. Data in the first two rows were extracted from archived data [167].

As seen from the table, the heavier atoms have more favorable ratios ($\beta \gtrsim 10^3$

for most alkali atoms). For ^{6}Li we include the rates for Raman lasers detuned from the $2s - 2p$ line and the narrower $2s - 3p$ line. For all other atoms we just consider the lowest energy $s - p$ transition. We see that the ratio for ^{6}Li can be improved by a factor of 2.2 by using the $3p$ states. Similar gains are found for laser cooling schemes using these states [168].

9.4 Magnetic field dependence of electric dipole transitions

In this section we will calculate $\Omega_{i\epsilon}$ and its dependence on the magnetic field. In the following section we will use these results to calculate Ω_R and Γ_{ine}.

9.4.1 Single-particle Hamiltonian

Fixing the principle quantum number of the valence electron, the fine and hyperfine atomic structure of an alkali in a magnetic field is described by a coupled spin Hamiltonian

$$H = H_a + H_B \tag{9.4}$$

where

$$H_a = c_f \boldsymbol{L}\cdot\boldsymbol{S} + c_{hf1}\boldsymbol{L}\cdot\boldsymbol{I} + c_{hf2}\boldsymbol{S}\cdot\boldsymbol{I} \tag{9.5}$$

$$H_B = \mu_B (g_L \boldsymbol{L} + g_S \boldsymbol{S} + g_I \boldsymbol{I})\cdot\boldsymbol{B}. \tag{9.6}$$

Here the vectors $\boldsymbol{L}$ and $\boldsymbol{S}$ are the dimensionless orbital and spin angular momentum of the electron, and $\boldsymbol{I}$ is the angular momentum of the nuclear spin. The coefficients c_f and c_{hf1}, c_{hf2} are the fine structure constant and hyperfine

structure constants, which were measured in experiments [167, 169]. μ_B is the Bohr magneton and g_L, g_S, g_I are the Lande g-factors.

For ^{6}Li, the Zeeman splitting energy is $E_B \sim (2\pi\hbar) \times 5\text{GHz}$ at the magnetic field of the wide Feshbach resonance $B = 834\text{G}$ [65]. This splitting is comparable to the fine structure constant $c_f \sim (2\pi\hbar) \times 7\text{GHz}$. For other heavier atoms where $E_B \ll c_f \sim (2\pi\hbar) \times 1\text{THz}$, the fine structure interaction is robust against the magnetic field, and we can appropriate the Hamiltonian as

$$H = c_{hf} \boldsymbol{J} \cdot \boldsymbol{I} + \mu_B (g_J \boldsymbol{J} + g_I \boldsymbol{I}) \cdot \boldsymbol{B} \tag{9.7}$$

with the vector $\boldsymbol{J} = \boldsymbol{L} + \boldsymbol{S}$.

The Hamiltonian (9.4) can be diagonalized in the basis $|Lm_L m_S m_I\rangle$, where $\{m_L, m_S, m_I\}$ are the z-components of $\{L, S, I\}$, and the eigenstate $|LQ\rangle$ can be expanded as

$$|LQ\rangle = \sum_{m_L m_S m_I} C^Q_{m_L m_S m_I} |Lm_L m_S m_I\rangle \tag{9.8}$$

where Q labels the eigenstate, and $C^Q_{m_L m_S m_I}$ corresponds to the eigenvector. We will use these coefficients to calculate the electric dipole transition in the following subsections.

9.4.2 Formal expressions

We define $D_q \equiv \langle Lm_L m_S m_I | e r_q | L' m'_L m'_S m'_I \rangle$, the electric dipole transition between $|Lm_L m_S m_I\rangle$ and $|L' m'_L m'_S m'_I\rangle$, where r_q is the position operator, expressed as an irreducible spherical tensor: $q = -1, 0, 1$ correspond to σ^-, π, σ^+ polarized light. Note that the electric dipole er_q does not directly couple to the electric spin m_S

or the nuclear spin m_I, and D_q is of the form $D_q = \delta_{m_S m'_S}\delta_{m_I m'_I}\langle Lm_L|er_q|L'm'_L\rangle$. Using the Wigner-Eckart theorem, we obtain

$$D_q = \delta_{m_S m'_S}\delta_{m_I m'_I} W^{L'L}_{m'_L q m_L}\langle L||er||L'\rangle \tag{9.9}$$

where $\langle L||er||L'\rangle$ is the reduced matrix element, independent of $\{m_L, m_S, m_I\}$. The coefficient $W^{L'L}_{m'_L q m_L}$ can be written in terms of the Wigner 3-j symbol [170]

$$W^{L'L}_{m'_L q m_L} = (-1)^{L'-1+m_L}\sqrt{2L+1}\begin{pmatrix} L' & 1 & L \\ m'_L & q & -m_L \end{pmatrix} \tag{9.10}$$

Combining Eq. (9.8) and Eq. (9.9), we obtain the electric dipole transition between two eigenstates $|LQ\rangle$ and $|L'Q'\rangle$,

$$D^{L'Q'}_{q,LQ} \equiv \langle LQ|er_q|L'Q'\rangle = \sum_{\bar{m}_L\bar{m}'_L\bar{m}_S\bar{m}_I} C^{Q}_{\bar{m}_L\bar{m}_S\bar{m}_I} C^{Q'}_{\bar{m}'_L\bar{m}_S\bar{m}_I} W^{L'L}_{\bar{m}'_L q\bar{m}_L}\langle L||er||L'\rangle \tag{9.11}$$

where the coefficients $C^{Q}_{\bar{m}_L\bar{m}_S\bar{m}_I}$ are defined by Eq. (9.8).

9.4.3 Analytical discussions

While $C^{Q}_{\bar{m}_L\bar{m}_S\bar{m}_I}$ can be numerically calculated by extracting the eigenvector of the Hamiltonian, in some regimes the problem simplifies, and $C^{Q}_{\bar{m}_L\bar{m}_S\bar{m}_I}$ corresponds to a Clebsch-Gordan coefficient. In this subsection we discuss these simple limits.

In a weak magnetic field such that the Zeeman splitting energy $E_B \ll c_{hf}$, the electronic angular momentum and the nuclear spins are strongly mixed. Here Q corresponds to the three quantum numbers $\{J, F, m_F\}$, where F is the quantum number associated with the total hyperfine spin $\boldsymbol{F} = \boldsymbol{J} + \boldsymbol{I}$, and m_F labels the magnetic sublevels. In this limit $C^{Q}_{\bar{m}_L\bar{m}_S\bar{m}_I} = C^{JFm_F}_{\bar{m}_L\bar{m}_S\bar{m}_I} = \langle\bar{m}_L\bar{m}_S|J\bar{m}_J\rangle\langle\bar{m}_I\bar{m}_J|Fm_F\rangle$ is simply the product of two Clebsch-Gordan coefficients.

In the regime $c_{hf} \ll E_B \ll c_f$, the electronic angular momentum and the nuclear spins are decoupled, and Q corresponds to $\{J, m_J, m_I\}$, with $C^{Q}_{\bar{m}_L \bar{m}_S \bar{m}_I} = \langle \bar{m}_L \bar{m}_S \bar{m}_I | J m_J m_I \rangle = \delta_{\bar{m}_I m_I} \langle \bar{m}_L \bar{m}_S | J m_J \rangle$. In this case, the dipole transition element obeys $D^{L'Q'}_{q,LQ} \propto \delta_{m_I m'_I}$, and the states with different nuclear spins are not coupled by the lasers.

In an extremely strong magnetic field such that $E_B \gg c_f$, the electronic spins and the electronic orbital angular momentum are decoupled, and Q corresponds to $\{m_L, m_S, m_I\}$, with $C^{Q}_{\bar{m}_L \bar{m}_S \bar{m}_I} = \delta_{\bar{m}_L m_L} \delta_{\bar{m}_S m_S} \delta_{\bar{m}_I m_I}$. In this case, the dipole transition element obeys $D^{L'Q'}_{q,LQ} \propto \delta_{m_S m'_S} \delta_{m_I m'_I}$, and states with disparate nuclear or electronic spin projections are not coupled by the lasers. In short, the large fields polarize the electronic spins and nuclear spins, making them robust quantum numbers which cannot be influenced by optical fields.

9.4.4 Numerical results

Here we numerically calculate $D^{L'Q'}_{q,LQ}$ in the intermediate regime $E_B \gtrsim c_{hf}$. For ^{6}Li, $c_{hf} \lesssim E_B \lesssim c_f$, one needs to diagonalize the Hamiltonian (9.4). The numerics are simpler for other alkali atoms where $c_{hf} \lesssim E_B \ll c_f$. In this case Q is decomposed into J and $\tilde{Q}$, with the latter labeling the eigenstates of the simplified Hamiltonian in Eq. (9.7). The coefficient $C^{Q}_{\bar{m}_L \bar{m}_S \bar{m}_I}$ is then reduced as $C^{Q}_{\bar{m}_L \bar{m}_S \bar{m}_I} = \langle \bar{m}_L \bar{m}_S | J \bar{m}_J \rangle C^{\tilde{Q}}_{\bar{m}_J \bar{m}_I}$.

As an illustration, in Fig. 9.2 we plot the dimensionless electric dipole transition $\mathcal{D}^{\tilde{Q}\tilde{Q}'}_{q} \equiv D^{L'J'\tilde{Q}'}_{q,LJ\tilde{Q}} / \langle L \| er \| L' \rangle$ as a function of the magnetic field for ^{23}Na, where we choose the eigenstates of $L = 0, J = 1/2$ and $L' = 1, J' = 1/2$ as the initial states and the final states (D1 transitions), and use σ^- polarized light.

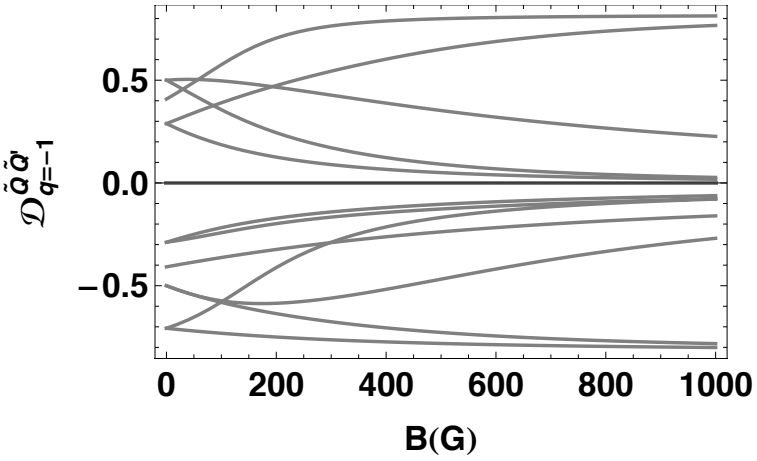

Figure 9.2: Dimensionless electric dipole transition $\mathcal{D}_q^{\tilde{Q}\tilde{Q}'} \equiv D^{L'J'\tilde{Q}'}_{q,LJ\tilde{Q}}/\langle L||er||L'\rangle$ as a function of magnetic field for ^{23}Na, with the parameters $L = 0, J = 1/2, L' = 1, J' = 1/2$ and $q = -1$. The twelve different lines correspond to all of the various allowed dipole transitions for σ^- light.

The $F = 1, 2$ and $F' = 1, 2$ manifolds allow twelve σ^- transitions. At large fields, the absolute values of four of them saturate at finite values while the rest of them approach zero. This large field result stems from the decoupling of the electronic and nuclear spins. (the $\tilde{Q}$ eigenstates can be described by m_J, m_I in that limit). Under such circumstance, the allowed transitions for the σ^- transition only occur at $m_J = 1/2, m'_J = -1/2$ and $m_I = m'_I$ with $m_I = -3/2, -1/2, 1/2, 3/2$.

9.5 Magnetic field dependance of Raman coupling

We have illustrated how the electric dipole transition $\mathcal{D}_q^{\tilde{Q}\tilde{Q}'}$ depends on the magnetic field. Here we calculate the ratio $\beta = \Omega_R/\Gamma_{\text{ine}}$ using Eq. (9.1) and Eq. (9.3) from Sec. II, and the relation $\Omega_{i\epsilon} \propto \sqrt{I_i}\mathcal{D}_q^{\tilde{Q}\tilde{Q}'}$, with I_i the intensity of each laser.

In Fig. 9.3, we plot β as a function of the magnetic field for various alkali atoms at $\Delta = (2\pi\hbar) \times 100\text{THz} \gg A_f$, where we assume $|g_1\rangle$ and $|g_2\rangle$ are the lowest

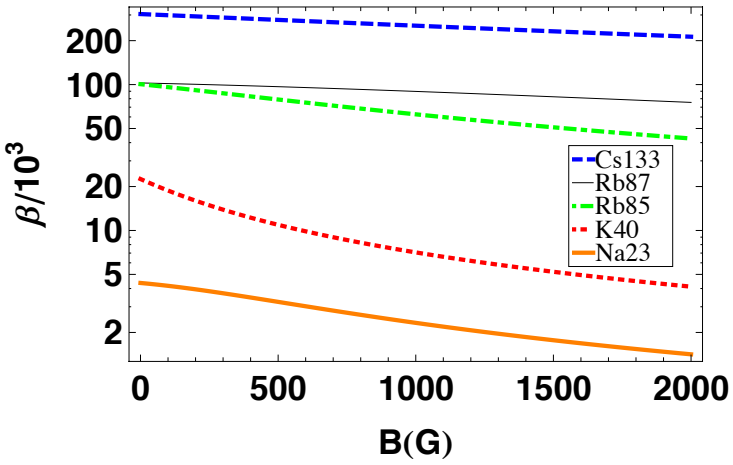

Figure 9.3: Ratio $\beta = \Omega_R/\Gamma_{\text{ine}}$ as a function of magnetic field B for various alkali atoms at $\Delta = (2\pi\hbar) \times 100\text{THz}$. Ω_R is the Raman Rabi rate, and Γ_{ine} is the inelastic scattering rate. Note the logarithmic vertical scale.

ground states, and the two lasers with σ^+ and π polarized light have an equal intensity. We see that although the ratios decrease with the magnetic field, they are still quite appreciable at $B \sim 200\text{G}-1200\text{G}$, suggesting that the Raman experiment and strong Feshbach-induced interactions are compatible.

Given that ^{6}Li is in a different regime than the other alkalis, it is convenient to discuss its properties separately. Analyzing Eqs. (9.5)-(9.6), without making the approximations inherent in Eq. (9.7), yields the transition rates in Fig. 9.4. Looking at the blue (dashed) curve in Fig. 9.4(a), we see at the large detuning, the ratio of the Raman Rabi rate to the inelastic scattering rate for ^{6}Li decreases faster than those for the heavier atoms in Fig. 9.3. This rapid fall-off can be attributed to the much weaker coupling between the electronic and nuclear spins in ^{6}Li. At the magnetic field of Feshbach resonance $B = 834\text{G}$ [65], β is suppressed by a factor of 7. At small detuning Δ the ratio β changes non-monotonically with the magnetic field, as Γ_{ine} decreases faster than Ω_R. In Fig. 9.4(b), we see that β increases rapidly for small Δ and levels out at large Δ. There

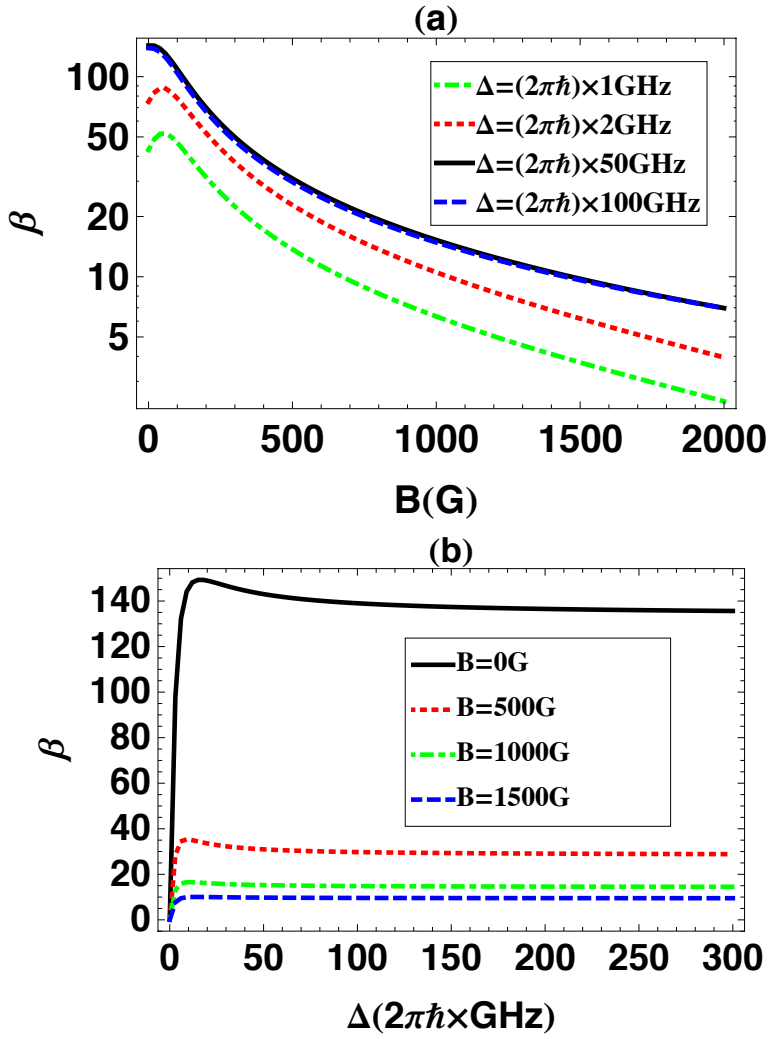

Figure 9.4: (a): Ratio $\beta = \Omega_R/\Gamma_{\text{ine}}$ as a function of magnetic field B for various detuning Δ for ^{6}Li. (b): Ratio β as a function of detuning Δ for various magnetic field B.

is an optimal detuning near $\Delta \approx A_f$, where β has a maxima. The peak value of β, however, is only marginally larger than its large Δ asymptotic value. Moreover, the peak is further reduced as B increases.

9.6 Conclusions

In summary, we comprehensively studied the Raman Rabi rates of alkali atoms in the presence of a magnetic field. While the ratio of the Raman Rabi frequency to the inelastic scattering rate decreases with the magnetic field, the suppression is *not* significant for most alkali atoms at the typical fields of the Feshbach resonance. Our primary motivation is evaluating the feasibility of using Raman techniques to generate strongly interacting Fermi gases with spin-orbit coupling. We conclude that ^{6}Li is not a good candidate, but ^{40}K is promising.

CHAPTER 10

ANOMALOUS CHARGE PUMPING IN A ONE DIMENSIONAL SUPERLATTICE

This chapter was adapted from "Anomalous charge pumping in a one dimensional optical superlattice" by Ran Wei and Erich J. Mueller, published in Physical Review A 92, 013609 (2015).

10.1 Abstract

We model atomic motion in a sliding superlattice potential to explore topological "charge pumping" and to find optimal parameters for experimental observation of this phenomenon. We analytically study the band-structure, finding how the Wannier states evolve as two sinusoidal lattices are moved relative to one-another, and relate this evolution to the center of mass motion of an atomic cloud. We pay particular attention to counterintuitive or anomalous regimes, such as when the atomic motion is opposite to that of the lattice.

10.2 Introduction

Slow periodic changes in a lattice potential can transport charge. For a filled band, the integrated particle current per cycle in such an adiabatic pump is quantized [171]. We study a simple but rich example of this phenomenon, namely charge transport in a sliding superlattice, and draw attention to its counterintuitive properties such as regimes where the charge moves faster than the potential, or even travels in the opposite direction. The mathematics predicting

this anomalous transport goes back 30 years [33, 172], but has not been observed in experiments. We here argue that this effect is observable in a cold atom experiment.

The quantum mechanics of particles in a one dimensional (1D) superlattice is rich, for incommensurate periods boasting a fractal energy spectrum [19], and a localization transition similar to what is seen in disordered lattices [173]. While recent studies have focused on the tight-binding limit (the Aubry-Andre model) [174, 175, 176, 177, 178, 179, 180, 181, 182, 183, 184, 185, 186, 187, 188, 189, 190, 191], we study the continuous limit of the 1D superlattice, where, because of the weak potential, the single-particle spectra can be calculated perturbatively. Related cold atom proposals on quantized transport [192, 193, 194, 195, 196, 197] have focused on the simplest superlattice where one sub-lattice constant is half of the other, and the lowest band is therefore not in the anomalous regime which interests us. Ref. [192], draws attention to anomalous retrograde motion of particles in the second band, an approach which complements our ground-state proposal.

The 1D superlattice can be mapped onto the Harper-Hofstadter model [19, 18]. The topological numbers (Chern numbers) associated with charge pumping can be mapped onto quantized Hall conductances [33, 198]. Recent experiments involving artificial gauge fields on 2D optical lattice have aimed to measure these 2D Chern numbers [12, 13, 14, 199, 200]. There are also related studies based on measurement of Hall drift [201], Bloch oscillations [202, 203], Zak phase [204, 205, 206], time-of-flight images [207, 208, 209], edge states [210, 211, 212, 213, 214, 215], or density plateaus [216, 217].

In this chapter, we study the charge transport in a 1D sliding superlattice,

where the moving lattice period is an arbitrary rational multiple of the static lattice. We analytically calculate energy band gaps and the topological invariants which give the integrated adiabatic current per pumping cycle [171]. The fact that this current can be made *arbitrarily large* and/or *opposite* to the direction of the sliding potential is counterintuitive. We present a physical interpretation of this phenomenon in terms of the quantum tunneling of Wannier functions between minima in the potential. We propose an experiment to detect this anomalous adiabatic current, and derive the optimal parameters. Through numerical simulations, we confirm that a *negative* integrated current and a nontrivial Chern number $C = -1$ is readily measured in an experiment. We analyze corrections to adiabaticity, the harmonic trap, multi-band effects, and finite-size effects.

10.3 Model

We consider the Hamiltonian of a 1D superlattice where one lattice adiabatically slides relative to the other,

$$H = \int dx\, \psi^\dagger(x) \left(-\frac{\hbar^2}{2m}\partial_x^2 + V_1(x,\varphi) + V_2(x) \right) \psi(x) \tag{10.1}$$

where $\psi(x)$ represents the field operator of the particle, $\hbar$ is Planck's constant, and m is the mass of the particle. The periodic potentials $V_1(x,\varphi) = 2v_1 \cos(px-\varphi)$ and $V_2(x) = 2v_2 \cos(qx)$ are commensurate, with lattice constants $2\pi/p$ and $2\pi/q$, intensities v_1 and v_2. We take the relative phase φ to be slowly varying in time. The period of the Hamiltonian is set by the greatest common divisor of p and q, i.e., $\kappa \equiv \gcd(p,q)$, as illustrated in the inset of Fig. 10.1. Treating $1/\kappa$ as the unit length, we redefine $x\kappa \to x$, $p/\kappa \to p$, and $q/\kappa \to q$. Treating $E_r = \hbar^2\kappa^2/m$

as the unit energy, we redefine $H/E_r \to H$, $v_1/E_r \to v_1$, and $v_2/E_r \to v_2$. The dimensionless Hamiltonian in the momentum space is then

$$H = \sum_k \frac{k^2}{2}\psi_k^\dagger\psi_k + \left(v_1 e^{-i\varphi}\psi_k^\dagger\psi_{k+p} + v_2\psi_k^\dagger\psi_{k+q} + h.c.\right) \tag{10.2}$$

Here $\psi_k = \frac{1}{\sqrt{L}}\int dx\, e^{ikx}\psi(x)$, with dimensionless system length L and dimensionless momentum k. Since states of momentum k are coupled only to those of momentum $k+n$ for integer n, we restrict ourselves to the first Brillouin zone ($0 \le k < 1$) and rewrite the Hamiltonian,

$$H = \sum_{0\le k<1}\sum_{n=-\infty}^{\infty} \frac{1}{2}(k+n)^2\psi_n^\dagger\psi_n + \left(v_1 e^{-i\varphi}\psi_n^\dagger\psi_{n+p} + v_2\psi_n^\dagger\psi_{n+q} + h.c.\right) \tag{10.3}$$

where we have suppressed the k index, writing $\psi_n \equiv \psi_{k+n}$.

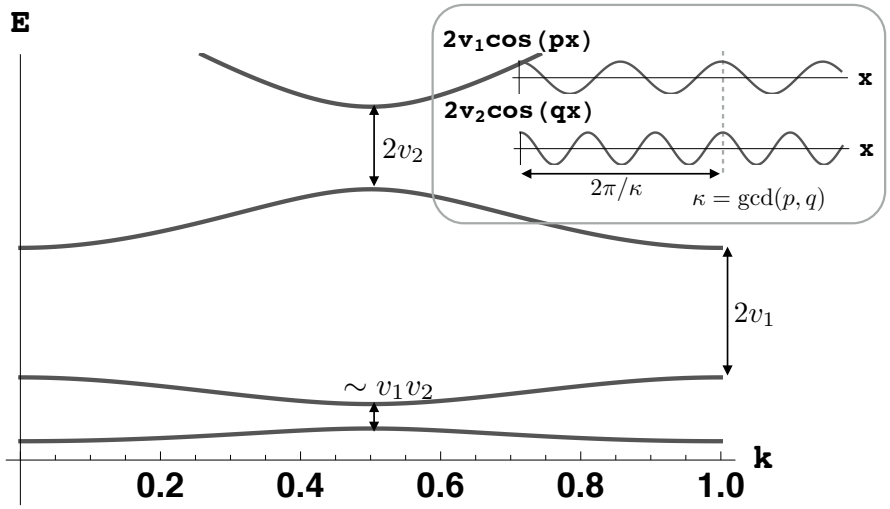

Figure 10.1: Band structure of a 1D superlattice for $p = 2, q = 3$, showing energy E vs dimensionless wave-vector k for weak potentials. Inset shows the two potential making up the superlattice, and illustrates the unit cell with period set by the greatest common divisor $\kappa \equiv \gcd(p, q)$. For this choice of p and q, the energy gap between the third and fourth band is set by the potential strength $2v_2$, the gap between the second and third band is set by the potential strength $2v_1$, and the small gap between the second and third band scales as $\sim v_1 v_2$.

To illustrate the resulting band structure, we impose a cut-off on n, and numerically diagonalize the Hamiltonian in Eq. (10.1) for $p = 2$ and $q = 3$. The

lowest four energy bands are shown in Fig. 10.1, and even for this simple case the gaps display a range of behaviors for small v_1 and v_2. The gap between the third and fourth band is induced by the potential $V_2(x)$, and is proportional to v_2 for weak potentials. The gap between the second and third band is induced by $V_1(x)$, and is proportional to v_1. The small gap between the second and third band is induced by the combination of these two potentials, which scales as $\sim v_1 v_2$. In the following section, we will discuss the origin of these scalings in the context of understanding the lowest energy gap.

10.4 Band gaps and topology

The eigenstates of the Hamiltonian in Eq. (10.3) can be found perturbatively in the limit of $v_1, v_2 \ll 1$. Suppressing the index k, we write $H = H_0 + \lambda H_1$, with

$$H_0 = \sum_{n=-\infty}^{\infty} \frac{1}{2}(k+n)^2 \psi_n^\dagger \psi_n \tag{10.4}$$

$$\lambda H_1 = \lambda_p H_p + \lambda_{-p} H_{-p} + \lambda_q H_q + \lambda_{-q} H_{-q}, \tag{10.5}$$

where $H_p = \sum_{n=-\infty}^{\infty} \psi_n^\dagger \psi_{n+p}$, $H_q = \sum_{n=-\infty}^{\infty} \psi_n^\dagger \psi_{n+q}$, and λ is a formal small parameter, with $\lambda_p = \lambda_{-p}^* = v_1 e^{-i\varphi}$ and $\lambda_q = \lambda_{-q}^* = v_2$.

For small λ and $0 \leq k < 1$, the eigenstates of the lowest band will be superpositions of $|-1\rangle$ and $|0\rangle$, where $|m\rangle = \psi_m^\dagger |\text{vac}\rangle$. We let $\delta k = k - 1/2$ denote the distance of k from the band crossing point and assume $\delta k > 0$. The physics for $\delta k < 0$ is analogous. While ordinary perturbation theory works far from the crossing ($\delta k \gg \epsilon$, where ϵ will be precisely defined below), one must use higher order degenerate perturbation theory to find the eigenstates for $\delta k \lesssim \epsilon$.

As argued in **Appendix 10.8.1**, the resulting effective Hamiltonian is of the form

$$H_{\text{eff}} = PH_0P + \sum_{s_+\geq 0}\sum_{s_-\geq 0}\sum_{r_+\geq 0}\sum_{r_-\geq 0} \lambda_p^{s_+}\lambda_{-p}^{s_-}\lambda_q^{r_+}\lambda_{-q}^{r_-}\,\mathcal{L}^{(s_+,s_-,r_+,r_-)} \tag{10.6}$$

where $P = |-1\rangle\langle -1| + |0\rangle\langle 0|$, and s_+, s_-, r_+, r_- are integers. The operator $\mathcal{L}^{(s_+,s_-,r_+,r_-)}$ is the contribution to H_{eff} involving the absorption of $\eta = sp + rq$ units of momentum from the lattices, where $s = s_+ - s_-$ and $r = r_+ - r_-$. By conservation of momentum, $\alpha \equiv \left\langle -1 \left| \mathcal{L}^{(s_+,s_-,r_+,r_-)} \right| 0 \right\rangle = 0$ unless $\eta = 1$. We linearize H_{eff} about $\delta k = 0$, and write the operators in the basis $\{|-1\rangle, |0\rangle\}$. At the lowest nontrivial order, we have

$$\mathcal{H}_{\text{eff}} = \begin{pmatrix} -\frac{1}{2}\delta k & \alpha\Delta e^{i\chi} \\ \alpha\Delta e^{-i\chi} & \frac{1}{2}\delta k \end{pmatrix} + \text{const.}, \tag{10.7}$$

where $\Delta = v_1^{|r_m|}v_2^{|s_m|}, \chi = -s_m\varphi$, and s_m, r_m correspond to the absolutely smallest solution to the Diophantine equation $sp + rq = 1$. This result agrees with a similar perturbative analysis carried out by Thouless *et al.* [33] and Niu [172] for related models.

The off-diagonal terms of Eq. (10.7) split the energy degeneracy at $\delta k = 0$, and create an energy gap of size $\Delta E_g \equiv 2|\alpha\Delta|$. For example, if $p = 2, q = 3$, the absolutely smallest solution to the Diophantine equation has $s_m = -1, r_m = 1$, as $-p + q = 1$. Thus the energy gap is $2|\alpha v_1 v_2|$, as denoted in Fig. 10.1. For larger $|s_m|$ and $|r_m|$, the energy gap can be extremely small. Ordinary perturbation theory would have sufficed in the regime where $\delta k \gg 2|\alpha\Delta|$, allowing us to identify ϵ as $2|\alpha\Delta|$. Properties of higher bands can be analyzed similarly.

By analyzing Eq. (10.7), we find that the lowest energy eigenstate of Eq. (10.4-10.5) has the form

$$|k, \varphi\rangle = -\sin\frac{\beta}{2}e^{i\chi/2}|-1\rangle + \cos\frac{\beta}{2}e^{-i\chi/2}|0\rangle + ..., \tag{10.8}$$

where $\tan\beta = -2\alpha\Delta/\delta k$. The neglected terms are higher order in v_1 and v_2. For $\delta k \gg 2|\alpha\Delta|$, $\sin\frac{\beta}{2} \approx 1$ and $\cos\frac{\beta}{2} \approx 0$, and the coefficients are featureless.

Slowly changing φ generates an adiabatic current [171]. For a completely filled band, the integrated current in one pumping period (φ from 0 to 2π) is [37]

$$\Delta Q = 2\pi C = \int_0^1 dk \int_0^{2\pi} d\varphi\, \Omega_{k\varphi} \tag{10.9}$$

where the Berry curvature is

$$\Omega_{k\varphi} = i\left(\partial_\varphi \langle k, \varphi | \partial_k | k, \varphi\rangle - h.c.\right) = \frac{s_m}{2}\partial_k \cos\beta. \tag{10.10}$$

We see $\Omega_{k\varphi}$ is concentrated near the location of the energy gap. Integrating the Berry curvature is trivial, yielding the Chern number $C = s_m$. Although our argument requires that v_1 and v_2 are small, due to the quantized nature of C, the result should hold for all nonzero v_1 and v_2. In our numerical calculations with larger v_1, v_2, we find the curvature is roughly uniform over the Brillouin zone, but as expected its integral is unchanged.

10.5 Anomalous charge pumping

By appropriately choosing p and q, one can make $C = s_m$ an arbitrary integer [218, 219, 220, 221]. This means that in one pumping cycle a single particle may move arbitrarily far and/or opposite to the direction of the sliding potential. Such long-distance and/or retrograde transport seems unphysical. The magic comes from the adiabatic process: If the potential moves sufficiently slowly, the particles always stay in a global minimum of the potential. Due to the structure of the superlattice, a slight motion of the potential could result in a dramatic change of the locations of the global minima (see Fig. 10.2(a)). Within a small

portion of a pumping cycle, the particles may "tunnel" to the new global minima which could be a large distance away from the old minima.

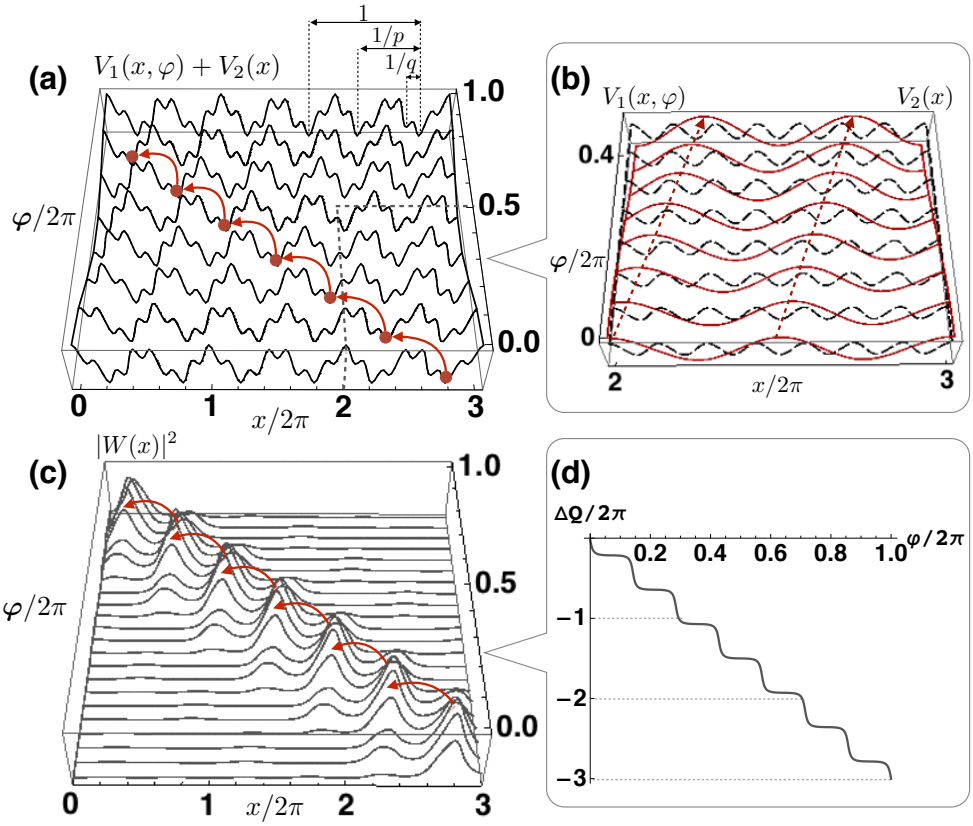

Figure 10.2: (a) Illustration of adiabatic charge transport in a 1D superlattice, where the particle "travels" through three unit cells to the left when the lattice potential moves to the right by one period. Solid lines show the potential $V_1(x,\varphi) + V_2(x)$ for different values of φ. Arrows schematically show how the locations of the minima shift discontinuously. (b) illustrates evolution of two separated potentials of the superlattice: the right-sliding potential $V_1(x,\varphi)$ (solid red) and the static potential $V_2(x)$ (dashed black). (c) Evolution of Wannier function. Arrows indicate the "tunneling" process. (d) shows the evolution of integrated adiabatic current as a function of φ. In these plots we choose $p = 2$ and $q = 7$, so the Chern number is $C = s_m = -3$. Other parameters are $v_1 = 0.5$ and $v_2 = 0.25$.

To further quantify our interpretations, we calculate the integrated current

$$\Delta Q(\varphi) = \frac{1}{2\pi}\int_0^1 dk \int_0^{\varphi} d\varphi'\, \Omega_{k\varphi'}, \tag{10.11}$$

and the Wannier function at lattice site j [222]

$$W_j(x,\varphi) = \sum_{0\le k<1} e^{ikj}\Psi_k(x,\varphi), \tag{10.12}$$

where the Bloch wave function is

$$\Psi_k(x,\varphi) = \frac{1}{\sqrt{L}}\sum_{n=-\infty}^{\infty}\langle n|k,\varphi\rangle e^{-i(n+k)x}. \tag{10.13}$$

Here we choose a *smooth* gauge for the Bloch wave function, so the Wannier function is well localized [223].

Fig. 10.2(d) shows the integrated current as a function of φ, calculated from Eq. (10.11) using a similar method to Ref. [224]. We see the function is "step-like": Flat regions correspond to slow transport, while the particle motion is rapid in the steep regions. This is further illustrated by the Wannier function in Fig. 10.2(c). During the slow transport, the Wannier function slowly drifts, while during the rapid transport, one peak drops in amplitude, and a second peak rises. This corresponds to tunneling.

For small v_1, v_2, the timescale for adiabaticity τ is related to the size of the gap, $1/\tau \sim |\alpha\Delta| \sim v_1^{|s_m|}v_2^{|r_m|}$. Thus when the Chern number $C = s_m$ is large and the potentials are weak, adiabaticity is hard to maintain in a practical experiment. For large v_1, v_2, the gap again falls, owing to the large potential barriers. Fig. 10.3 shows the energy gap ΔE_g as a function of v_1 and v_2 for $p = 2, q = 3$. The gap has a maximium value of $\Delta E_g \approx 0.09$ at $v_1 = 0.23$ and $v_2 = 0.95$. An optimized experiment would be performed with these parameters.

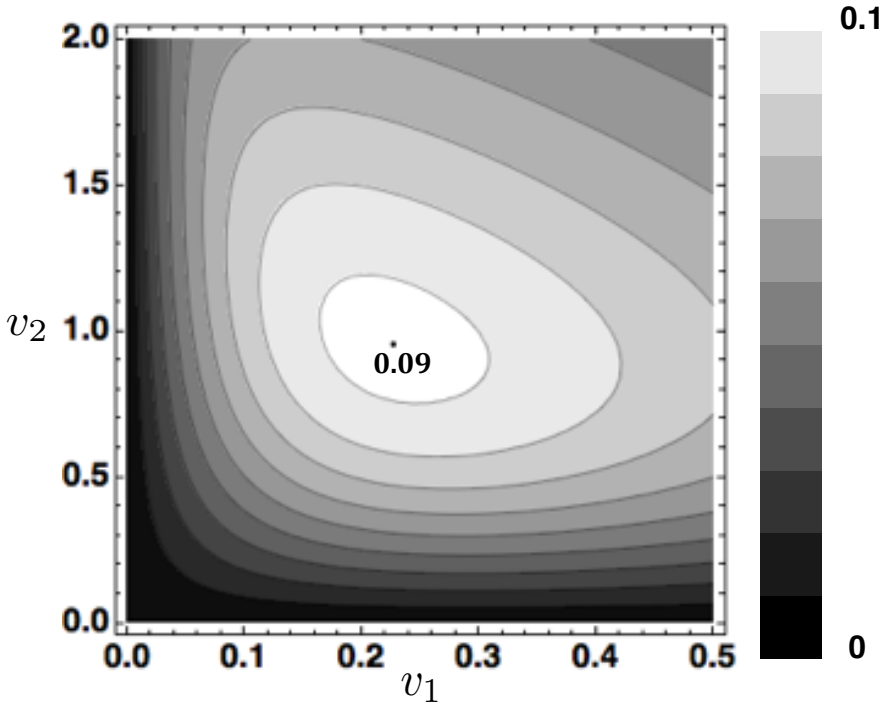

Figure 10.3: Energy gap ΔE_g as a function of v_1, v_2 for $p = 2, q = 3$. The gap has a maximium value of $\Delta E_g \approx 0.09$ at $v_1 = 0.23$ and $v_2 = 0.95$.

10.6 Experimental proposal

To observe this anomalous current, we envision a Fermi gas confined to a quasi-1D tube, such that only one transverse mode is occupied. Although the present analysis is 1D, we expect the phenomena will persist for more general transverse confinement. Along the tube we engineer two longitudinal periodic potentials $V_1(x, \varphi) = 2v_1 \cos(px - \varphi)$ and $V_2(x) = 2v_2 \cos(qx)$ via two pairs of counter-propagating laser beams. The time-dependent phase $\varphi = \delta\omega\, t$ is produced by a frequency difference $\delta\omega$ between two of the beams. To satisfy the adiabatic condition, we require $\hbar\delta\omega \ll \Delta E_g$. The resulting adiabatic particle current can be detected by observing the motion of the center of mass of the cloud: After time $t = 2\pi N/\delta\omega$, the center of mass should move a distance $r_c = 2\pi CN/\kappa$. A dimensionless measure of this displacement is $x_c = \kappa r_c$. The displacement can be

measured *in-situ* [225, 226, 227] or after time-of-flight [228]. Similar experiments were proposed by Chiang and Niu [192], and Wang, Troyer and Dai [195].

In modeling this experiment, one must account for the finite cloud size. We include this physics by adding a harmonic potential along the tube, $V(x) = m\omega_0^2 x^2/2$. Such potentials are always found in such experiments. Within a local density approximation, the lowest band will be filled at the center of the cloud, but only partially filled near the edge. Although our Chern number argument only applies to the central region, we still expect the center of mass motion to be nearly quantized. For $\hbar\omega_0 \ll v_1, v_2$, and the particle number much greater than one, only a very small portion of particles live at boundaries. Our numerical simulations (detailed below) confirm this results. For a typical experiment, $\omega_0 \sim 10$ Hz, and $v_1/\hbar, v_2/\hbar \sim 100$ kHz [229].

Because of the trap, the displacement r_c cannot be made arbitrarily large. When $m\omega_0 r_c^2/2$ is of order of the band gap ΔE_g, atoms can tunnel to the higher bands. In our numerical simulation, we see that for small $\delta\omega$, the maximum displacement scales as $1/\omega_0$.

10.7 Numerical simulation

In order to see the feasibility of our experimental proposal, we numerically simulate the dynamical evolution of a 1D Fermi gas. We take the many-body state to be a Slater determinant, made up from single-particle wave functions $\psi_i(x,t)$ with $1 \le i \le \nu$, where ν is the number of fermions. At time $t = 0$, $\psi_i(x,0)$ is the ith eigenstate of the Hamiltonian. We evolve $\psi_i(x,t)$ via the time-dependent single-particle Schrödinger equation, and then calculate the center

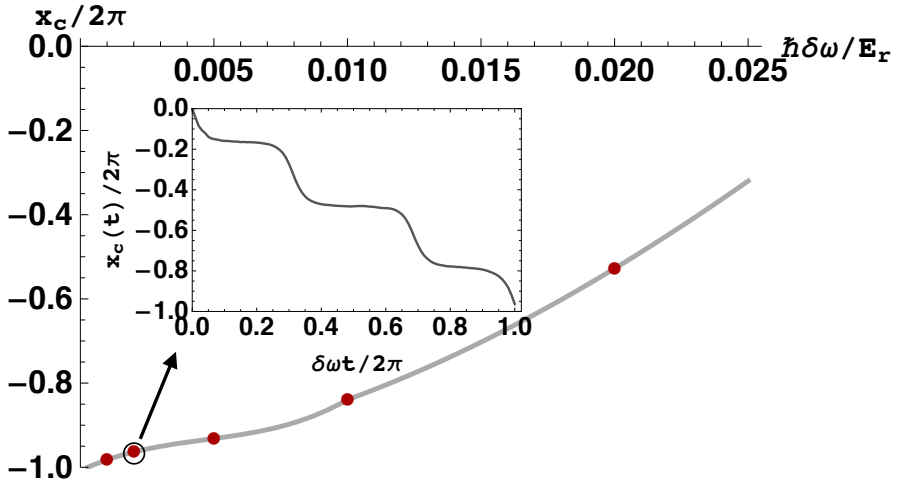

Figure 10.4: Displacement of the center of mass (in units of the superlattice) after one pumping period $T = 2\pi/\delta\omega$ for $\nu = 63$ fermions in a superlattice with $p = 2, q = 3, v_1 = 0.23E_r, v_2 = 0.95E_r$, and a harmonic trap $\hbar\omega_0 = 2.2 \times 10^{-3}E_r$. Physically, $\delta\omega$ is the detuning between the beams producing the lattice with wave-number p. We see $x_c/2\pi \to C = -1$ as $\delta\omega$ decreases. Inset shows the evolution of the center of mass for $\hbar\delta\omega = 0.002E_r$. [c.f. Fig. 10.2(d)]

of mass $x_c(t) \equiv 1/\nu \sum_{i=1}^{\nu} \int dx\, x|\psi_i(x,t)|^2$. Fig. 10.4 shows the results for $p = 2, q = 3$ where the Chern number is $C = -1$. We see $x_c < 0$, meaning that the particles travel in the *opposite* direction to the sliding potential. Remarkably this retrograde motion persists even for relatively large $\delta\omega$. As $\delta\omega \to 0$ the motion becomes quantized. A typical experiment has $E_r/\hbar \sim 100$ kHz [229], so the Chern number $C = -1$ is readily extracted when $\delta\omega \lesssim 200$ Hz. The inset of Fig. 10.4 shows the evolution of the center of mass in one pumping cycle for $\hbar\delta\omega = 0.002E_r$. We see the function is "step-like", similar to the ideal case (no harmonic trap and adiabatic) in Fig. 10.2(d).

10.8 Appendix

10.8.1 Derivation of effective Hamiltonian

Here we derive an effective Hamiltonian for Eq. (10.4-10.5). For small λ Since the eigenstates of the lowest band will be superpositions of $|-1\rangle$ and $|0\rangle$, motivating projection operators

$$P = |-1\rangle\langle -1| + |0\rangle\langle 0| \tag{10.14}$$

$$Q = 1 - P. \tag{10.15}$$

The states $|m\rangle = \psi_m^\dagger|\text{vac}\rangle$, satisfy $H_0|m\rangle = \frac{1}{2}(k_x + m)^2|m\rangle$. We seek eigenstates $H|\psi\rangle = E|\psi\rangle$. We break the wave function into two parts

$$|\psi\rangle = P|\psi\rangle + Q|\psi\rangle \equiv |\psi_0\rangle + |\psi_{\text{ex}}\rangle, \tag{10.16}$$

where $|\psi_0\rangle$ is in the low energy sector, and $|\psi_{\text{ex}}\rangle$ is a superposition of the higher-energy states. The eigen-equation is then decoupled into two equations

$$PH|\psi\rangle = PE|\psi\rangle = E|\psi_0\rangle \tag{10.17}$$

$$QH|\psi\rangle = QE|\psi\rangle = E|\psi_{\text{ex}}\rangle. \tag{10.18}$$

Inserting the identity $P^2 + Q^2 = P + Q = 1$ on the left hand side of Eq. (10.17)-(10.18) and substituting $|\psi_{\text{ex}}\rangle$ in terms of $|\psi_0\rangle$, we obtain a closed equation for $|\psi_0\rangle$,

$$H_{\text{eff}}|\psi_0\rangle = E|\psi_0\rangle, \tag{10.19}$$

where

$$H_{\text{eff}} \equiv PHP + PHQ\frac{1}{E - QHQ}QHP. \tag{10.20}$$

Using the identity $PH_0Q = 0$ and expanding the second term of Eq. (10.20), we obtain

$$H_{\text{eff}} = PH_0P + \lambda PH_1P + \lambda^2 PH_1Q \sum_{j=0}^{\infty} \frac{1}{E - QH_0Q} \left(\lambda \frac{QH_1Q}{E - QH_0Q} \right)^j QH_1P. \quad (10.21)$$

This equation can be written as

$$H_{\text{eff}} = PH_0P + \sum_{s_+\geq 0} \sum_{s_-\geq 0} \sum_{r_+\geq 0} \sum_{r_-\geq 0} \lambda_p^{s_+} \lambda_{-p}^{s_-} \lambda_q^{r_+} \lambda_{-q}^{r_-} \mathcal{L}^{(s_+,s_-,r_+,r_-)} \quad (10.22)$$

where the momentum conservation implies that $\alpha \equiv \left\langle -1 \left| \mathcal{L}^{(s_+,s_-,r_+,r_-)} \right| 0 \right\rangle = 0$ unless $sp + rq = 1$, where $s = s_+ - s_-$ and $r = r_+ - r_-$. In our problem, the lowest order contribution to α has either $s_+ = 0$ or $s_- = 0$. Similarly $r_+ = 0$ or $r_- = 0$. The lowest order contribution to the diagonal elements of H_{eff} corresponds to an identity matrix.

Linearizing H_{eff} about $\delta k = 0$, and writing the operators in the basis $\{|-1\rangle, |0\rangle\}$, we have

$$\mathcal{H}_{\text{eff}} = \begin{pmatrix} -\frac{1}{2}\delta k & \alpha\Delta e^{i\chi} \\ \alpha\Delta e^{-i\chi} & \frac{1}{2}\delta k \end{pmatrix} + \text{const.}, \quad (10.23)$$

where $\Delta = v_1^{|r_m|} v_2^{|s_m|}, \chi = -s_m\varphi$, and s_m, r_m correspond to the absolutely smallest solution to the Diophantine equation $sp + rq = 1$.

BIBLIOGRAPHY

[1] Y.-J. Lin, R. L. Compton, K. Jiménez-García, J. V. Porto, and I. B. Spielman, Nature (London) **462**, 628 (2009).

[2] J. Dalibard, F. Gerbier, G. Juzeliūnas, and P. Öhberg, Rev. Mod. Phys. **83**, 1523 (2011).

[3] N. Goldman, G. Juzeliūnas, P. Öhberg, and I. B. Spielman, Rep. Prog. Phys. **77**, 126401 (2014).

[4] I. B. Spielman, Phys. Rev. A **79**, 063613 (2009).

[5] R. Wei and E. J. Mueller, Phys. Rev. A. **87**, 042514 (2013).

[6] Y.-J. Lin, K. Jiménez-García, and I. B. Spielman, Nature (London) **471**, 83 (2011).

[7] Y. A. Bychkov and E. I. Rashba, J. Phys. C **17**, 6039 (1984).

[8] G. Dresselhaus, Phys. Rev. **100**, 580 (1955).

[9] V. Galitski and I. B. Spielman, Nature (London) **494**, 49 (2013).

[10] L. Huang, Z. Meng, P. Wang, P. Peng, S.-L. Zhang, L. Chen, D. Li, Q. Zhou, and J. Zhang, arXiv:1506.02861 (2015).

[11] Z. Wu, L. Zhang, W. Sun, X.-T. Xu, B.-Z. Wang, S.-C. Ji, Y. Deng, S. Chen, X.-J. Liu, and J.-W. Pan, arXiv:1511.08170 (2015).

[12] M. Aidelsburger, M. Atala, S. Nascimbène, S. Trotzky, Y.-A. Chen, and I. Bloch, Phys. Rev. Lett. **107**, 255301 (2011).

[13] M. Aidelsburger, M. Atala, M. Lohse, J. T. Barreiro, B. Paredes, and I. Bloch, Phys. Rev. Lett. **111**, 185301 (2013).

[14] H. Miyake, G. A. Siviloglou, C. J. Kennedy, W. C. Burton, and W. Ketterle, Phys. Rev. Lett. **111**, 185302 (2013).

[15] M. Atala, M. Aidelsburger, M. Lohse, J. T. Barreiro, B. Paredes, and I. Bloch, Nat. Phys. **10**, 588 (2014).

[16] R. Wei and E. Mueller, Phys. Rev. A **84**, 063611 (2011).

[17] E. J. Mueller, Physics **4**, 107 (2011).

[18] P. G. Harper, Proceedings of the Physical Society. Section A **68**, 874 (1955).

[19] D. R. Hofstadter, Phys. Rev. B **14**, 2239 (1976).

[20] C. Chin and E. J. Mueller, Physics **6**, 118 (2013).

[21] C. J. Pethick and H. Smith, *Bose-Einstein Condensation in Dilute Gases* (Cambridge University Press, Cambridge, 2002).

[22] P. G. deGennes, *Superconductivity of Metals and Alloys* (W. A. Benjamin, New York, 1966).

[23] M. Olshanii, Phys. Rev. Lett. **81**, 938 (1998).

[24] L. D. Landau, J. Phys. (Moscow) **5**, 71 (1941).

[25] L. D. Landau, J. Phys. (Moscow) **11**, 91 (1947).

[26] J. Bardeen, L. Cooper, and J. R. Schrieffer, Phys. Rev. **108**, 1175 (1957).

[27] N. N. Bogoliubov, Nuovo Cimento **7**, 794 (1958).

[28] S. Baur, Ph.D. thesis, Cornell University, 2011.

[29] X.-L. Qi and S.-C. Zhang, Physics Today **63**, 33 (2010).

[30] J. E. Moore, Nature (London) **464**, 194 (2010).

[31] K. v. Klitzing, G. Dorda, and M. Pepper, Phys. Rev. Lett. **45**, 494 (1980).

[32] Landau, L. D. and E. M. Lifshitz, *Statistical Physics* (Pergamon Press, Oxford, 1980).

[33] D. J. Thouless, M. Kohmoto, M. P. Nightingale, and M. den Nijs, Phys. Rev. Lett. **49**, 405 (1982).

[34] X. G. Wen, Adv. Phys. **44**, 405 (1995).

[35] M. Z. Hasan and C. L. Kane, Rev. Mod. Phys. **82**, 3045 (2010).

[36] X.-L. Qi and S.-C. Zhang, Rev. Mod. Phys. **83**, 1057 (2011).

[37] D. Xiao, M. Chang, and Q. Niu, Rev. Mod. Phys. **82**, 1959 (2010).

[38] J. Zak, Phys. Rev. Lett. **62**, 2747 (1989).

[39] M. J. Rice and E. J. Mele, Phys. Rev. Lett. **49**, 1455 (1982).

[40] M. Atala, M. Aidelsburger, Julio T. Barreiro, D. Abanin, T. Kitagawa, E. Demler, and I. Bloch, Nat. Phys. **9** 795 (2013).

[41] W. P. Su, J. R. Schrieffer, and A. Heeger, Phys. Rev. Lett. **42**, 1698 (1979).

[42] A. Kitaev, Phys. Usp. **44**, 131 (2001).

[43] A. P. Schnyder, S. Ryu, A. Furusaki, and A. W. W. Ludwig, Phys. Rev. B **78**, 195125 (2008).

[44] S. Ryu, A. P. Schnyder, A. Furusaki, and A. W. W. Ludwig, New J. Phys. **12**, 065010 (2010).

[45] S. Stock, Z. Hadzibabic, B. Battelier, M. Cheneau, and J. Dalibard, Phys. Rev. Lett. **95**, 190403 (2005).

[46] N. Goldman, I. Satija, P. Nikolic, A. Bermudez, M. A. Martin-Delgado, M. Lewenstein, and I. B. Spielman, Phys. Rev. Lett. **105**, 255302 (2010).

[47] M. R. Matthews, B. P. Anderson, P. C. Haljan, D. S. Hall, C. E. Wieman, and E. A. Cornell, Phys. Rev. Lett. **83**, 2498 (1999).

[48] K.W. Madison, F. Chevy, W. Wohlleben, and J. Dalibard, Phys. Rev. Lett. **84**, 806 (2000).

[49] J. R. Abo-Shaeer, C. Raman, J. M. Vogels, and W. Ketterle, Science **292**, 476 (2001).

[50] P. C. Haljan, I. Coddington, P. Engels, and E. A. Cornell, Phys. Rev. Lett. **87**, 210403 (2001).

[51] V. Schweikhard, I. Coddington, P. Engels, V. P. Mogendorff, and E. A. Cornell, Phys. Rev. Lett. **92**, 040404 (2004).

[52] M. W. Zwierlein, J. R. Abo-Shaeer, A. Schirotzek, C. H. Schunck, and W. Ketterle, Nature (London) **435**, 1047 (2005).

[53] E. J. Mueller and T. -L. Ho, Phys. Rev. Lett. **88**, 180403 (2002).

[54] K. Kasamatsu, M. Tsubota, and M. Ueda, Phys. Rev. Lett. **91**, 150406 (2003).

[55] K. Kasamatsu and M. Tsubota, Phys. Rev. A **79**, 023606 (2009).

[56] C.-H. Hsueh, T.-L. Horng, S.-C. Gou, and W. C. Wu, Phys. Rev. A **84**, 023610 (2011).

[57] S. Sinha and G. V. Shlyapnikov, Phys. Rev. Lett. **94**, 150401 (2005).

[58] P. Sánchez-Lotero and J. J. Palacios, Phys. Rev. A **72**, 043613 (2005).

[59] S. I. Matveenko, D. Kovrizhin, S. Ouvry, and G. V. Shlyapnikov, Phys. Rev. A **80**, 063621 (2009).

[60] V. Schweikhard, I. Coddington, P. Engels, S. Tung, and E. A. Cornell, Phys. Rev. Lett. **93**, 210403 (2004).

[61] A. Seidel, H. Fu, D.-H. Lee, J. M. Leinaas, and J. Moore, Phys. Rev. Lett. **95**, 266405 (2005).

[62] E. Timmermans, Phys. Rev. Lett. **81**, 5718 (1998).

[63] J. M. Gerton, D.Strekalov, I. Prodan and R. G. Hulet, Nature (London) **408**, 692 (2000).

[64] P. Engels, I. Coddington, P. C. Haljan, and E. A. Cornell, Phys. Rev. Lett. **89**, 100403 (2002).

[65] C. Chin, R. Grimm, P. Julienne, and E. Tiesinga, Rev. Mod. Phys. **82**, 1225 (2010).

[66] S. Kraft, F. Vogt, O. Appel, F. Riehle, and U. Sterr, Phys. Rev. Lett. **103**, 130401 (2009).

[67] S. Stellmer, M. K. Tey, B. Huang, R. Grimm, and F. Schreck, Phys. Rev. Lett. **103**, 200401 (2009).

[68] Y. N. Martinez de Escobar, P.G. Mickelson, M. Yan, B. J. DeSalvo, S. B. Nagel, and T. C. Killian, Phys. Rev. Lett. **103**, 200402 (2009).

[69] M. Lu, N. Q. Burdick, S. H. Youn, and B. L. Lev, Phys. Rev. Lett. **107**, 190401 (2011).

[70] M. W. Zwierlein, J. R. Abo-Shaeer, A. Schirotzek, C. H. Schunck, and W. Ketterle, Nature (London) **435**, 1047 (2005).

[71] D. F. Agterberg, and, H. Tsunetsugu, Nat. Phys. **4**, 639 (2008).

[72] A. I. Larkin and Y. N. Ovchinnikov, Soviet Phys. JETP **20**, 762 (1965).

[73] K. Kim and D. R. Nelson, Phys. Rev. B, **64**, 054508 (2001).

[74] W. Hofstetter, I. Affleck, D. Nelson, and U. Schollwöck, Europhys. Lett. **66**, 178 (2004).

[75] I. Affleck, W. Hofstetter, D. R. Nelson, and U. Schollwöck, J. Stat. Mech.: Theor. Exp. **2004**, P10003 (2004).

[76] J. S. Langer and Q. Amberaogar, Phys. Rev. **64**, 498 (1967).

[77] P. Fulde and R. A. Ferrell, Phys. Rev. **135**, A550 (1964).

[78] A. A. Abrikosov, Soviet Phys. JETP **5**, 1174 (1957).

[79] Strictly speaking, the coupling constant g should be renormalized as $-1/g = m/4\pi\hbar^2 a_s - 1/V \sum_{\mathbf{k}} 1/2\epsilon_{\mathbf{k}}$, where V is the system volume and $\epsilon_{\mathbf{k}}$ is the excitation energy. However, as long as a_s is small compared to the transverse confinement, this regularization does not change the effective 1D model [23].

[80] J. N. Fuchs, A. Recati, and W. Zwerger, Phys. Rev. Lett. **93**, 090408 (2004).

[81] P. Rosenbusch, D. S. Petrov, S. Sinha, F. Chevy, V. Bretin, Y. Castin, G. Shlyapnikov, and J. Dalibard, Phys. Rev. Lett. **88**, 250403 (2002).

[82] A. Bulgac and Y. Yu, Phys. Rev. Lett. **91**, 190404 (2003).

[83] N. Nygaard, G. M. Bruun, C. W. Clark, and D. L. Feder, Phys. Rev. Lett. **90**, 210402 (2003).

[84] M. Machida and T. Koyama, Phys. Rev. Lett. **94**, 140401 (2005).

[85] R. Sensarma, M. Randeria, and T.-L. Ho, Phys. Rev. Lett. **96**, 090403 (2006).

[86] M. Takahashi, T. Mizushima, M. Ichioka, and K. Machida, Phys. Rev. Lett. **97**, 180407 (2006).

[87] Hui Hu, Xia-Ji Liu, and Peter D. Drummond, Phys. Rev. Lett. **98**, 060406 (2007).

[88] N. Nygaard, G. M. Bruun, B. I. Schneider, C. W. Clark, and D. L. Feder, Phys. Rev. A **69**, 053622 (2004).

[89] M. Machida, Y. Ohashi, and T. Koyama, Phys. Rev. A **74**, 023621 (2006).

[90] H. J. Warringa and A. Sedrakian, Phys. Rev. A **84**, 023609 (2011).

[91] D. L. Feder, Phys. Rev. Lett. **93**, 200406 (2004).

[92] G. Tonini, F. Werner, and Y. Castin, Eur. Phys. J. D **39**, 283 (2006).

[93] A. Bulgac, Y.-L. Luo, P. Magierski, K. J. Roche, and Y. Yu, Science **332**, 1288 (2011).

[94] H. Akera, A. H. MacDonald, S. M. Girvin, and M. R. Norman, Phys. Rev. Lett. **67**, 2375 (1991).

[95] G. Möller and N. R. Cooper, Phys. Rev. Lett. **99**, 190409 (2007).

[96] H. Zhai, R. O. Umucalılar, and M. Ö. Oktel, Phys. Rev. Lett. **104**, 145301 (2010).

[97] V. Schweikhard, I. Coddington, P. Engels, V. P. Mogendorff, and E. A. Cornell, Phys. Rev. Lett. **92**, 040404 (2004).

[98] V. Bretin, S. Stock, Y. Seurin, and J. Dalibard, Phys. Rev. Lett. **92**, 050403 (2004).

[99] E. E. Salpeter, Phys. Rev. **84**, 1226 (1951).

[100] We define the number of fermions and paired fermions as $N = \frac{\sqrt{2}L}{2\pi\tilde{\ell}} \int_{-K_0/2}^{K_0/2} \sum_n \langle a^\dagger_{K-nK_0\uparrow} a_{K-nK_0\uparrow} \rangle dK$ and $N_{\text{pair}} = \frac{\sqrt{2}L}{4\pi\tilde{\ell}} \int_{-K_0/2}^{K_0/2} \sum_{n,n'} |\langle a_{-K+nK_0\downarrow} a_{K-n'K_0\uparrow} \rangle|^2 dK$.

[101] D. Sciamarella and Y. Pomeau, Journal of Low Temp. Phys. **123**, 35, (2001)

[102] K. M. Jones, E. Tiesinga, P. D. Lett, and P. S. Julienne, Rev. Mod. Phys. **78**, 483 (2006).

[103] G. B. Partridge, K. E. Strecker, R. I. Kamar, M. W. Jack, and R. G. Hulet, Phys. Rev. Lett. **95**, 020404 (2005).

[104] H. E. Hall and W. F. Vinen, Proc. R. Soc. Lond. A **238**, 215 (1956).

[105] S. Teitel and C. Jayaprakash, Phys. Rev. B **27**, 598(R) (1983).

[106] N. R. Cooper, N. K. Wilkin, and J. M. F. Gunn, Phys. Rev. Lett. **87**, 120405 (2001).

[107] G. Möller and N. R. Cooper, Phys. Rev. Lett. **103**, 105303 (2009).

[108] L. Hormozi, G. Möller, and S. H. Simon, Phys. Rev. Lett. **108**, 256809 (2012).

[109] N. R. Cooper and J. Dalibard, Phys. Rev. Lett. **110**, 185301 (2013).

[110] N. R. Cooper, Advances in Physics **57**, 539 (2008).

[111] R. M. Noack, S. R. White, and D. J. Scalapino, Physica C **270** 281 (1996).

[112] H. J. Schulz, Phys. Rev. B **53**, 2959(R) (1996).

[113] G. Cristofanoa, V. Marottaa, A. Naddeob, and G. Niccoli, Phys. Lett. A **372**, 2464 (2008).

[114] M.-C. Cha and J.-G. Shin, Phys. Rev. A **83**, 055602 (2011).

[115] A. Petrescu and K. LeHur, Phys. Rev. Lett. **111**, 150601 (2013).

[116] A. Dhar, M. Maji, T. Mishra, R. V. Pai, S. Mukerjee, and A. Paramekanti, Phys. Rev. A **85**, 041602(R) (2012).

[117] A. Dhar, T. Mishra, M. Maji, R. V. Pai, S. Mukerjee, and A. Paramekanti, Phys. Rev. B **87**, 174501 (2013).

[118] A. Tokuno and A. Georges, New J. Phys. **16**, 073005 (2014).

[119] E. Orignac and T. Giamarchi, Phys. Rev. B **64**, 144515 (2001).

[120] L.-C. Ha, C.-L. Hung, X. Zhang, U. Eismann, S.-K. Tung, and C. Chin, Phys. Rev. Lett. **110**, 145302 (2013).

[121] E. Majorana, Nuovo Cimento **14**, 171 (1937).

[122] F. Wilczek, Nat. Phys. **5**, 614 (2009).

[123] C. Nayak, S. H. Simon, A Stern, M. Freedman, and S. DasSarma, Rev. Mod. Phys. **80**, 1083 (2008).

[124] N. Read and D. Green, Phys. Rev. B **61**, 10267 (2000).

[125] S. DasSarma, C. Nayak, and S. Tewari, Phys. Rev. B **73**, 220502(R) (2006).

[126] J. Alicea, Phys. Rev. B **81**, 125318 (2010).

[127] L. Fidkowski, R. M. Lutchyn, C. Nayak, and M. P. A. Fisher, Phys. Rev. B **84**, 195436 (2011).

[128] T. Mizushima, M. Ichioka, and K. Machida, Phys. Rev. Lett. **101**, 150409 (2008).

[129] J. D. Sau, R. M. Lutchyn, S. Tewari, and S. DasSarma, Phys. Rev. Lett. **104**, 040502 (2010).

[130] R. M. Lutchyn, J. D. Sau, and S. D. Sarma, Phys. Rev. Lett. **105**, 077001 (2010).

[131] L. Fu and C. L. Kane, Phys. Rev. Lett. **100**, 096407 (2008).

[132] Y. Oreg, G. Refael, and F. vonOppen, Phys. Rev. Lett. **105**, 177002 (2010).

[133] J. Alicea, Y. Oreg, G. Refael, F. vonOppen, and M. P. A. Fisher, Nat. Phys. **7**, 412 (2011).

[134] V. Mourik, K. Zuo, S. M. Frolov, S. R. Plissard, E. P. A. M. Bakkers, and L. P. Kouwenhoven, Science **336**, 1003 (2012).

[135] J. R. Williams, A. J. Bestwick, P. Gallagher, S. S. Hong, Y. Cui, A. S. Bleich, J. G. Analytis, I. R. Fisher, and D. G.-Gordon, Phys. Rev. Lett. **109** 056803 (2012).

[136] M. T. Deng, C. L. Yu, G. Y. Huang, M. Larsson, P. Caroff, and H. Q. Xu, Nano Lett. **12**, 6414-6419 (2012).

[137] A. Das. Y. Ronen, Y. Most, Y. Oreg, M. Heiblum, and H. Shtrikman, Nat. Phys. **8**, 887 (2012).

[138] P. Wang, Z.-Q. Yu, Z. Fu, J. Miao, L. Huang, S. Chai, H. Zhai, and J. Zhang, Phys. Rev. Lett. **109**, 095301 (2012).

[139] L. W. Cheuk, A. T. Sommer, Z. Hadzibabic, T. Yefsah, W. S. Bakr, and M. W. Zwierlein, Phys. Rev. Lett. **109**, 095302 (2012).

[140] C. Zhang, S. Tewari, R. M. Lutchyn, and S. DasSarma, Phys. Rev. Lett. **101**, 160401 (2008).

[141] M. Sato, Y. Takahashi, and S. Fujimoto, Phys. Rev. Lett. **103**, 020401 (2009).

[142] S.-L. Zhu, L.-B. Shao, Z. D. Wang, and L.-M. Duan, Phys. Rev. Lett. **106**, 100404 (2011).

[143] M. Gong, G. Chen, S. Jia, and C. Zhang, Phys. Rev. Lett. **109**, 105302 (2012).

[144] L. Jiang, T. Kitagawa, J. Alicea, A. R. Akhmerov, D. Pekker, G. Refael, J. I. Cirac, E. Demler, M. D. Lukin, and P. Zoller, Phys. Rev. Lett. **106**, 220402 (2011).

[145] X.-J. Liu and H. Hu, Phys. Rev. A **85**, 033622 (2012).

[146] X.-J. Liu, L. Jiang, H. Pu, and H. Hu, Phys. Rev. A **85**, 021603(R) (2012).

[147] L. Fidkowski, R. M. Lutchyn, C. Nayak, and M. P. A. Fisher, Phys. Rev. B **84**, 195436 (2011).

[148] Jay D. Sau, B. I. Halperin, K. Flensberg, and S. DasSarma, Phys. Rev. B **84**, 144509 (2011).

[149] M. Cheng and H.-H. Tu, Phys. Rev. B **84**, 094503 (2011).

[150] Y. Liao, A. S. C. Rittner, T. Paprotta, W. Li, G. B. Partridge, R. G. Hulet, S. K. Baur, and E. J. Mueller, Nature (London) **467**, 567 (2010).

[151] D.S. Petrov, D.M. Gangardt, and G.V. Shlyapnikov, J. Phys. IV France **116**, 3 (2004).

[152] Y. Shin, C. H. Schunck, A. Schirotzek, and W. Ketterle, Phys. Rev. Lett. **99**, 090403 (2007).

[153] C. H. Schunck, M. W. Zwierlein, C. A. Stan, S. M. F. Raupach, W. Ketterle, A. Simoni, E. Tiesinga, C. J. Williams, and P. S. Julienne, Phys. Rev. A **71**, 045601 (2005).

[154] C. A. Regal, M. Greiner, and D. S. Jin, Phys. Rev. Lett. **92**, 040403 (2004).

[155] J.-Y. Zhang, S.-C. Ji, Z. Chen, L. Zhang, Z.-D. Du, B. Yan, G.-S. Pan, B. Zhao, Y.-J. Deng, H. Zhai, S. Chen, and J.-W. Pan, Phys. Rev. Lett. **109**, 115301 (2012).

[156] T.-L. Dao, A. Georges, J. Dalibard, C. Salomon, and I. Carusotto, Phys. Rev. Lett. **98**, 240402 (2007).

[157] Z. Fu, P. Wang, L. Huang, Z. Meng, and J. Zhang, Phys. Rev. A **86**, 033607 (2012).

[158] C. Zhang, S. Tewari, R. M. Lutchyn, and S. DasSarma, Phys. Rev. Lett. **101**, 160401 (2008).

[159] M. Sato, Y. Takahashi, and S. Fujimoto, Phys. Rev. Lett. **103**, 020401 (2009).

[160] S.-L. Zhu, L.-B. Shao, Z. D. Wang, and L.-M. Duan, Phys. Rev. Lett. **106**, 100404 (2011).

[161] N. R. Cooper, Phys. Rev. Lett. **106**, 175301 (2011).

[162] M. Gong, G. Chen, S. Jia, and C. Zhang, Phys. Rev. Lett. **109**, 105302 (2012).

[163] X.-J. Liu and H. Hu, Phys. Rev. A **85**, 033622 (2012).

[164] X.-J. Liu, L. Jiang, H. Pu, and H. Hu, Phys. Rev. A **85**, 021603(R) (2012).

[165] X.-J. Liu and P. D. Drummond, Phys. Rev. A **86**, 035602 (2012).

[166] R. Wei and E. J. Mueller, Phys. Rev. A **86**, 063604 (2012).

[167] The data for ^{6}Li($2p$) was extracted from M. E. Gehm's PhD thesis: Preparation of an optically trapped degenerate Fermi gas of ^{6}Li: finding the route to degeneracy (Duke, 2003). The data of ^{40}K was extracted from T. Tiecke's PhD thesis: Feshbach resonances in ultracold mixtures of the fermionic gases ^{6}Li and ^{40}K (Amsterdam, 2010). The data of ^{23}Na, ^{85}Rb, ^{87}Rb, ^{133}Cs was extracted from D. A. Steck's online public resources (http://steck.us/alkalidata). The data of ^{6}Li($3p$) was from the private communications with R. G. Hulet (2012).

[168] P. M. Duarte, R. A. Hart, J. M. Hitchcock, T. A. Corcovilos, T.-L. Yang, A. Reed, and R. G. Hulet, Phys. Rev. A **84**, 061406(R) (2011).

[169] E. Arimondo, M. Inguscio, and P. Violino, Rev. Mod. Phys. **49**, 31 (1977).

[170] D. M. Brink and G. R. Satchler, Angular Momentum (Oxford, 1968).

[171] D. J. Thouless, Phys. Rev. B **27**, 6083 (1983).

[172] Q. Niu, Phys. Rev. B **34**, 5093 (1986).

[173] S. Aubry and G. André, Ann. Isr. Phys. Soc. **3**, 133 (1980).

[174] L.-J. Lang, X. Cai, and S. Chen, Phys. Rev. Lett. **108**, 220401 (2012).

[175] Z. Xu, L. Li, and S. Chen, Phys. Rev. Lett. **110**, 215301 (2013).

[176] Z. Xu and S. Chen, Phys. Rev. B **88**, 045110 (2013).

[177] L.-J. Lang and S. Chen, J. Phys. B: At. Mol. Opt. Phys. **47** 065302 (2014).

[178] Y. E. Kraus, Y. Lahini, Z. Ringel, M. Verbin, and O. Zilberberg, Phys. Rev. Lett. **109**, 106402 (2012).

[179] Y. E. Kraus and O. Zilberberg, Phys. Rev. Lett. **109**, 116404 (2012).

[180] Y. E. Kraus, Z. Ringel, and O. Zilberberg, Phys. Rev. Lett. **111**, 226401 (2013).

[181] F. Grusdt, M. Höning, and M. Fleischhauer, Phys. Rev. Lett. **110**, 260405 (2013).

[182] S. Ganeshan, K. Sun, and S. D. Sarma, Phys. Rev. Lett. **110**, 180403 (2013).

[183] S.-L. Zhu, Z.-D. Wang, Y.-H. Chan, and L.-M. Duan, Phys. Rev. Lett. **110**, 075303 (2013).

[184] K. A. Madsen, E. J. Bergholtz, and P. W. Brouwer, Phys. Rev. B **88**, 125118 (2013).

[185] I. I. Satija and G. G. Naumis, Phys. Rev. B **88**, 054204 (2013).

[186] X. Deng and L. Santos, Phys. Rev. A **89**, 033632 (2014).

[187] F. Matsuda, M. Tezuka, and N. Kawakami, J. Phys. Soc. Jpn. **83**, 083707 (2014).

[188] D.-T. Tran, A. Dauphin, N. Goldman, and P. Gaspard, Phys. Rev. B **91**, 085125 (2015).

[189] F. Mei, S.-L. Zhu, Z.-M. Zhang, C. H. Oh, and N. Goldman, Phys. Rev. A **85**, 013638 (2012).

[190] P. Marra, R. Citro, and C. Ortix, Phys. Rev. B **91**, 125411 (2015).

[191] F. Liu, S. Ghosh, and Y. D. Chong, Phys. Rev. B **91** 014108 (2015).

[192] J.-T. A. Chiang and Q. Niu, Phys. Rev. A **57**, R2278 (1998).

[193] O. R.-Isart and J. J. G.-Ripoll, Phys. Rev. A **76**, 052304 (2007).

[194] Y. Qian, M. Gong, and C. Zhang, Phys. Rev. A **84**, 013608 (2011).

[195] L. Wang, M. Troyer, and X. Dai, Phys. Rev. Lett. **111**, 026802 (2013).

[196] F. Mei, J.-B. You, D.-W. Zhang, X. C. Yang, R. Fazio, S.-L. Zhu, and L. C. Kwek, Phys. Rev. A **90**, 063638 (2014).

[197] D.-W. Zhang, F. Mei, Z.-Y. Xue, S.-L. Zhu, and Z. D. Wang, Phys. Rev. A **92**, 013612 (2015).

[198] M. Kohmoto, Ann. Phys. (Berlin) **160**, 343 (1985).

[199] M. Atala, M. Aidelsburger, M. Lohse, J. T. Barreiro, B. Paredes, and I. Bloch, Nat. Phys. **10**, 588 (2014).

[200] M. Aidelsburger, M. Lohse, C. Schweizer, M. Atala, J. T. Barreiro, S. Nascimbène, N. R. Cooper, I. Bloch, and N. Goldman, Nat. Phys. **11**, 162 (2015).

[201] A. Dauphin and N. Goldman, Phys. Rev. Lett. **111**, 135302 (2013).

[202] H. M. Price and N. R. Cooper, Phys. Rev. A **85**, 033620 (2012).

[203] X.-J. Liu, K. T. Law, T. K. Ng, and P. A. Lee, Phys. Rev. Lett. **111**, 120402 (2013).

[204] D. A. Abanin, T. Kitagawa, I. Bloch, and E. Demler, Phys. Rev. Lett. **110**, 165304 (2013).

[205] M. Atala, M. Aidelsburger, J. T. Barreiro, D. Abanin, T. Kitagawa, E. Demler, and I. Bloch, Nat. Phys. **9**, 795 (2013).

[206] F. Grusdt, D. Abanin, and E. Demler, Phys. Rev. A **89**, 043621 (2014).

[207] E. Alba, X. F.-Gonzalvo, J. M.-Petit, J. K. Pachos, and J. J. Garcia-Ripoll, Phys. Rev. Lett. **107**, 235301 (2011).

[208] E. Zhao, N. B.-Ali, C. J. Williams, I. B. Spielman, and I. I. Satija, Phys. Rev. A **84**, 063629 (2011).

[209] D.-L. Deng, S.-T. Wang, and L.-M. Duan, Phys. Rev. A **90**, 041601(R) (2014).

[210] N. Goldman, J. Dalibard, A. Dauphina, F. Gerbierb, M. Lewensteine, P. Zoller, and I. B. Spielman, Proc. Natl. Acad. Sci. U.S.A. **110**, 6736 (2013).

[211] N. Goldman, J. Beugnon, and F. Gerbier, Phys. Rev. Lett. **108**, 255303 (2012).

[212] N. Goldman, J. Beugnon, and F. Gerbier, Eur. Phys. J.: Spec. Top. **217**, 135 (2013).

[213] M. D. Reichl and E. J. Mueller, Phys. Rev. A **89**, 063628 (2014).

[214] B. K. Stuhl, H.-I. Lu, L. M. Aycock, D. Genkina, and I. B. Spielman, Science **349**, 1514 (2015).

[215] M. Mancini, G. Pagano, G. Cappellini, L. Livi, M. Rider, J. Catani, C. Sias, P. Zoller, M. Inguscio, M. Dalmonte, and L. Fallani, Science **349**, 1510 (2015).

[216] R. O. Umucalılar, H. Zhai, and M. Ö. Oktel, Phys. Rev. Lett. **100**, 070402 (2008).

[217] L. B. Shao, S.-L. Zhu, L. Sheng, D. Y. Xing, and Z. D. Wang, Phys. Rev. Lett. **101**, 246810 (2008).

[218] M. Kohmoto, J. Phys. Soc. Jpn. **61**, 2645 (1992).

[219] D. Osadchy and J. E. Avron, J. Math. Phys., **42**, 5665 (2001).

[220] N. Goldman, J. Phys. B: At. Mol. Opt. Phys. **42**, 055302 (2009).

[221] J. E. Avron, O. Kenneth, and G. Yehoshua, J. Phys. A: Math. Theor. **47**, 185202 (2014).

[222] Q. Niu, Phys. Rev. Lett. **64**, 1812 (1990).

[223] N. Marzari, A. A. Mostofi, J. R. Yates, I. Souza, and D. Vanderbilt, Rev. Mod. Phys. **84**, 1419 (2012).

[224] T. Fukui, Y. Hatsugai, H. Suzuki, and M. Kohmoto, J. Phys. Soc. Jpn. **74**, 1674 (2005).

[225] W. S. Bakr, A. Peng, M. E. Tai, R. Ma, J. Simon, J. I. Gillen, S. Fölling, L. Pollet, and M. Greiner, Science **329**, 547 (2010).

[226] N. Gemelke, X. Zhang, C.-L. Hung, and C. Chin, Nature (London) **460**, 995 (2009).

[227] J. F. Sherson, C. Weitenberg, M. Endres, M. Cheneau, I. Bloch, and S. Kuhr, Nature (London) **467**, 68 (2010).

[228] I. Bloch, J. Dalibard, and W. Zwerger, Rev. Mod. Phys. **80**, 885 (2008).

[229] M. Greiner, O. Mandel, T. Esslinger, T. W. Hänsch, and I. Bloch, Nature (London) **415**, 39 (2002).